University of Genoa

Doctoral Thesis

# Vascular remodeling after endovascular treatment: quantitative analysis of medical images with a focus on aorta


*Supervisor:*
**Prof. Domenico Palombo**
*Co-supervisors:*
**Prof. Ferdinando Auricchio**
**Dr. Giovanni Spinella**
**Dr. Michele Conti**
**Dr. Elena Faggiano**

*Author:*
**Alice Finotello**


*A thesis submitted in fulfillment of the requirements for the degree of Doctor of Philosophy*
*in*

Biotechnologies in Translational Medicine


Academic year 2017/2018
XXXI PhD course

*"Graduation is only a concept. In real life every day you graduate.*
*Graduation is a process that goes on until the last day of your life.*
*If you can grasp that, you'll make a difference."*
*A.P.*

# Abstract

In the last years, the convergence of advanced imaging techniques and endovascular procedures has revolutionized the practice of vascular surgery. However, regardless the anatomical district, several complications still occur after endovascular treatment and the impact of endovascular repair on vessel morphology remains unclear. Starting from this background, the aim of this thesis is to fill the gaps in the field of vessel remodeling after endovascular procedure. Main focus of the work will be the repair of the aorta and, in particular thoracic and thoracoabdominal treatments. Furthermore an investigation of the impact of endovascular repair on femoro-popliteal arterial segment will be reported in the present work. Analyses of medical images will been conducted to extract anatomical geometric features and to compare the changes in morphology before treatment and during follow-up.

After illustrating in detail the aims and the outline of the dissertation in Chapter 1, Chapter 2 will concern the anatomy and the physiology of the aorta along with the main aortic pathologies and the related surgical treatments. Subsequently, an overview of the medical image techniques for segmentation and vessel geometric quantification will be provided.

Chapter 3 will introduce the concept of remodeling of the aorta after endovascular procedure. In particular, two types of aortic remodeling will be considered. On one side remodeling can be seen as the shrinkage of the aneurysmal sac or false lumen thrombosis. On the other side, aortic remodeling could be seen as the changes in the aortic morphology following endograft placement which could lead to complications.

Chapter 4 will illustrate a study regarding the analysis of medical images to measure the geometrical changes in the pathological aorta during follow-up in patients with thoracoabdominal aortic aneurysms treated with endovascular procedure using a novel uncovered device, the Cardiatis Multilayer Flow Modulator.

Chapter 5 will focus on the geometrical remodeling of the aortic arch and descending aorta in patients who underwent hybrid arch treatment to treat thoracic aneurysms. The goal of the work is to develop a pipeline for the processing of pre-operative and post-operative Computed Tomography images in order to detect the changes in the aortic arch physiological curvature due to endograft insertion.

Chapter 6 will focuse on the use of 3D printing technology as valuable tool to support patient's follow-up. In particular, we report a case of a patient originally treated with endovascular procedure for type B aortic dissection and which experimented several complications during follow-up. 3D printing technology is used to show the remodeling of the aortic vasculature

during time.
Chapter 7 will concern patient-specific finite element simulations of aortic endovascular procedure. In particular, starting from a clinical case where complication developed during follow-up, the predictive value of computational simulations will be shown.
Chapter 8 will illustrate a study concerning the evaluation of morphological changes of the femoro-popliteal arterial segment due to limb flexion in patients undergoing endovascular treatment of popliteal artery aneurysms.

# Acknowledgments

It seems like yesterday I started and three years have already passed...
First of all, I would like to express my gratitude to my supervisor Professor Domenico Palombo: thanks for your knowledge and for introducing me in the vascular surgery world.
My highest gratitudes go to Giovanni Spinella, who supported me every day with motivation and enthusiasm.
I am also thankful to all vascular "colleagues": Bianca, Valerio, Cecilia, Maria Antonietta, Sara, Rachele, Giorgio, Gian Antonio, Tareq, Elvira and Mauro. Thanks for your nice company!
A special thanks to all CompMech group. Thanks to the group head Prof. Ferdinando Auricchio who kindly invite me to his Lab in Pavia (my second home during the last four years!). I am really thankful to Michele Conti and Simone Morganti for their interest in my work and for the help they give me.
A very big (!) thanks to Elena Faggiano: image processing wasn't the same without you!
Many thanks to all my CompMech colleagues. First of all, a huge big GRAZIE to Alberto and Margherita who shared with me the PhD and the related anxieties (especially Margherita). I couldn't have done it without you and your advices.
Thanks to my new office mates Alex, Ahmed, Gaetano and Massimo. Gianmaria, Mauro, Lorenzo, Alfredo, Giulia, Anna, Sonia, Francesca, Prof Alessandro Reali, Stefania, Gianluca, Valeria, Erika, Franca, Giulia, Laura, Jessica, Alberto S., Karim, Osama, Guillermo, Giorgione, Valentina, Rodrigo, Marco, Andrea and Xi: thanks for your always good company during these years. Many thanks also to all the new arrivals of the Group!
None of this would have been possible without the support of my family. Grazie Mamma e Papà!
Finally, I would like to thank Cristiano, my "new family".

# Contents

# List of Tables

# List of Figures

# List of Abbreviations

$D_{AR-LSA}$ Distance from aortic root to left subclavian artery

$D_{LSA-D}$ Distance from left subclavian artery to distal landing zone

$v_{LR}$ Volume of lumen region

$v_{RF}$ Volume of residual flow

$v_{TAR}$ Volume of total aneurysm

AAA Abdominal aortic aneurysms

AR Aortic root

AsAo Ascending aorta

CFD Computational Fluids Dynamics

CI Confidence Interval

CL Length of the centerline covered by the endograft(s)

CT Computed Tomography

CTA Computed Tomography Angiography

D1 Distal landing point

DICOM Digital Imaging and Communication in Medicine

DsAo Descending aorta

ER Endografting region

EVAR EndoVascular Aneurysm Repair

FEA Finite Element Analysis

FL Flexed leg

FPA Femoral-popliteal artery

HU Hounsfield Units

ICC Intraclass Correlation Coefficient

ICP Iterative Closest Point algorithm

IFU Instructions for use

ILT Intraluminal thrombus

IMH Intramural Hematoma

L Centerline length

LR Lumen region

LSA Left subclavian artery

MFM Multilayer Flow Modulator

MFMF Multilayer flow modulator blood flow

MRI Magnetic Risonance Imaging

P1 Proximal landing point

PAA Popliteal artery aneurysms

PAD Peripheral artery disease

PAU Penetrating Atherosclerotic Ulcer

RF Residual blood flow

rTAAD Retrograde type-A aortic dissection

RTR ratio of thrombotic region

SCI Spinal cord ischemia

SI Shape Index

SL Straight leg

TA Total aorta

TAAA Thoraco-abdominal aortic aneurysms

TAR Total aneurysm region

TEVAR Thoracic EndoVascular Aneurysm Repair

# Chapter 1

# Outline of the thesis work

This thesis presents the work done during the Ph.D. course and constitutes the compendium of the main results.
The main objective of this work is to fill the gaps in the field of vessel remodeling after endovascular treatments. Main focus is on the endovascular repair of the aorta to investigate the impact of such treatment on vessel morphology. In particular, the work is based the integration of medical imaging techniques and computational facilities to extract anatomical geometric features and to quantify the changes in morphology before and after treatment and during follow-up time with the final aim of providing outcomes with high impact in the clinical research. Moreover, the concept of geometric analysis to investigate the impact of endovascular treatment has been applied also to the femoro-popliteal arterial segment which is usually considered an hostile environment for endovascular stenting due to repetitive daily leg flexion. Most of such investigations resulted in specific publications which are listed at the end of the present chapter.
This research work has been conducted at the Vascular and Endovascular Surgery Unit of Ospedale Policlinico San Martino, Genoa and in very close collaboration with the Computational Mechanics and Advanced Material Group of the Department of Civil Engineering and Architecture, University of Pavia.

In this study we integrated techniques of medical imaging and computational facilities to obtain a better understanding of the vascular pathologies and to provide outcomes with high impact in the clinical research.

## 1.1 Organization of the dissertation

After this introductory chapter, the present dissertation is structured as follows:

- Chapter 2 will be devoted to the understanding of the aorta and of the most common pathologies associated with aging and atherosclerotic processes (i.e. aortic aneurysms

and dissections). Current surgical options will be investigated with a special focus to endovascular procedures. Then, an overview of medical image processing and geometric features extraction exploited in the work will be presented.

- Chapter 3 will introduce the concept of remodeling of the aorta after endovascular procedure. In particular, two types of aortic remodeling will be considered. On one side remodeling can be seen as the shrinkage of the aneurysmal sac or false lumen thrombosis. On the other side, aortic remodeling could be seen as the changes in the aortic morphology following endograft placement which could lead to complications.
- Chapter 4 will illustrate a study regarding the analysis of medical images to measure the geometrical changes during follow-up after endovascular treatment using a novel device, the Cardiatis Multilayer Flow Modulator.
- Chapter 5 will focus on the geometrical remodeling of the aortic arch and descending aorta in patients who underwent hybrid arch treatment to treat thoracic aneurysms. The goal of the work is to develop a pipeline for the processing of pre-operative and post-operative Computed Tomography Angiography images in order to detect the changes in the aortic arch physiological curvature due to endograft insertion.
- Chapter 6 will regard a case report regarding a patient originally treated with endovascular procedure for type B aortic dissection and which experimented several complications during follow-up. 3D printing technology is used to show the remodeling of the aortic vasculature during time.
- Chapter 7 will concern patient-specific structural simulations of aortic endovascular procedure. In particular, starting from a clinical case where complication developed during follow-up, the predictive value of computational simulations will be showed.
- Chapter 8 will illustrate a study concerning the evaluation of femoro-popliteal artery changes during knee flexion in patients who underwent endovascular treatment of popliteal artery aneurysms by means a standardized protocol for computed tomography angiography acquisition with both straight leg and flexed hip/knee position and *in-vivo* medical image analysis.
- In the last Chapter, the conclusions are drawn highlighting the original aspects of the doctoral research. Moreover, further research developments are outlined.

### 1.1.1 List of pubblications

- Chapter 3 resulted in the paper:
  Palombo D, Spinella G, Gazzola V, **Finotello A**, Mambrini S, Conti M, Auricchio F, Pane B. "Thoracic aorta remodeling after endovascular treatment" in Aortic Complexities, Edi.Ermes

- Chapter 4 resulted in the papers:
  - Spinella G, **Finotello A**, Faggiano E, Pane B, Conti M, Gazzola V, Auricchio F, Palombo D. Mid-term follow-up geometrical analysis of thoraco-abdominal aortic aneurysm treated with multilayer flow modulator. Annals of Vascular Surgery 2018; 53: 97-104.
  - Faggiano E, Spinella G, Fedele M, **Finotello A**, Conti M, Pane B, Perfumo MC, Auricchio F, Palombo D. "The theoretical and experimental basis of the Multilayer Flow Modulator" in Palombo D., Pane B. , Spinella G. Editor. The current role of Multilayer Flow Modulator Stents in Complex Aortic Pathology. Torino: Edizioni Minerva Medica; 2017, ISBN: 978-88-7711-891-2;
  - **Finotello A**, Faggiano E, Conti M, Spinella G, Pane B, Palombo D, Auricchio F. Medical image analysis to measure the follow-up geometry of thoraco-abdominal aortic aneurysms treated with multilayer ow modulator stent. CMBBE: I & V. Revision submitted.
- Chapter 5 resulted in the paper:
  Spinella G, **Finotello A**, Conti M, Faggiano E, Gazzola V, Auricchio F, Chakfé N, Palombo D, Pane B. Assessment of geometrical remodeling of the aortic arch after hybrid treatment. European Journal of Cardio-Thoracic Surgery. In press.
- Chapter 6 resulted in the paper:
  **Finotello A**, Marconi S, Pane B, Conti M, Gazzola V, Mambrini S, Auricchio F, Palombo D, Spinella G. Twelve-year Follow-up Post-Thoracic Endovascular Repair in Type B Aortic Dissection Shown by Three-dimensional Printing. Annals of Vascular Surgery 2019; 55: 309-e13.
- Chapter 7 resulted in the proceeding:
  **Finotello A**, Spinella G, Conti M, Pane B, Auricchio F, Palombo D. Toward the use of patient-specific structural simulations of endovascular repair in the clinical practice. $67^{th}$ International congress of the European Society of Cardiovascular and Endovascular Surgery (Strasbourg, France). Abstract published online. YOUNG SURGEON AWARD 1st PLACE.
- Chapter 8 resulted in the paper:
  Spinella G, **Finotello A**, Pane B, Salsano G, Mambrini S, Kamenskiy A, Gazzola V, Cittadini G, Auricchio F, Palombo D, and Conti M. *In-vivo* morphological changes of the femoropopliteal artery due to limb flexion after endovascular treatment of popliteal aneurysms. Journal of Endovascular Therapy; accepted for publication.

# Chapter 2

# Introduction

The vascular system is an organ system constituted from vessels that carry blood and lymph (lymphatic system) through the body. The circulatory system of the blood has two components: a systemic (arterial) circulation and a pulmonary circulation (see Figure 2.1): the arteries carry blood away from the heart to the tissues under high pressure; the veins transport it back to the heart.

## 2.1 Aorta

The aorta is the main artery of the human body, it is about 30-40 cm long and has an average diameter of 2.5-3.5 cm. The aorta is located before the thorax, in the posterior mediastinal portion, crosses the diaphragm muscle passing in the special orifice and finally goes to place on the back wall of the abdominal cavity. It originates directly from the heart, precisely from the base of the left ventricle, from which it is functionally separated from the aortic semilunar valve, which pushes inside the oxygen-rich blood from the left atrium (where the pulmonary veins emerge). After originating from the left ventricle with a diameter of about 3 cm, the aorta goes upwards originating the thoracic ascending aorta, and bends forming the aortic arch going to lean on the vertebral column. Three important arterial vessels originate from the aortic arch:

- Anonymous artery (or brachiocephalic arterial trunk) which divides into the right common carotid artery and right subclavian artery that goes respectively in the head and in the right arm.
- Left common carotid artery that suppies blood to the head.
- Left subclavian artery that carries blood in the left arm.

From the aortic arch the aorta descends forming the descending thoracic aorta and crosses the diaphragm to form the abdominal aorta. The abdominal aorta does not end up bifurcating

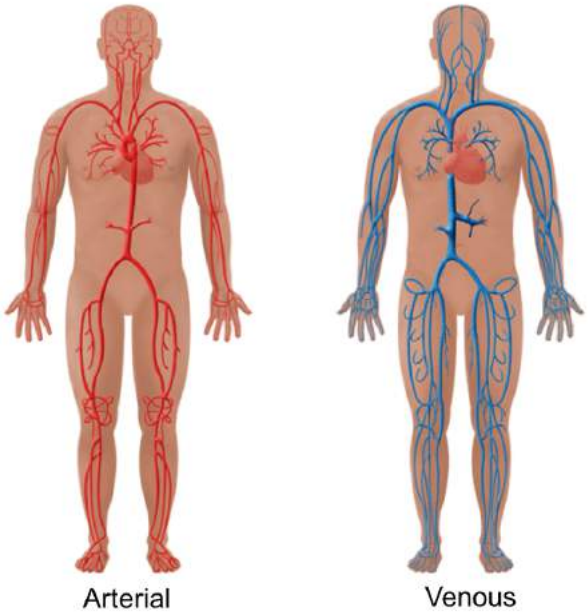


Figure 2.1: Arterial (left) and pulmonary (right) circulatory system. Reproduced from hopkinsmedicine.org.

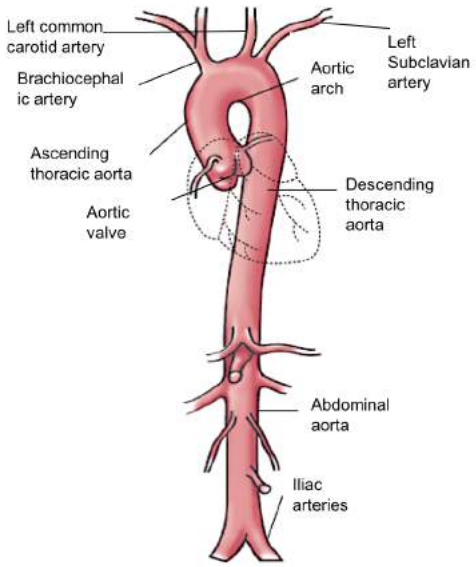


Figure 2.2: After originating from the aortic valve of the heart, the aorta divides into the ascending aorta, the aortic arch, the descending (thoracic) aorta, and the abdominal aorta. Reproduced from my.clevelandclinic.org.

into the right and left common iliac artery.
From the descending thoracic and abdominal portion arise both branches destined to the walls of the thorax and abdomen (intercostal, diaphragmatic, lumbar arteries) and branches destined to the viscera contained in these cavities (esophageal, bronchial, renal, adrenal, spermatic or ovarian arteries, mesenteric arteries, and celiac trunk) [Uflacker [2006a]; Uflacker [2006b]].
The task of the aorta is therefore to distribute the oxygen-rich blood to the lower-sized arteries; these, in turn, repeatedly branch off to vascularize the tissues of the entire organism. The aorta, however, is not a simple conduit of blood transport, but a real organ: thanks to the marked elasticity of its walls it is able to dilate during systole and relax during diastole, in order to ensure a constant flow of blood into the secondary arteries. The aortic endothelium also secretes numerous vasoactive peptides able to modulate the activity, not only of the various structures of the vessel wall, but also of the blood cells and proteins of the coagulation system that come into contact with it [Sandoo et al., 2010].

The part of the aorta that crosses the thorax is called thoracic aorta whereas the part that passes through the abdomen is called abdominal aorta. The thoracic aorta is further divided into ascending aorta, aortic arch, and descending thoracic aorta.
The other arterial branches, the so-called collateral branches, originate from the aorta. In particular from the aortic arch the vessels that spray the head, the neck, the upper limbs and the upper part of the thorax are unraveled; on the contrary, the branches that supply

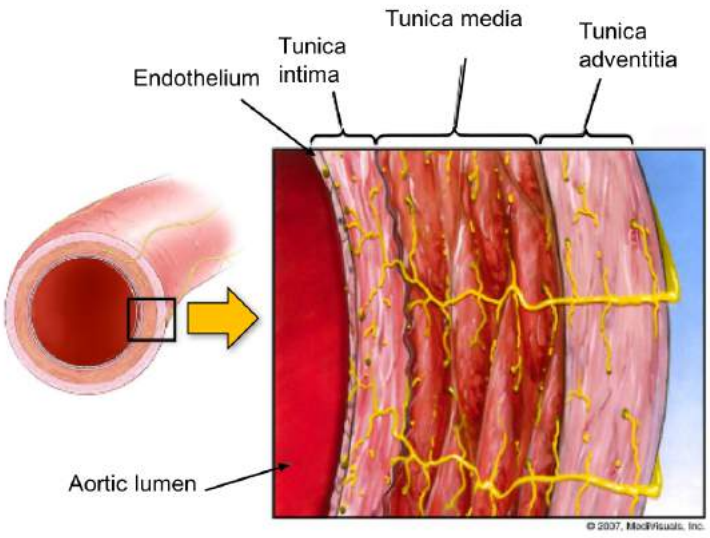


Figure 2.3: Structural organization of the aorta. Reproduced from www.medvisuals.com

the organs like lungs, kidneys, stomach and intestines originate from the descending aortic segment.
As shown in Figure 2.3, the aortic wall consists of a three-layer structure:

- the innermost layer is called tunica intima and is in direct contact with the blood and is composed of endothelial cells;
- the middle layer is the tunica media, thicker and composed of smooth muscle tissue, with the function of cushioning changes in internal blood pressure;
- the tunica adventitia is the outer layer consisting of collagen and elastic fibers oriented along the axis of the vessel, giving the vessel resistance to mechanical stress [Cronenwett and Johnston, 2014].

## 2.2 Pathologies

### 2.2.1 Aortic aneurysm

The most common disease of the aorta is the aneurysm, a dilation of the aortic wall due to degenerative phenomena of the elastic component of the vessel wall and therefore to the weakening and collapse of the same (see Figure 2.4). In particular the aneurysm is formed from the degeneration of the fibers of the medium tunic, which spontaneous regenerative mechanisms tend to replace with anelastic fibrous tissue which, not being able to withstand

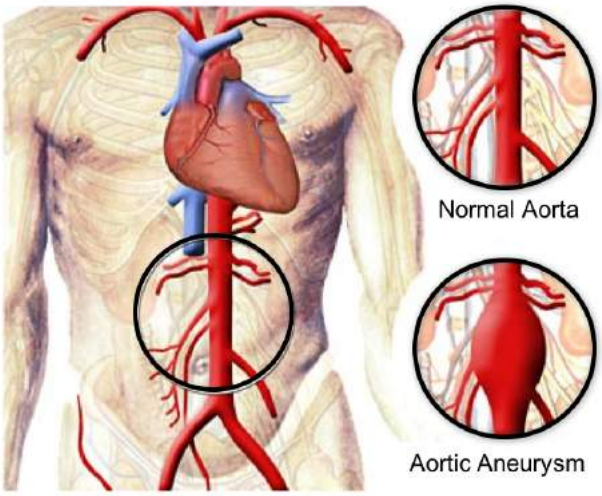


Figure 2.4: Illustration of a human body with close-ups of a normal aorta and one with aortic aneurysm. Adapted from edu.glogster.com

the pressure wave due to the flow of blood, tends to be worn out. Furthermore, the plaque builds up in this tissue, causing a zone called a thrombus. When the bulge grows to 50 percent or greater than the normal size it is classified as aneurysm O'gara [2003].
The initial mechanism that causes the weakening of the wall and triggers the dilatation is often atherosclerosis, mostly contextual to arterial hypertension. Another frequently involved process is cystic necrosis of the tunica media, in which the elastic fibers are progressively destroyed by the degenerative process and this, together with the arterial hypertension, causes the vessel to dilate.
The risk linked to this pathology is therefore that of the vessel breaking with consequent internal bleeding that, depending on the district concerned, can be fatal.
Aortic aneurysms are subdivided according to their location in thoracic aortic aneurysms and abdominal aortic aneurysms. Thoracic aortic aneurysms are then subdivided according to their position in the ascending aortic, aortic arch, or descending thoracic aortic aneurysms, whereas the abdominal ones are defined according to the relationship with the renal arteries in subrenal (the most frequent) and suprarenal abdominal aortic aneurysms. Thoracoabdominal aortic aneurysms traverse the diaphragm and involve portions of both the thoracic and the abdominal aorta.
Based on their extension, according to Crawford classification, these can be categorized as follows:

- Type 1: involves the proximal half of the descending aorta and extends up to the level of the renal arteries.

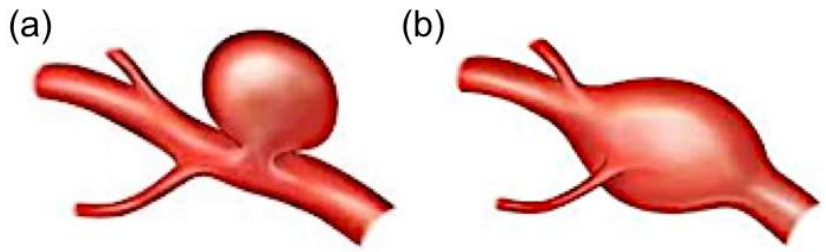


Figure 2.5: Diagrams of (a) saccular and (b) fusiform aneurysms.
Reproduced from www.ettaastudy.com

- Type 2: extends from the proximal half of the descending thoracic aorta to the sub-renal aorta.
- Type 3: extends from the distal half of the descending thoracic aorta to the abdominal aorta.
- Type 4: involves most of the abdominal aorta with origin above the renal arteries.

Morphologically we can distinguish between fusiform and saccular aneurysms. Saccular aneurysms (see Figure 2.5a) are balloon-like bulges that protrude from one side of the affected aorta segment. Typically these are pseudoaneurysms caused by trauma such as a traffic accident or are the result of a penetrating aortic ulcer. Fusiform aneurysms, on the other hand, are bulges that involve the affected aorta segment in its entirety (see Figure 2.5b) [Cronenwett and Johnston, 2014].
Most aortic aneurysms are completely silent (they do not give any sign of self until they get complicated, causing very serious problems such as rupture or dissection of the aneurysm itself), and the diagnosis is often casual during investigations that are performed for other diseases; for example, the abdominal aortic aneurysms are often incidentally diagnosed during a prostate ultrasound.

### 2.2.2 Aortic dissection

The aortic dissection is characterized by an intimal tear with separation of the tunica media from the tunica adventitia and the consequent formation of a second blood flow ("false lumen") from the original one ("true lumen"). More details are given in figure 2.6. This process leads to a weakening of the vascular wall and an alteration of the relations between the aorta and the arterial vessels afferent. Sometimes the intimal tear is the first act of this process, other times the first step consists of a hematoma in the tonaca media determined by an injury of the Vasa Vasorum and / or fibrillary sloughing. Dissection propagation can proceed both

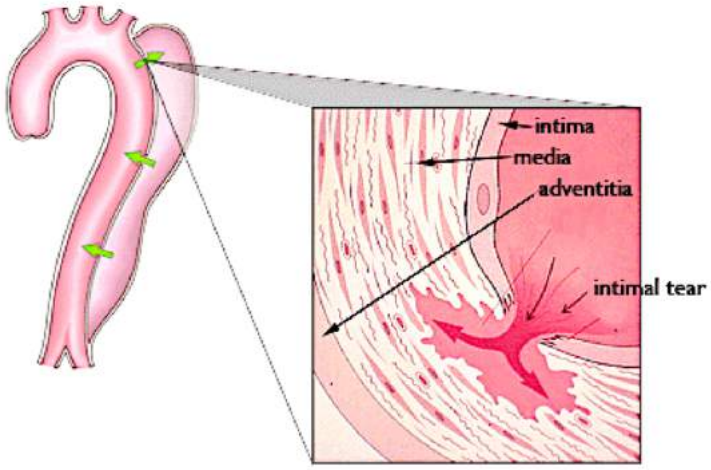


Figure 2.6: Schematic representation of aortic dissection: entry and re-entry tears are green highlighted. Pathogenesis of the aortic dissection. Reproduced from [Pyeritz and Gasner, 1999].

anterograde and retrograde from the initial point of the lesion involving the lateral branches and causing complications such as malperfusion syndrome, or aortic valvular insufficiency.
Based on the interval from the onset of symptoms a dissection can be classified as acute (<14 days) or chronic (> 14 days). Acute aortic dissection is a surgical emergency and is among the vascular diseases with higher mortality. Its early recognition can make the difference in patient survival with good outcomes.
The factors that lead to the breaking of the integrity of the intimal tear are both genetic and acquired. The most common risk factor for aortic dissection is hypertension which, due to a chronic exposure of the aorta to high pressures, leads to a thickening of the intima, fibrosis, calcification and extracellular deposit of fatty acids. Genetic conditions such as Marfan syndrome, Ehlers-Danlos vascular syndrome, annuloaortic ectasia, and bicuspid aortic valve can often cause acute syndromes of the aorta, including acute aortic dissection [Tintoiu et al., 2017].

Stanford's classification distinguishes between type A and type B aortic dissection. In the first case the dissection involves the ascending aorta, in the second case the only descending aorta. The classification of DeBakey distinguishes instead 3 types of dissection:

1. type I which involves the entire aorta;
2. type II which involves only the ascending aorta;
3. type III which excludes the ascending aorta and the aortic arch.

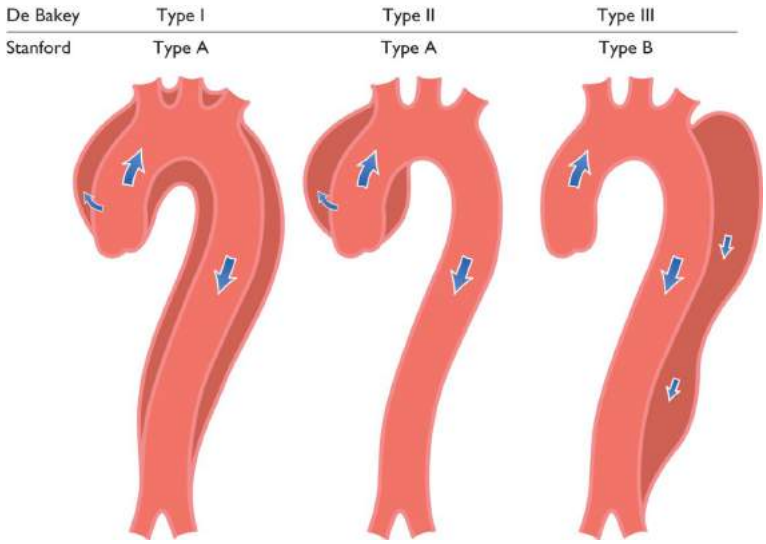


Figure 2.7: Most common classification systems of aortic dissections: De Bakey and Stanford. Reproduced from Imagerie médicale, hopital d'Antibes, France

Furthermore, dissections can be divided into complicated and uncomplicated. Complicated dissections exhibit one or more of the following characteristics: rupture, impending rupture, collateral branch involvement with malperfusion syndrome or persistent chest pain, drug-resistant hypertension, and false lumen aneurysms [Levy and Le, 2018].

## 2.3 Inclusion criteria and treatment

### 2.3.1 Aortic aneurysms

The aneurysm can be treated pharmacologically or surgically, depending on the stage of advancement, size and severity. In the case of initial or non-severe aneurysms with a diameter of less than 5 cm, drugs such as beta-blockers and calcium channel blockers are administered to lower blood pressure and thus reducing the risk of rupture. Furthermore, in these patients, close clinical surveillance is required, in particular to monitor that the blood pressure is maintained at the recommended levels (systolic blood pressure $\leq$110 mmHg). If instead the aneurysm has a very rapid growth or is in conditions of greater severity, it is necessary to intervene surgically. There are two possible techniques: the so-called open surgery or the endovascular treatment ((T)EVAR - (Thoracic) EndoVascular Aneurysm Repair).
In the first case, the affected aortic segment is removed and replaced with an artificial stroke in material such as Dacron (see Figure 2.8 left).
The endovascular technique is a less invasive technique which consists in the positioning of an endoprosthesis to cover the pathologic segment of the aorta (Figure 2.8 right). This method

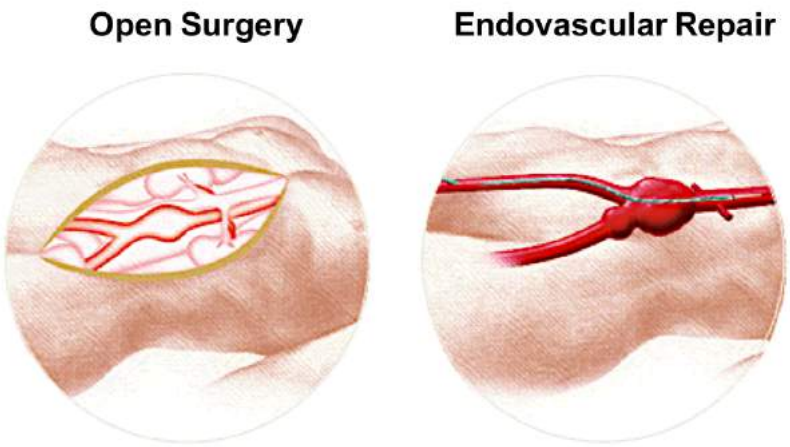


Figure 2.8: Treatment options: open repair (left) and endovascular aortic repair (right). Reproduced from ww.vascularinfo.co.uk.

is made even more convincing by the fact that classical surgical treatment often involves a high perioperative mortality, with serious complications, including paraplegia, renal failure and cerebral stroke.
Ascending aortic aneurysms are generally treated with surgical reconstruction, whereas descending aortic aneurysms are treated with both surgical technique and endovascular technique.

### 2.3.2 Aortic dissections

Depending on the type of dissection the therapy will be:

1. Surgical, in acute dissection of type A (while waiting for the intervention, it will still be necessary to control the arterial pressure to avoid the progress of the damage. Intervention could consist in surgical or endovascular treatment.

2. From the IRAD register it emerges that 78% of patients with type B dissection are treated with pharmacological therapy alone, 11% undergo endovascular treatment and 11% is submitted to open surgery [Fattori et al., 2008].

## 2.4 Endovascular treatment

The endovascular treatment of the aorta has focused the joint interest of different specialists, radiologists, vascular surgeons, cardiac surgeons, cardiologists, favoring a progressive inter-

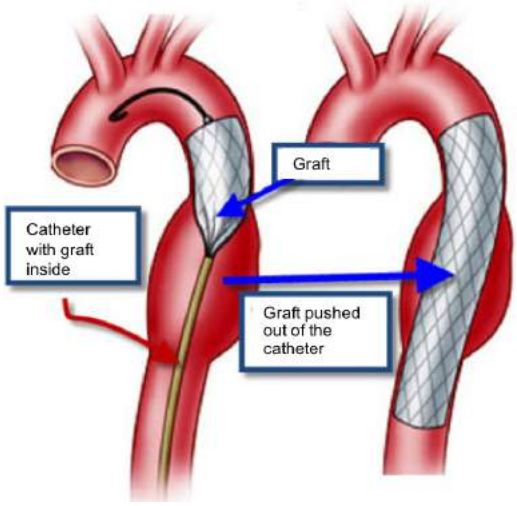


Figure 2.9: Endovascular procedure of aortic aneurysm.
Reproduced from bestheartsurgery.com

penetration of the different experiences [Oderich and Factor, 2017].
The insertion takes place by means of a catheter, typically accessing the femoral artery and, once the correct positioning has been verified through angiographic images, the stent is expanded and anchored to the wall of the aorta before and after the aneurysmal portion, remaining fixed in position (see Figure 2.9).The endoprosthesis thus creates a stable channel for blood flow, reducing pressure inside the aneurysm and preserving it from rupture. In cases of aortic dissection, the endoprosthesis is placed in correspondence of the entry tear, inducing false lumen thrombosis and true lumen expansion.
An accurate pre-operative planning to locate an adequate (in terms of diameters and lengths) proximal landing zone is mandatory in order to achieve stable fixation and sealing and to avoid re-interventions during follow-up. In the evaluation of an appropriate proximal landing zone, the application of traditional TEVAR requires a proximal zone of at least 20 mm of healthy and relatively straight neck, with diameter lower than 40 mm and without significant calcification or thrombus. At the present, there are numerous commercially available endoprostheses which vary depending from the stent material, graft fabric, and fixation. The most classic endoprostheses consist of an expandable metal structure covered with a layer of synthetic material - Polyethylene terephthalate (PET; eg. Dacron) or polytetrafluoroethylene (PTFE; eg. Teflon) - (see Figure 2.10).
Most of commercially available endografts for EVAR of abdominal aneurysms are currently in their third to fourth generation. Four generic schemes are currently available: straight aorto-aortic endografts, bifurcated systems, aorto-mono-iliac systems, and combined bifurcated and iliac branched stent endografts [Beard et al., 2013]. Traditional EVAR requires a healthy infra-renal proximal neck for graft fixation. Inadequate necks can cause endoleak or migration

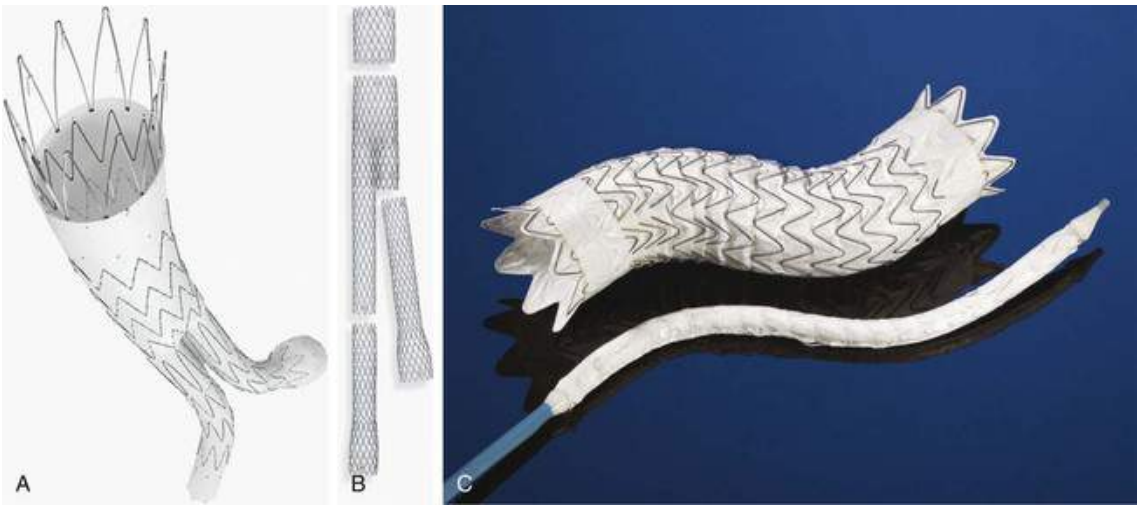


Figure 2.10: Most common endovascular devices: (A) Bifurcated Zenith endograft (Cook Medical, Bloomington, Ind.). (B) Bifurcated AneuRx endograft (Medtronic). (C) Excluder endograft (W.L. Gore & Associates, Flagstaff, Ariz.) expanded and constrained in its delivery sheath. Reproduced from https://radiologykey.com/aortic-endografting/ (courtesy of Cook Inc (A), Medtronic (B) and Gore (C)).

during follow-up. The use of fenestrated or branched endoprostheses, which have openings and branches in correspondence with the collateral arteries to preserve the vascularity, could be a solution when you are facing with aneurysms affecting parts of the aorta in which there are collateral branches (see Figure 2.11). The applicability of these types of endoprostheses is however still limited by the fact that they can not be used for emergency operations as they require careful study and a personalized design on the individual patient in order to be correctly implanted, resulting in longer times and higher costs.

### 2.4.1 Treatment of the aortic arch

The pathologies that include the aortic arch are therefore generally excluded for endovascular treatment due to an inadequate proximal landing zone and the risk of obstructing one or more supraortic trunks. However, the recent introduction of new approaches, which include the vascularization of the arch vessels (hybrid treatment) or the use of fenestrated custom-made devices or alternative endovascular techniques (chimney technique) to obtain adequate landing zones, has allowed the application of the endovascular techniques to be extended proximally to the aortic arch (see Figure 2.12). The hybrid treatment is the most widely employed technique in case of proximal landing zone in correspondence of the aortic arch.

The descending thoracic aortic aneurysms with a proximal neck$>$ 20 mm from the left

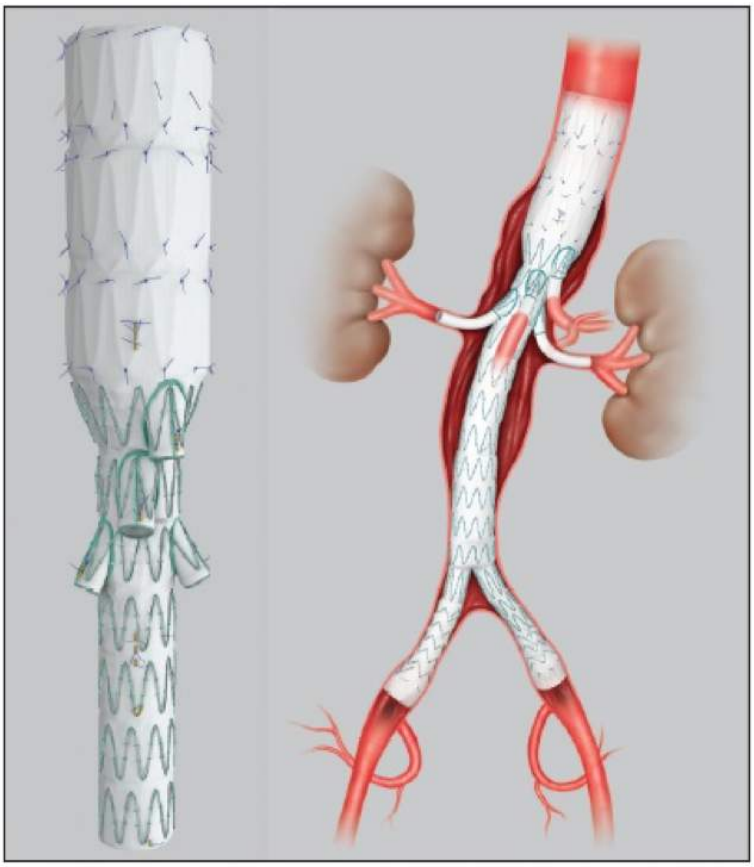

Figure 2.11: Branched Zenith t-Branch thoracoabdominal endovascular device (Cook Medical). Reproduced from evtoday.com (courtesy of Cook Medical).

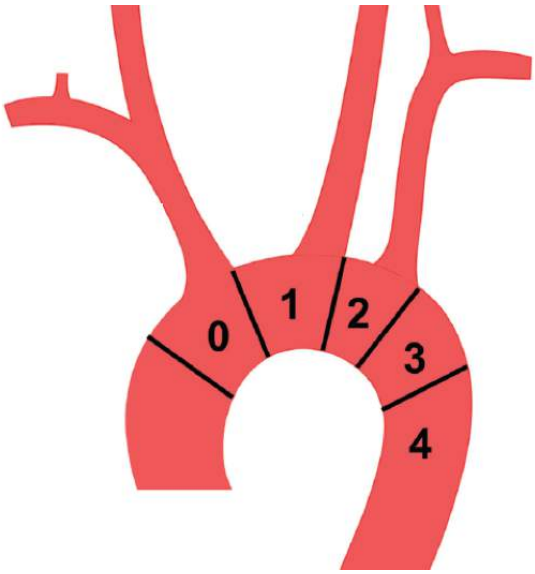


Figure 2.12: Proximal landing zone classification (Ishimaru). Reproduced from evtoday.com.

subclavian artery (landing zone 4 as depicted in Figure 2.12 represent an ideal situation for the placement of an endoprosthesis, the need for additional procedures on the left subclavian artery. Aneurysms involving zone 3 or 2 require coverage or transposition of the left subclavian artery instead with a carotid-subclavian bypass (see Figure 2.13). If the aneurysm involves the common carotid, a carotid-carotid bypass and a carotid-subclavian bypass should be performed to allow endoprosthesis positioning in zone 1 (see Figure 2.13). If the disease involves the aortic arch in its entirety and requires the coverage of the anonymous trunk, complete transposition of supra-aortic vessels should be performed (see Figure 2.13) to obtain positioning in zone 0.

## 2.5 Complications

The endovascular treatment of thoracic and abdominal aortic diseases has been definitely established as a valid alternative to conventional open surgery. Since this type of treatment is progressively more widespread, it is increased the amount of complications concerning the procedure, which in most cases are treated with endovascular procedures [Pratesi and Pulli, 2018].

The morphological parameters that must be evaluated in the follow-up are the absence or presence of endoleak, the size of the aorta, the morphology of the endoprosthesis, the diameter and morphology of the aortic landing zones and possible irregularities of the aortic wall. Furthermore, in patients treated for aortic dissection, it is essential to evaluate the perfusion

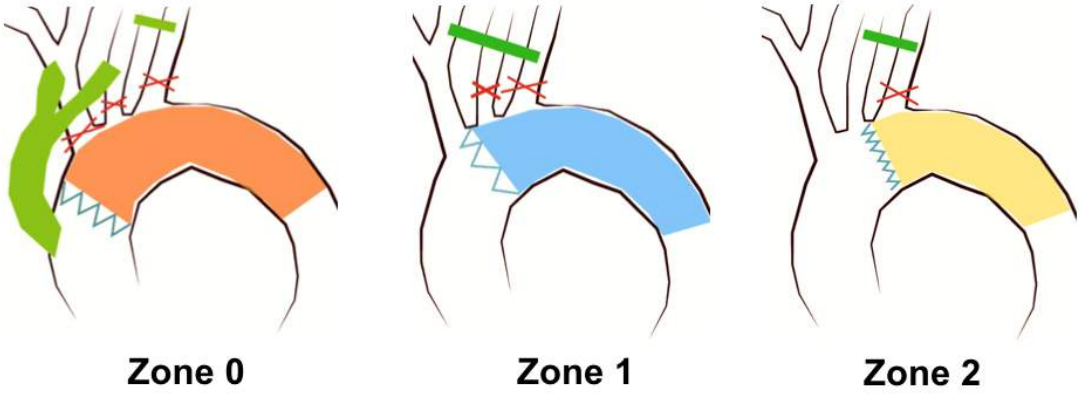


Figure 2.13: Schematic representation of debranching procedure for zones 0, 1, or 2 according to the Ishimaru classification. For each case, bypass is highlighted in green, while red crosses represent brachiocephalic trunk and left common carotid artery excluded by ligation or with plug occlusion in case of left subclavian artery.

of the vessels originating from the false lumen in order to avoid risk of malperfusion and ischemia.
Endoleak represents the most common complication after endovascular treatment of aortic disease, with a frequency ranging from 4% to 24%. Endoleaks are classified according to the site of origin at the level of the proximal (Type Ia) or distal (Type Ib) prosthesis landing zones. Proximal or distal endoleaks are due to an incomplete adherence between the prosthesis and the aortic wall, while the leakages at the middle of the prosthetic tract could be due to a retrograde flow through an aortic collateral (Type II) or a defect prosthetic (Type IV). Endoleaks can also originate from insufficient adhesion of overlapping features between two prosthetic elements (Type III). The persistence of endoleak is a sign of failure of the procedure and has important clinical repercussions, with potential risk of aortic rupture.

Retrograde aortic dissection, with involvement of the aortic arch and ascending aorta, represents a more obvious catastrophic event during the treatment of type B dissections or thoracic aneurysms. This complication could be associated with the use of a particularly rigid system especially in cases with severe aortic arch angulation. Retrograde aortic dissection, can also be caused by insertion of a prosthesis with excessive radial force that can cause tearing of the intima at the proximal landing zone. In these cases the new intimal lesion can be treated by the positioning of an additional prosthesis or by surgery.
Endoprosthesis migration is another possible complication (see Figure 2.15), sometimes favored by aortic remodeling that occurs following thrombosis of the aneurysmal sac. The

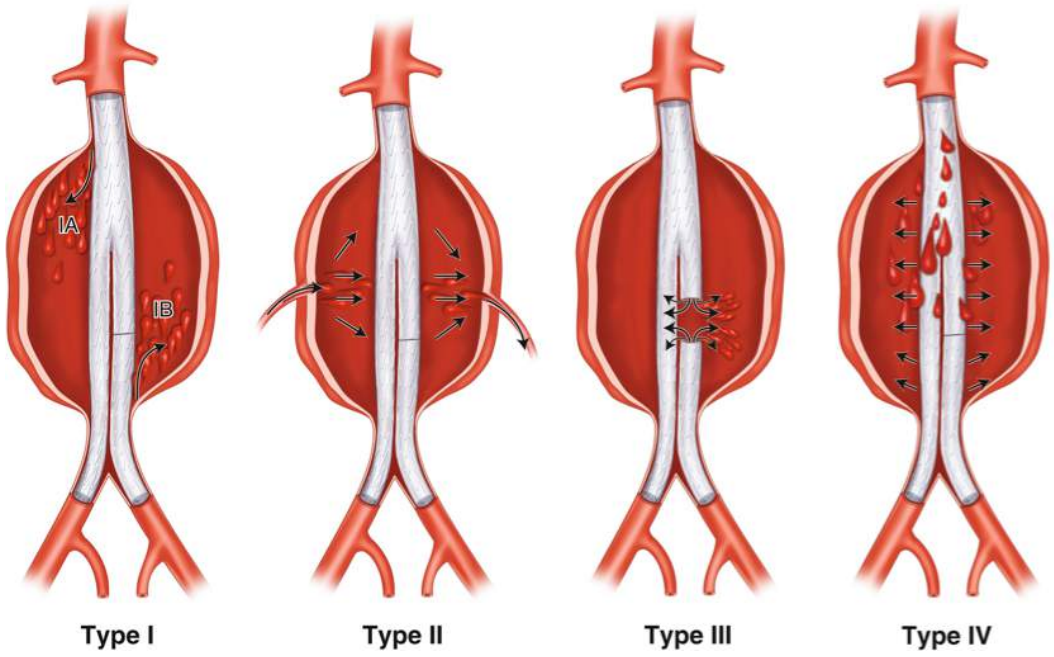


Figure 2.14: Endoleak classification system. Reproduced from [Gardner and Sabri, 2018]

prosthesis migration can cause not only leak but also occlusion of the main branches that originates from the aorta, with serious ischemic consequences.

## 2.6 Clinical diagnosis and medical imaging

Although all pathologies of the descending aorta can potentially be treated with endoprosthesis, not all patients are eligible for an endovascular procedure: vascular imaging is of crucial importance in identifying those patients with suitable anatomy, in the choice of the most suitable endoprosthesis (number of segments, size and extension) for the anatomy under investigation, and in the planning of the intervention modalities.

**Multidetector Computed Tomography (CT)** is the method of first choice in the evaluation of acute and chronic aortic diseases thanks to the ability to explore the entire thoracic-abdominal vascular district with images with high spatial resolution, in a few seconds and with a few dl of contrast medium. Since its introduction in the early seventies, CT has indeed revolutionized the field of diagnostic imaging allowing to capture detailed images, quickly and in a non-invasive way. From the pioneering tomographs, we have reached the modern multilayer CT, able to produce very high quality images of the entire body district with very short acquisition times, providing both anatomical and functional information, unthinkable until a

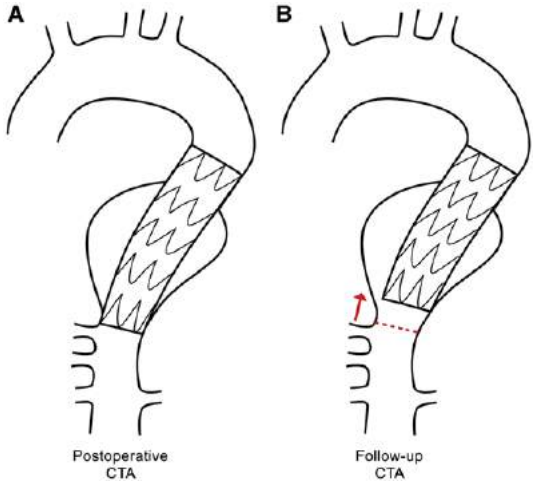


Figure 2.15: On the left correct apposition after surgery. Picture on the right shows that during follow-up endograft has migrated. Reproduced from Berezowski et al. [2017].

few years ago. Having therefore undergone a strong technological development, CT is today a fundamental investigation of use in the screening, diagnosis, therapy and management of patient care.

The basic principle on which the CT is based is composed of a rotating system (gantry) which consists of an X-ray tube on one side and a side of detectors on the opposite side: the rotation of this system around the patient allows to acquire the radiological image by assigning a gray value (from black to white) according to the density of each given point of the image. Multislice CT is today characterized by the presence of several detectors (currently 4 to 320) on the gantry arranged along the scan progress axis. In this way simultaneous acquisition of $n$ slices is obtained, which entails a $n$-times greater speed with the same parameters.

Thanks to the high speed of multislice CT, it is now possible to perform detailed studies of vascular structures without having to sacrifice spatial resolution. Furthermore, dedicated workstations for image processing have been developed as well.

**CT Angiography (CTA)** uses a CT scanning and an injection of iodine-rich contrast medium. CTA examination begins with a scan performed under basic conditions, before administration of the contrast agent, and it is useful for the evaluation of calcifications, for the detection of intramural hematomas and to better set the extent of the scan and the point on which to perform the bolus tracking, a system to monitor the amount of contrast that passes through the vessels, so as to scan when inside these has been reached maximum concentration of contrast medium. The phase of contrast agent administration is in fact the pivotal point for an optimal examination: the aim is to obtain a purely arterial impregnation (without venous or tissue contamination) synchronized with the scan.

CTA examination is essential in the preoperative planning of endovascular procedures to eval-

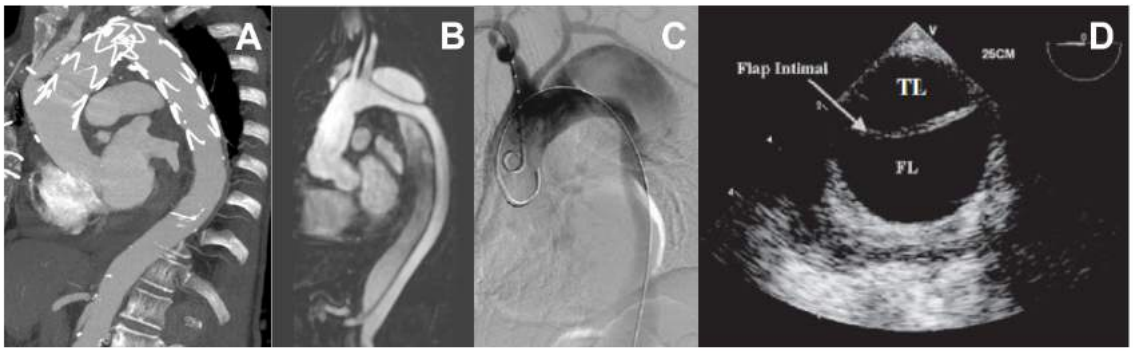


Figure 2.16: Examples of vascular imaging methods. (A) Post-operative CTA, (B) MRI showing a dissected aorta (reproduced from Sherrah et al. [2015]), (C) intra-operative angiography, (D) intra-operative trans-esophageal echocardiography which shows dissection intimal flap between true and false lumen (reproduced from Júnior et al. [2011]).

uate the extension in length of the lesion and to obtain images perpendicular to the major axis of the vessel that are usually adopted to perform measurements and, in particular, to determine an adequate prosthesis oversizing.

**Magnetic Resonance Imaging (MRI)** is also a valid method in the evaluation of aortic diseases, even if calcifications could not be visualized. The functional sequences and the detail provided by the angio-MR make it particularly useful in the study of aortic dissection.

Both CTA and MRI can be used in the postprocedural follow-up. Considering the best visualization at the CTA scan of the metal components of endoprosthesis, MRI is usually used only in cases of renal insufficiency or for radioprotective reasons (e.g., young patients). Post-procedural follow-up should be frequent in the first year, usually at 1, 3, 6 and 12 months, yearly thereafter.

**Angiography** is of fundamental importance during the endovascular procedure (fluoroscopy as a guide and angiography as a pre- and post-procedural control).

**Trans-esophageal echocardiography** provides a valuable, essential contribution during the endovascular procedure, particularly in the case of dissection. With this method it is in fact possible to distinguish in real time the true lumen from the false and verify the correct position of guide and catheter during the positioning of the endoprosthesis. After endoprosthesis release, the color Doppler allows to evaluate the absence or presence of flow inside the aneurysmal sac/ false lumen and the initial thrombosis of the excluded portion.

## 2.7 Analysis of biomedical images

### 2.7.1 Medical imaging pre-processing

The image processing allows to obtain clear and detailed images in order to capture information and the principal features for the analysis. For the 3D reconstruction of the anatomical structures of interest, the study of the images acquisition and the geometrical information that can be obtained from the segmentation are necessary.
The DICOM (Digital Imaging and Communication in Medicine) format describes how to compose messages to send between imaging modalities (for example CT, MR and ultrasound devices) and defines a standard for handling, storing, printing, and transmitting information. DICOM-formatted messages combine images and metadata to create a rich description of a medical imaging procedure.

### 2.7.2 Osirix Software

OsiriX is a free and open-source image processing application for Machintosh (Apple, Apple Inc.) dedicated to visualize anatomical DICOM data sets. This software has been developed using open-source libraries such as Papyrus Toolkit for DICOM files, PixelMed and DICOM Offis for DICOM network, the Visualization Toolkit for 3D rendering, and the Insight Toolkit for registration and segmentation. OsiriX has been specifically designed for navigation and visualization of multimodality and multidimensional images: 2D Viewer, 3D Viewer, 4D Viewer (3D series with temporal dimension, for example Cardiac-CT) and 5D Viewer (3D series with temporal and functional dimensions, for example Cardiac-PET-CT). The 3D Viewer offers all modern rendering modes: Multiplanar reconstruction, Surface Rendering, Volume Rendering and Maximum Intensity Projection.

### 2.7.3 VMTK

VMTK is a collection of open-source libraries and tools dedicated to the reconstruction of geometries and vascular surfaces. It is based on two libraries: VTK (the Visualization Toolkit) and ITK (the Insight Toolkit), also open-source and written in C ++, which respectively provide surface processing toos and the basic tools necessary for image segmentation. VMTK also works by exploiting a series of C ++ classes and scripts in Python, which allow to segment the image to reconstruct the geometries and perform geometric analyzes.
Most of the operations performed on the images in this thesis were performed using VMTK scripts.

### 2.7.4 Segmentation

Segmentation, ie the separation of structures of interest from the background or from other structures, is an essential analysis function for which numerous algorithms have been developed in the field of image processing. In medical imaging, the automatic delineation of image components is used to analyze anatomical structures and types of tissues as well as pathological regions.
In the literature, segmentation techniques are divided into several classes:

- Manuals, semi-automatic and automatic.
- Pixel-based and region-based.
- Manual delineation, low-level and model-based segmentation.
- Classical, statistics, fuzzy, and neuronal networks.

The most used techniques can be classified into two broad categories: (1) region-based segmentation that identifies regions that meet a given homogeneity criterion and (2) edge-based segmentation that searches for margins between regions with different characteristics. In the first case the identification is based on the intensity of the pixel or on other attributes such as the texture. Instead the techniques that localize the pixels of the contour use the concept of gradient of the image whose value increases at the edges.

#### Level sets segmentation

The idea behind the level set technique is to represent a surface that evolves during time:

$$S : \mathbb{R}^2 \times \mathbb{R} \to \mathbb{R}^3$$

as an isosurface of level $k$ (in this case we choose $k$=0) of a time dependent scalar function:

$$\Phi(x,t) : \mathbb{R}^3 \times \mathbb{R} \to \mathbb{R}$$

to that:

$$S(t) := \{x \in \mathbb{R}^3 \mid \Phi(x,t) = k\} \text{ with } k = 0$$

$S(t)$ is called *zero level sets* of $\Phi(x,t)$ and will identify the region of interest at the end of the segmentation process. The problem is therefore to find a stationary solution of the

time-dependent Partial Derivative Equation:

$$\begin{cases} \frac{\partial \Phi}{\partial t}(x,t) = -w_1 G(x)||\nabla\Phi|| + 2w_2\nabla\cdot\left(\frac{\nabla\Phi}{||\nabla\Phi||}\right)||\nabla\Phi|| + w_3\nabla P(x)\cdot\nabla\Phi, \quad (x,t)\in\mathbb{R}^3\times[0,T] \\ \\ \Phi(x,0) = \Phi_0(x), \qquad\qquad x\in\mathbb{R}^3 \end{cases} \tag{2.1}$$

To define the initial condition it is necessary to previously define a surface S(0) that approximates the volume of interest (the method to obtain such initialization is described in the following). $\Phi_0(x)$ is defined as:

$$\begin{cases} -D_0(x) \text{ if } x \text{ is inside } S(0) \\ +D_0(x) \text{ if } x \text{ is outside } S(0) \\ 0 \text{ if } x \in S(0) \end{cases} \tag{2.2}$$

where $D_0(x) = min_{y\in S(0)}\{\parallel x - y \parallel\}$.
Referring to the Equation 2.1, the terms $w_1, w_2, w_3$ are used-defined parameters. The first term of the Equation 2.1 is an *inflaction term* and $G(x)$ is called expansion speed and is defined as:

$$G(x) = \frac{1}{1+||\nabla\widehat{I}(x)||}$$

The surface expands along the normal direction to the zero level of $\Phi$, with a velocity normal to $G(x)$.
The second term is a penalization term that guarantees the smoothness of the surface, penalizing high curvatures.
The function $P(x)$ is called *attraction potential*:

$$P(x) = -\left\|\nabla\widehat{I}(x)\right\|$$

The third term of Equation 2.1 defined a convective term that drives the surface towards the edges.
This procedure is implemented in VMTK in the script `vmtklevelsetsegmentation`.
The level sets technique takes as input an image, which is used to initialize the level sets, and returns as output an image resembling the initial 3D image, but with values between -$X$ and $X$ ($X\in\mathbb{R}$ )based on the distance to the target surface, which has the value 0.

### Colliding fronts initialization

An adequate initialization of the surface $S(t)$ is fundamental in order to correctly extract the region of interest. One of the possible initialization is based on the *colliding front* method. The agorith starts by manually placing two seed points $P_i$ ($i = 1, 2$) within the lumen to

represent the extreme points of the region to be extracted. The algorithm then evolves with two independent wave fronts that propagate from each seed, with speed proportional to the local image intensity; i.e., solving the following Eikonal equation:

$$||\nabla T_i(x)|| = \frac{1}{1 + \widehat{I}(x)} \tag{2.3}$$

assuming $T_i(P_i) = 0$. Here $T_i(x)$ indicates the travel time of the wave propagating from the $P_i$ point and $I(x)$ the image gray-value. The initial level set function is the defined as:

$$\phi_0(x) := \nabla T_1 \cdot \nabla T_2 \tag{2.4}$$

Its value is negative wherever the two fronts face one another (region of initialization) and positive otherwise (see Figure 2.17). This allows to obtain an approximation of the desired segment of the vessel, also excluding other branches and the background.

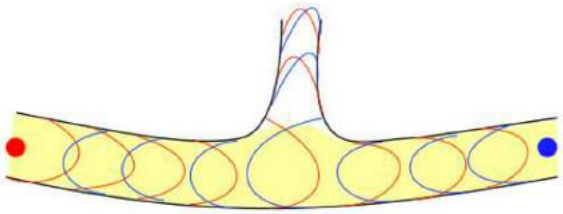

Figure 2.17: Colliding fronts initialization. The region of initialization is the region where the two wave fronts collide (yellow region).

### Custom Threshold initialization

In a second method of initialization implemented in the VMTK library, called *threshold initialization*, the initial level set is chosen as all pixels of the image between a lower and an upper threshold (chosen in Hounsfield Units - HU- ). Then the Equation 2.1 will evolve starting from such initialization surface.
This type of initialization method has been usually adopted in our work for the extraction of the stent metal rings from post-operative CTAs. However, the problem when dealing with threshold initialization is that the bones have an intensity (in terms of HU) similar to that of the metal graft and undesired entities will be therefore extracted. Therefore, for our purposes, we decided to customize the initialization step to avoid those drawbacks and automatically segment only the stent rings. A VTK-based Python code script was developed comparing the original CTA image with the image resulting from the level sets segmentation of the vessel lumen to produce a new image, ready for segmentation.

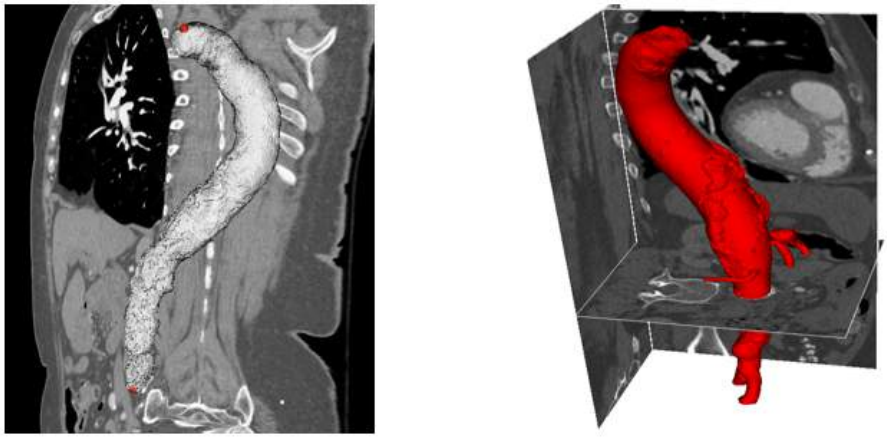

Figure 2.18: For the segmentation of the vessel lumen from contrast-enhanced CTAs we adopted the lsemi-automatic evel sets segmentation with colliding fronts initialization. On the left side the two seeds (red dots) from with the two waves front propagate are highlighted and the initialization surface is showed. The initialization procedure is then repeated for each branch. On the right side, the iso-surface of zero level is depicted.

Starting from two main considerations:

- recalling Equation 2.2, the level sets image is an image whose pixels are negative inside the surface boundary, positive outside and 0 on the boundary (see Figure 2.19);
- when nearing the boundary the pixels of the segmented image are approaching to 0;

and assuming that the stentgraft surrounds the vessel lumen, i.e. is sufficiently near to the boundary of the level sets image, in the new image we suppress (set to 0) all the pixels whose correspondent pixel in the level set image has intensity superior to a user-defined HU threshold (which should be set as a positive value), i.e. all the pixels sufficiently distant from the outer contour of the vessel.
Our script will then automatically pipes the `vmtklevelsetsegmentation` script with the threshold initialization algorithm allowing for automatical segmentation of metallic graft.

### Manual segmentation

Manual segmentation refers to a user-dependent process in which it is necessary to outline or fill regions of target structures on each image in an image stack in order to reconstruct

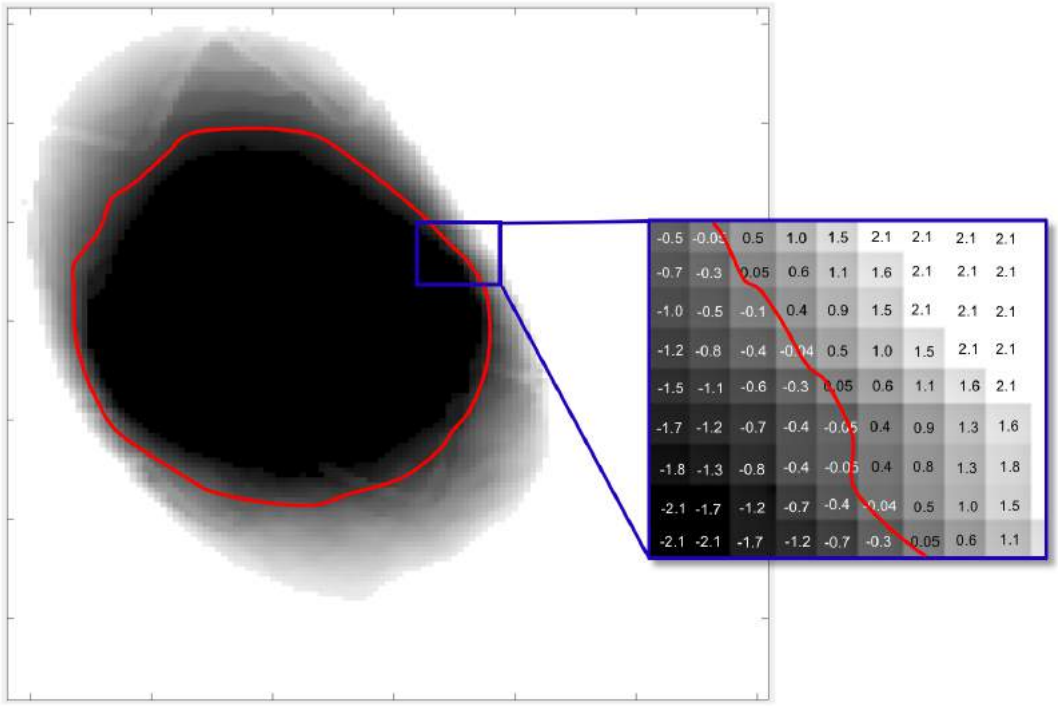


Figure 2.19: Slice of the level sets image with 0 level set highlighted with red curve. As depicted pixels are negative inside, positive outside and approach to zero near the boundary.

a 3D object. 2D manual contouring tools are needed in the context of non-standard tasks, e.g. when it is required to segment regions with low contrast with respect to the adjacent structures. Manual contouring might also be used to correct segmentations that result from sub-optimal automatic methods.
The drawback is that manual segmentation is a very time consuming procedure that requires a big amount of user interaction.
Different software for medical image processing allow manual segmentation. In particular, in this thesis work we made use of a semi-manual segmentation procedure implemented in the MITK software (www.mitk.org). This tool allow to discern the manually define the contour of the anatomical structure in a reduced number of slices; the 3D surface interpolation using radial basis functions allow to correctly reconstruct the object in 3D.

### 2.7.5 Surface preparation

Once the segmented image is obtained, it is converted into a 3D surface with the marching cubes algorithm, originally proposed by Lorensen and Cline in 1987 [Lorensen and Cline, 1987]

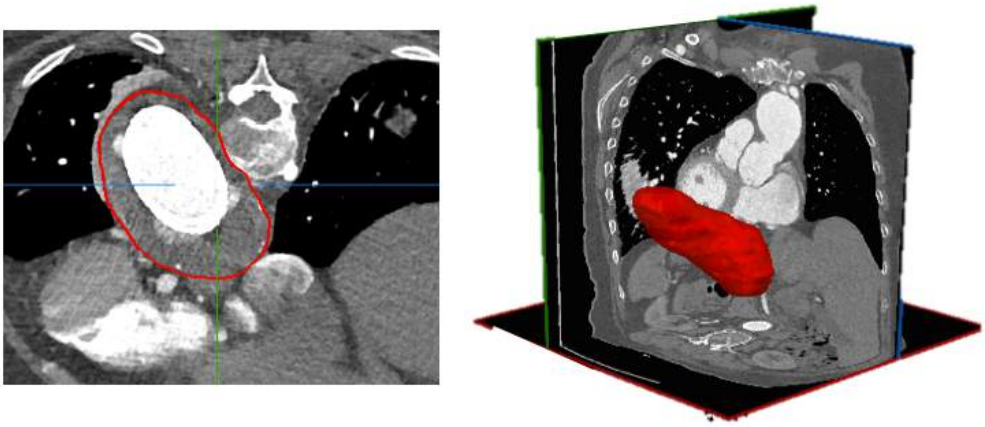

Figure 2.20: Segmentation of the aneurysm external wall which required a 2D manual segmentation due to the low contrast of the thrombotic region in comparison with the adjacent anatomical structures. On the left side of the image we can see manual delineation of the contour of the structure on a single slice; on the right the final 3D object (aneurysm) is reconstructed.

and implemented in the VMTK library. This algorithm returns an initial polygonal surface that, however, is not directly suitable for image analysis due to an insufficient triangle quality. Hence, surface meshes need to be improved with smoothing filters and remeshing operations. In our work, between the existing smoothing filters, we always made use of the global smoothing filter based on the algorithm described by Taubin [Taubin, 1995] and implemented in VMTK which is not affected by shrinkage-related problems. Moreover, remeshing operation is performed to obtain a new mesh that will maintain the same topological characteristics of the original mesh but with higher quality of the triangles and well organized vertices. The method we adopted is implemented in VMTK and surface triangles are resized according to a user-defined target edge length which is uniformly assigned to the whole surface.
When there is the necessity to quantitatively compare surfaces which are reconstructed from images with different reference system, e.g. geometries segmented during different follow-up times, surface registration should be performed. The registration algorithm implemented in VMTK is based on the Iterative Closest Point (ICP) algorithm [Besl and McKay, 1992]. The core of the algorithm is to minimize the difference between two clouds of points: one point cloud (reference) is kept fixed whereas the other one (source) is rigid transformed to best match the reference. The transformation is iteratively revised to minimize an error metric in order to get proper convergence of the surfaces.

### 2.7.6 Vessel topology characterization

Once obtained the 3D surfaces of interest, it is necessary to describe the geometry itself with a series of local and global synthetic descriptors. The choice of the geometrical features to be extracted depends on the application and on the aim. When dealing with blood vessels, quantitative geometric analysis of vessel geometry is an important step for the quantification, the diagnosis, and the monitoring of vascular diseases. Vessel descriptors could be useful for simulation aims as well.

### 2.7.7 Centerline computation

One of the most powerful descriptors to describe the shape of the vessels is the centerline which could be defined as the shortest line drawn between a starting inflow section and one or more outflow sections that locally maximizes the distance from the walls. Lots of methods for the centerline extraction of medical entities have been proposed so far, both from medical images and from 3D models. The algorithm implemented in VMTK is based on the analysis of a 3D object and has the advantage to be quite stable to perturbations on the surface.
As extensively reported by Antiga et al. [Antiga et al., 2003], the computation of the centerline inside an object $\Omega \subset \mathbb{R}^3$ with boundary $\partial\Omega$ results in finding a path $C = C(s)$ (where $s$ is the curvilinear abscissas) between two extremal points $p_1$ and $p_2$ that minimizes the energy functional:

$$E_{centerline}(C) = \int_0^L F(C(s))ds \tag{2.5}$$

Considering, for any point $x \in \Omega$ , the scalar field $F(x) = DT^{-1}(x)$ and $DT(x)$ a decreasing function of scalar transform defined as:

$$DT(x) = \min_{y \in \partial\Omega} \{dist(x, y)\} \tag{2.6}$$

the centerline defined in Equation 2.6 lies on the medial axis of $\Omega$ which is the locus of points equidistant from the boundary $\partial\Omega$. To define an approximation of the medial axis of $|Omega$ it is necessary to introduce the concept of Voronoi diagram of a set point $P$:

$$Vor(P) = \bigcup_{p \in P} \partial V(p) \tag{2.7}$$

where $V(P) = \{x \in \mathbb{R}^3 \mid dist(p, x) \leq dist(p, P)\}$ is the Voronoi region associate with point p, i.e. the region of $\mathbb{R}^3$ whose points are closer to $p$ than other other point included in $P$. The Voronoi diagram os a surface made of convex polygons whose vertices are the centers of the maximal spheres with radius $R(x)$.
Computation of the Voronoi diagram is performed by first computing its dual, i.e. the Delaunay tessellation of $P$, $Del(P)$. Then, removal of the tetrahedra whose circumcenter falls outside the object and the reconstruction of the Voronoi polygons whose vertex are complete

is performed.
The problem of Equation 2.5 is then solved on the embedded Voronoi diagram assuming $F(x) = R^{-1}(x)$.
The strong formulation of the Equation 2.5 is defined as:

$$| \nabla T(x) | = F(x) \tag{2.8}$$

with $T(p_0) = 0$ as boundary condition. Following [Antiga et al., 2003] the equation is solved by the Fast Marching Method extended to polygonal non-manifolds. Once the Equation 2.8 is solved on the whole Voronoi diagram, centerline path is obtained from $p_1$ following the direction of maximum descent of $T(x)$.

#### Centerline post-processing

Centerlines could be affected by noise and sudden changes of directions. Therefore, before any further analysis, resampling and smoothing of the centerlines are of fundamental importance in order to perform robust and repeatable geometric analyses. Moreover, when dealing with mutual comparisons of pre- and post-operative centerlines parameters, we have the necessity to obtain centerlines with the same number of points. Therefore, for the resampling step, we introduced an in-house VTK-based Python code which finds a cubic B-spline representation of a N-dimensional curve with a user-given sample size. To obtain a smoothed representation of the centerline we moreover apply a Laplacian smoothing filter.

### 2.7.8 Geometrical analysis

When dealing with the analysis of lumen vessels (e.g. the aorta) could be necessary to obtain the lumen surface without collateral branches: in the bifurcation zones, in fact, measurements on sections could be influenced. Such operation, already implemented in VMTK is performed in 3 steps: centerline computation, branch splitting (e.g. subdivision of the surface on the regions corresponding to the bifurcations and main lumen extraction), and interpolation of the holes. Quantification of the vessel volume could be automatically performed starting from the surface of the vessel and could be an important parameter to be computed when performing a comparison of patient's vasculature during follow-up time. Centerline could be also used to obtain cross-sections of the vessel surface perpendicular to the centerline itself and to compute the measurements on every section. By means of the VMTK script `vmtksurfacesections` maximum diameter, minimum diameter, area, and shape index (computed as the ratio between the maximum and the minimum diameter) are automatically retrieved.

**Quantitative Centerline characterization**

Automatic computation of the centerline length is an important parameter to be addressed. The length of the centerline between two arbitrary points $a_1$ and $a_2$ lying on the centerline is defined as:

$$l(a_1, a_2) = \int_{a_1}^{a_2} sds \tag{2.9}$$

Besides being useful for the correct sizing of the endograft, in our study we make use of centerline lengths (both total centerline length and also computation of distances on the centerline between points of interest) for comparisons between pre-operative and post-operative centerlines. Vessel tortuosity and point-wise curvature could be seen as important metrics to indicate a possible pathology development. The tortuosity index is presented as a global parameter which can provide useful information about the overall shape of the vessel. On the other hand, curvature values are computed for each point of the centerline allowing to capture the local and complex bahavior of the vessel.
Tortuosity index is defined as: $T = L/CVD - 1$, where $L$ represents the centerline length and $CVD$ is the Euclidean distance between the endpoints of the centerline. This parameter quantifies the fractional increase in length of a tortuous lumen vessel when compared to a perfectly straight one.
Curvature, at a given point, is computed as the inverse of the radius of the local osculating circle, i.e. the circle approximating the curve in the given point. It is mathematically expressed by the following equation:

$$\kappa(s) = \frac{|c'(s) \times c''(s)|}{|c'(s)|^3} \tag{2.10}$$

where $c(s)$ is the line and $s \in [0, L]$ the curvilinear abscissa previously defined in Equation 2.5; with L=total centerline length. From this definition, the value of curvature, at a certain point, quantifies its deviation from a straight line.

### 2.7.9 Parent vessel reconstruction

In this section we will explain how to retrieve a virtual 3D surface model removing the saccular aneurysm from its parent vasculature. The framework of the algorithm has been originally proposed from Ford et al. [Ford et al., 2014] for the removal of intra-cranial aneurysms and implemented in VMTK by M. Piccinelli. The algorithm implemented in VMTK has been partially modified for our purposes (contribution by Eng. Elena Faggiano). The algorithm is based on the definition of Voronoi diagram and, in particular, on the property that allows to derive the Voronoi diagram given the model surface and viceversa. Starting from the vessel surface, the Voronoi diagram was firstly computed using a script already implemented in the VMTK library. Then, two couples of centerlines are extracted by manually placing seeds

on the model. The first couple is extracted from the surface model from the input section (proximal section of the vessel) to the top of the aneurysm sac and to the output section (distal section) and defined the forward direction. The second couple of centerlines is extracted from the output section (distal section) to the top of the aneurysm sac and to the input section (proximal section) in the backward direction.
The removal of the saccular aneurysm is then performed in three steps:

- Identification of the centerline points that define the area of influence of the sac, removal of the portion of centerline between this two extreme points and creation of a new interpolated parent artery centerline (see Figure 2.21). Differently from the original algorithm already implemented in VMTK which automatically identifies the points delimiting the sac on the centerline, our script was modified allowing for manual picking of the two points directly on the vessel centerline.

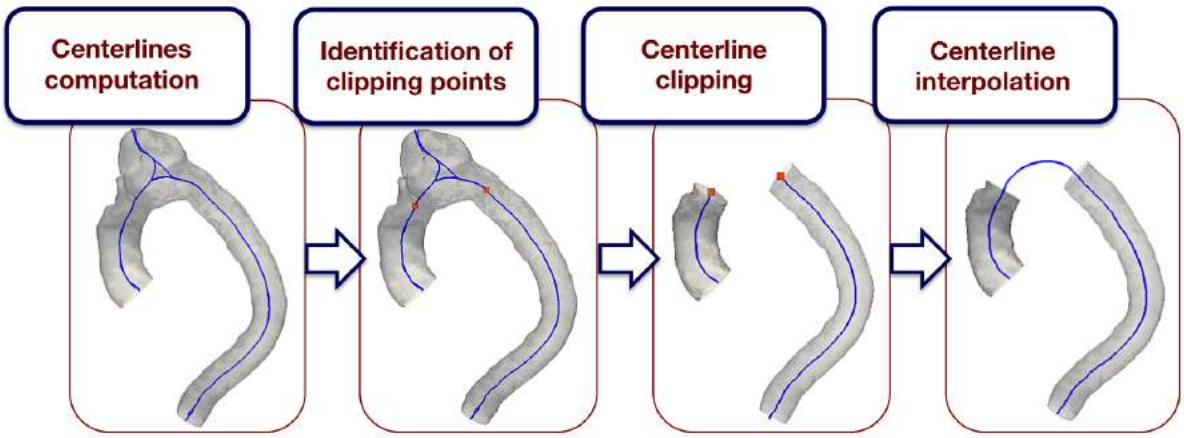


Figure 2.21: Starting from computation of two couples of centerlines, manual identification of the two extreme points defining the aneurysm sac, removal of the portion between these two points and creation of the parent artery centerline are performed.

- Removal of the Voronoi Diagram pertaining the portions related to the aneurysm sac.

- Interpolation of a new Voronoi Diagram for the portion of artery where it has been removed (see Figure 2.22) by paralled transporting the Voronoi points following the trajectory of the new interpolated centerline and reconstruction of the new parent vessel model surface.

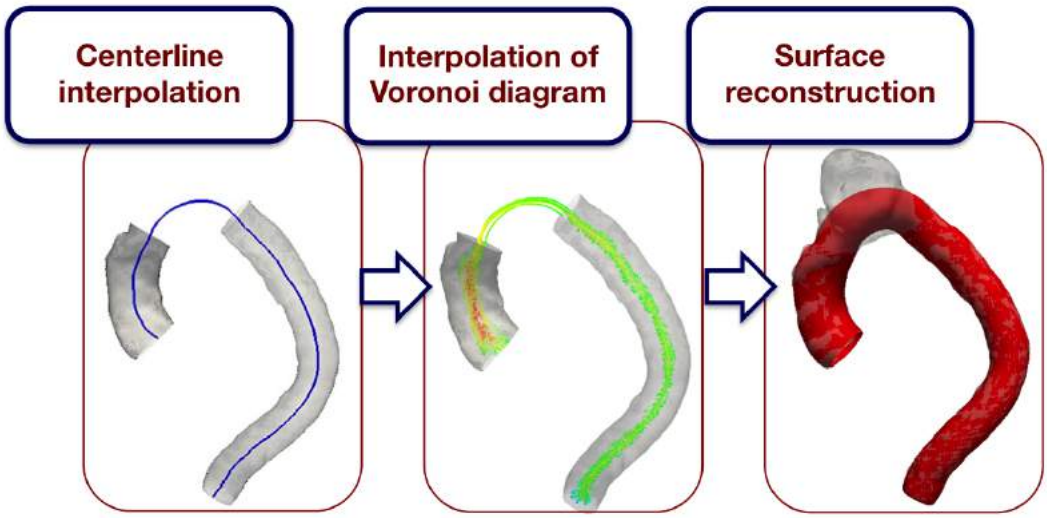


Figure 2.22: Reconstruction of a new Voronoi diagram and of the parent vessel surface. The reconstructed parent vessel surface is in red whereas the original surface is in white.

### 2.7.10 Vessel surface outer contour lines

Some studies claim the superiority of surface outer contours paths in comparison to the centerline path. For example, the work of Kaladji et al. [Kaladji et al., 2013] demonstrated that the use of centerline length instead of outer surface length in endovascular planning usually lead to underestimation of the length of the required endograft.
Parametrization of tubular surfaces starting from meshes has been extensively reported in literature.
The method we implemented is based on computing a harmonic function with extremal on branch boundaries. An in-house VTK-based Python code (in collaboration with Eng. Elena Faggiano and Eng. Margherita Coda, CompMech Group, University of Pavia) was developed that performs computation of harmonic mapping by solving La Place equation with temperature imposed at boundaries (Dirichlet boundary conditions). In particular, we imposed 0 temperature at outlet and 1 at inlet. The algorithm then performs steepest gradient descent from boundary with temperature 1 downward to temperature 0, along diffused temperature values. At the end, we obtain a user-defined number of equidistant outer contours laying on the surface of the vessel.
For our purposes, the script will then automatically compute the length of the surface outer contours and extract the paths characterized by the maximum and minimum length (outerline and innerline in the following of this thesis). In Figure 2.23 an example of outer contour lines

is given for a thoracic aorta surface.

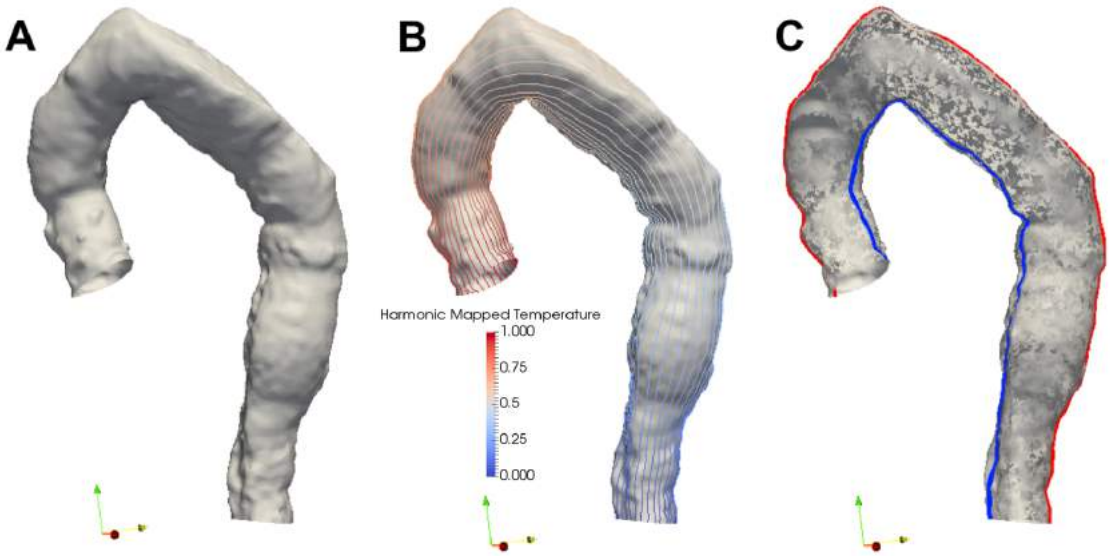


Figure 2.23: Example of outer contour lines computation. (A) starting surface, (B) surface outer contours colored according to temperature values (from inlet=temperature 1 to outlet=temperature 0). (C) Innerline (blue) and outerline (red) are automatically detected.

# Chapter 3

# Thoracic aorta remodeling after endovascular treatment: literature review

The endovascular treatment has allowed to change radically the results of the therapy of thoracic aortic diseases in reducing mortality and postoperative complications. Unfortunately, the reinterventions rate after TEVAR are the Achilles' heel of the endovascular treatment. In particular, the development of endoleaks, infections and dissections might lead to re-interventions. Therefore, following endovascular treatment, aortic remodeling is one of the main factors that should be considered when evaluating the outcomes.
Two types of aortic remodeling can be considered: one can consider remodeling as the shrinkage of the aneurysmal sac or false lumen thrombosis in case of treatment of aortic dissections. Conversely, aortic remodeling can be seen as the changes occurred in the aortic morphology following endograft placement, which could be related to the onset of complications.
In the following we present a short literature review on aortic remodeling after TEVAR in both aneurysmal pathology and aortic dissections.[1].

## 3.1 Literature overview

To this day, the evolution of aortic morphology after TEVAR is a subject of strong debate and there is little scientific evidence on it, even if recently numerous interesting analyses have been proposed, based on complex medical images processing, mechanical tests and fluid dynamics. The main aortic arch and thoracic aorta pathologies the vascular surgeon deals with are aneurysm, acute or chronic dissection, penetrating aortic ulcer and intra-mural hematoma.

[1]This chapter is based on:

- Palombo D, Spinella G, Gazzola V, Finotello A, Mambrini S, Conti M, Auricchio F, Pane B. "Thoracic aorta remodeling after endovascular treatment" in Aortic Complexities, Edi.Ermes

Each of these pathologies shows peculiarities from a morphological and anatomopathological point of view. As a consequence, the evaluation of post-procedural aortic evolution is complex and must take into account several elements.
In the literature we find several reports, including meta-analyses evaluating the evolution of the aorta after TEVAR for type A and B aortic dissections, acute and chronic; conversely, the results of remodeling after aneurysmal pathology treatment are still few.
The endovascular treatment of aortic dissections aims at reducing the false lumen perfusion by excluding from the circulation the main dissection lamella proximal tears in order to promote aortic remodeling with true lumen re-expansion and, at the same time, to maintain the collateral branches vascularization (supra-aortic, spinal, splanchnic and renal vessels). As discussed in the previous Chapter, the indication for the treatment varies depending on the site and on the extent and gravity of the pathology. For type A aortic dissections the reparative intervention is mandatory and must be performed in an emergency regime; on the other hand, for type B aortic dissections an indication for intervention is necessary in case of complicated pathology. Therefore the key to the success of treatment itself lies not only in the resolution of the "acute" clinical conditions, but in promoting a remodeling of the pathological aortic morphology towards a situation that stabilizes over time, thus ensuring that the vessel functions are as physiologically as possible [Conrad et al., 2009] .
We can doubtlessly state that the main factor to be considered for evaluating the evolution of the morphological clinical response is the progression of the dissection. Therefore, particular attention should be paid to the development of a retrograde dissection, which is a strong negative prognostic factor, or to the progression of the anterograde dissection propagation, that instead constitutes an increased risk for future reinterventions.
The second important element in the outcome of this category of patients is the evolution of the true and false lumen relationship. As described by several authors, the endovascular treatment long-term efficacy is linked to the persistent post-procedural patency of the false lumen. In this regard, Matalanis et al. [Matalanis et al., 2016] have provided an exhaustive description of the evolution of the treatment of type A dissections, due to the necessity of achieving a complete false lumen thrombosis after treatment.
Literature data show that after surgical correction of acute type A dissection the false lumen in the descending aorta remains patent in a variable percentage between 50% and 80% of cases. 15-60% of these patients will undergo an aneurysmal evolution within 10 years and 25% of them will have to undergo a complex reintervention [Park et al., 2009].
Even in the case of type B dissection, the ultimate goal should be to obtain false lumen thrombosis, in order to ensure a "positive" remodeling of the aorta during follow-up. Despite the lack of literature data on morphological changes after endovascular treatment of type B aortic dissections, the meta-analysis performed by Patterson et al. [Patterson et al., 2014] has demonstrated that patients undergoing TEVAR are more likely to encounter a reduction in the false lumen diameter and a consequent re-expansion of the proximal true lumen between 36 and 48 months after treatment: 80-90% of acute cases vs 38-90% of chronic cases. Interestingly, they have shown that the persistence of false lumen perfusion is associated with disease

progression and that such patients will undergo during time a maximum increase of aortic diameter equal to 65%, if compared with the initial one. The study concluded that, albeit data were not definitive, aortic remodeling with reduction of the false lumen correlated with an increasing survival in the medium term and with a decreasing aneurysmal evolution of the descending and abdominal thoracic aorta and lower incidence of endoleak or distal reperfusion and resultant re-interventions. It also emphasized that remodeling is greater in those patients treated in acute basis compared to the ones treated for chronic dissection in the form of significant reduction of false lumen and increase of the true lumen after intervention.The presence of a thicker fibrous dissection septum with multiple large tears would indeed make the aorta less susceptible to morphological changes.

In order to promote aortic remodeling in the acute type B aortic dissection and to avoid follow-up reinterventions, some authors suggested using the provisional extension to induce complete attachment (PETTICOAT) technique. However, in spite of early positive results, the aortic diameter continued to expand during the follow-up. This result seems to suggest a careful consideration regarding the use of PETTICOAT technique, as it would not seem to protect the dissected aorta from aneurysmal dilatation during the follow-up. For this reason, some authors have suggested using a bare stent associated with the dissected aorta ballooning to facilitate the attachment of the dissected lamella to the remaining part of the aortic wall. Recently, Melissano et al. [Melissano et al., 2018] have shown a preliminary experience with this procedure achieving an excellent aortic remodeling, even if these patients have had a short follow-up with a mean time of 7.2 months only. The authors have observed no complications and the complete exclusion of the false lumen in all cases.

The endovascular approach in patients with thoracic aortic aneurysms is based on different concepts and is based on the necessity to exclude completely the aneurysmal aorta from the circulation. The prerequisite for a successful treatment is therefore to obtain an adequate sealing of the endoprosthesis both on the proximal and on the distal aortic neck; whereas the subsequent aortic remodeling is of secondary interest, as the sac diameter reduction, although desirable, is not indispensable for the success at long-term follow-up. On the contrary, the aortic remodeling after TEVAR, particularly in correspondence of the landing zones, can cause the procedure failure if the aortic neck dilatation affects the previously obtained seal, with the consequent development of type I endoleaks.

In spite of the recent growing interest in aortic remodeling after treatment of aortic dissections, specific information about the morphological remodeling of the aneurysmal sac after TEVAR are few.

As stated by Moulakakis et al. [Moulakakis et al., 2015] the motion of the aneurysmal sac wall after endovascular repair reflects complex interactions between the components of the excluded aneurysm tract, including compliance of the wall itseft, intra-aneurysm sac pressure, and remodeling of the thrombus.

Nomura et al. [Nomura et al., 2015] reported the outcomes of a volumetric and diametric analysis of 44 cases using CTA scans. They conclude the superiority of pre- and post-operative volumetric analysis in comparison with the standard analysis of diameters to investigate the

remodeling of the aneurysm sac and thrombus. In particular, volumetric analysis after TEVAR was able to predict the presence of endoleak and that an increased aneurysm volume correlated with a greater probability of high pressure endoleak.
Moreover, when TEVAR is used to treat Intramural hematoma (IMH) or penetrating atherosclerotic ulcer (PAU) a significant vascular remodeling has been observed, with normalization of the aortic diameter at 1 year follow-up [Lavingia et al. [2014]; Sueyoshi et al. [2014]].
However, as previously discussed, one of the main limitations of endovascular repair is the high rate of reinterventions during follow-up recommending lifelong follow-up imaging. The remodeling of the anatomy of the aorta after TEVAR can therefore be considered with a negative meaning of the term. Sac enlargement, aneurysmal degeneration, and the presence of endoleak should be accurately assessed.
In 2014, Alberta et al. [Alberta et al., 2014] have analyzed the evolution of aortic necks after endovascular treatment and identified a correlation between the percentage of endograft oversizing and the aortic dilatation in the proximal (6.9% increase in diameter) and distal landing zones (increase of 2.7 %).
Moreover, the article by Hassoun's group [Hassoun et al., 2006], published in the Journal of Vascular Surgery, albeit dating back to 2006, demonstrated a statistical significant increase in the aortic neck diameters after TEVAR compared to pre-operative values. In particular, 6 months after the procedure, an average increase of $1.8 \pm 0.2$ mm and $2.7 \pm 0.5$ mm was recorded respectively for the proximal and distal landing zones. Furthermore, this study highlights an aortic neck expansion that continued during the firsts 3 years follow-up, even if only in a small percentage of cases the evolution was significant (i.e. more than 5 mm) and leaded to endograft migration and endoleak development.
In last years, however, several studies have made use of advanced techniques of medical images processing and analysis (i.e. CTA, MRI) together with specific analyses on post-TEVAR aortic mechanics modifications and fluid dynamics. In this context, the study of Nauta et al. [Nauta et al., 2017] has demonstrated that the positioning of a thoracic aortic endoprosthesis creates a zone of greater rigidity, preceded and followed by much more elastic segments of aorta. The elasticity mismatch between these contiguous segments is thought to be the basis of the proximal and distal landing zones aneurysmal degeneration and, less often, of the endograft tract retrograde dissection upstream. The increase of the longitudinal tension reached a statistical significance in the aortic arch, with a growth of 77%. Such result, once again, shows that the aortic arch is the most critical zone in the treatment of thoracic aortic pathologies.
In a recent study, Midulla et al. [Midulla et al., 2014] of pointed out how the impact of TEVAR on aortic function and on aortic morphology is little known. In particular, a pre- and post-operative patient-specific comparative analysis focused on the device implantation site was presented and 30 cases were investigated. The results showed that in about half of the patients (47%) a change in the aortic geometry was recorded, 78% of which presented the proximal landing zone at the level of the arch.
Naguib et al. [Naguib et al., 2016] focused on the long-term changes in aortic length after TEVAR for thoracic aortic aneurysms and dissections. They found that the increase of the

aortic length in the longitudinal direction reached significance 1 year after endovascular treatment. Such outcomes should be taken into account in the planning secondary interventions. More recently, also Mestres et al. [Mestres et al., 2017] have proposed an interesting study based on manual measurements on 36 cases analyzing the aortic arch curvature and its remodeling after TEVAR. However, up to day very few of such studies attempted to relate negative aortic remodeling to clinical outcomes and complications development during follow-up.

## 3.2 Conclusion

As concerns the positive remodeling of the aorta, especially in the treatment of dissections and the remodeling of true and false lumens, so much has been written. In the recent years, however, attention has focused on the "negative" remodeling that occurs in the aorta during follow-up, asking how this remodeling is correlated with the development of complications during follow-up. Just to understand if such negative remodeling takes place and why this happens is the basis of research in recent years and could be useful to conceive a new generation of prosthesis that reduces the risk of complications during follow-up.

# Chapter 4

# Medical image analysis to measure the follow-up geometrical changes of TAA aneurysms treated with MFM stent

In this chapter I will expose a project developed during the PhD program regarding the Multilayer Flow Modulator (MFM), a novel device for the endovascular treatment of aortic pathologies. First, the concept of multilayer flow modulator will be explained and literature on MFM device will be reviewed; then our study about geometric analysis of the follow-up changes after MFM implantation will be presented. [2]

## 4.1 MFM device

### 4.1.1 The concept behind the MFM

The MFM is composed by a self-expandable three-dimensional braided structure (see Figure 4.1) which forms a mesh with a specific porosity and permeability (60% to 70%). Translating the concept of flow-diverting stents from intracranial aneurysms, the MFM device is not intended to isolate the aneurysmal area from the circulation but to re-establish a physiological

[2] This chapter is based on:

- Spinella G, Finotello A, Faggiano E, Pane B, Conti M, Gazzola V, Auricchio F, Palombo D. Mid-term follow-up geometrical analysis of thoraco-abdominal aortic aneurysm treated with multilayer flow modulator. Annals of Vascular Surgery 2018; 53: 97-104.
- Faggiano E, Spinella G, Fedele M, Finotello A, Conti M, Pane B, Perfumo MC, Auricchio F, Palombo D. "The theoretical and experimental basis of the Multilayer Flow Modulator" in Palombo D., Pane B. , Spinella G. Editor. The current role of Multilayer Flow Modulator Stents in Complex Aortic Pathology. Torino: Edizioni Minerva Medica; 2017, ISBN: 978-88-7711- 891-2.
- Finotello A, Faggiano E, Conti M, Spinella G, Pane B, Palombo D, Auricchio F. Medical image analysis to measure the follow-up geometry of thoraco-abdominal aortic aneurysms treated with multilayer ow modulator stent. CMBBE: I & V. Revision submitted.

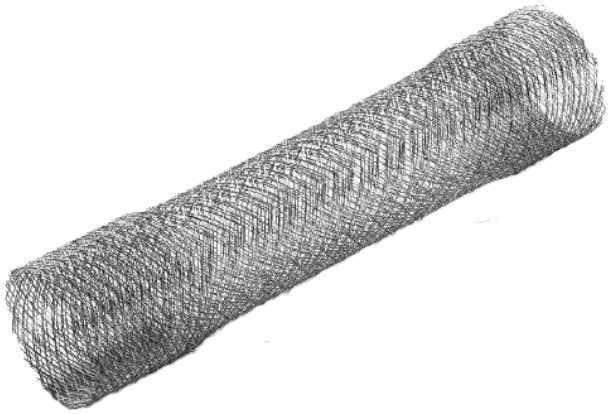

Figure 4.1: Multilayer Flow Modulator for aortic treatment

flow leading to gradual healing of the artery. The MFM has a compliance similar to that of the native aorta, diminishing the problem of peak wall stress in the aneurysm by laminating the flow [Sultan et al., 2014a]. The innovative idea behind MFM is to deploy a device covering both ends of the aneurysm that will work as a "windbreak" able to:

- regularize the blood flow, eliminating or reducing the recirculation in the aneurysm sac;
- promote an organized thrombus as well as promote generation of new endothelium along the MFM inner layer;
- maintain perfusion of all collateral branches.

**Fluid dynamics changes induced by the MFM.** Working like a windbreak, the MFM aligns the flow inside the aneurysm sac. After passing through the MFM, the blood flows along the wall in the same direction as the systemic pressure flow, eliminating turbulence and flow vortices [Xenos et al., 2015]. In fusiform aneurysms treated with the MFM, the flow enters the sac from the proximal part of the vessel segment and exits from the distal part; with laminar redirected flow (see Figure 4.2A-C) [Sultan et al. [2014a]; Heisler and Dewalle [1988]; Polydorou et al. [2010]]. Lamination of the blood flow generates fine layers of thrombus. In saccular aneurysms, MFM implantation completely changes the dynamics within the sac, decelerating the flow in the sac, breaking the vortex and reducing its strength by inverting its

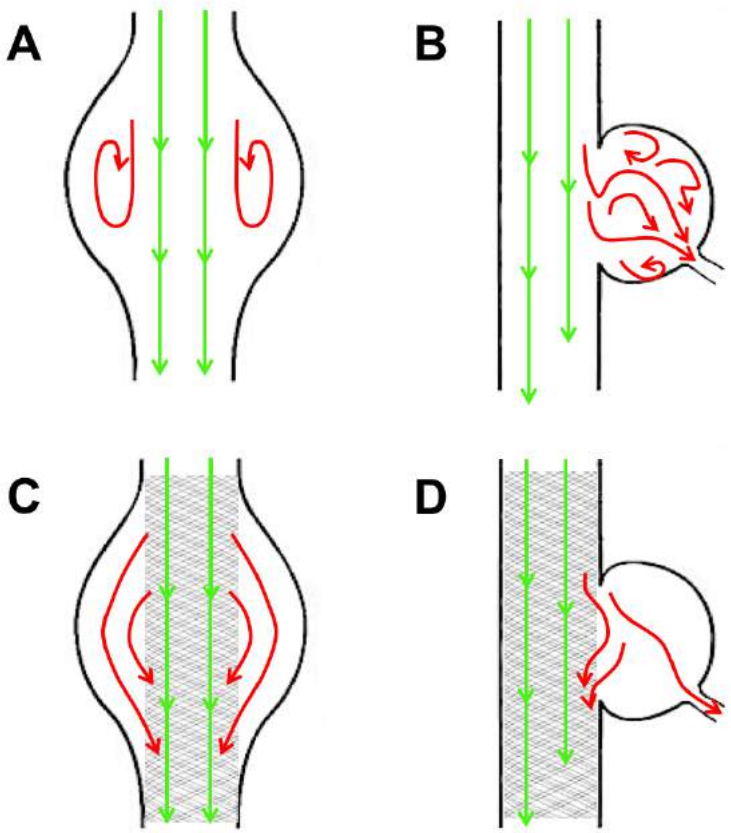


Figure 4.2: Schematic illustration of the irregular flow in fusiform (A) and saccular (B) aneurysms and of its regularization after MFM implantation (C, D).

trajectory [Sisto et al., 2015]. The time of blood residence in the aneurysm is increased, with the effect of slowing and realigning the vortex, promoting creation of a thrombosed layer leaded by stagnant blood flow within the aneurysm. Flow regularization and consequent structured thrombus formation will prevent aneurysms from rupture.

**Intraluminal thrombus formation.** By reducing blood velocity inside the aneurysm and laminating the flow, the MFM promotes the formation of an organized thrombus [Sultan and Hynes, 2012]. Again, the role of the thrombus concerning the risk of rupture is controversial. Although the possibility that the presence of intraluminal thrombus can act positively on the aortic wall is still debated [Vorp et al., 2001], in recent years several studies shown that the presence of thrombus reduces and redistributes the stresses and reduces the tension on the aortic wall [Wang et al. [2002]; Georgakarakos et al. [2009]].Therefore the idea behind the MFM is to promote the formation of organized thrombus inside the aneurysm sac, diminishing

the strain on the wall and consequently protecting the wall from rupture [Thubrikar et al., 2003].

**Endothelialization.** When the aneurysm is fully thrombosed, the blood flow is sheared along the inner layer of the MFM, which promotes the formation of an endothelial layer. With the endothelialization process, the stent and the disrupted vessel wall under the stent are no longer thrombogenic. The device is progressively covered by endothelial cells forming neointima on its endoluminal side. At the same time, the laminar flow entering the side branches prevents the fixation of the cells at their ostia [Lasheras [2007]; Lazaris et al. [2012]]. Histology reports from human explants have shown that implantation of the MFM induces a fibrous layer to appear between the smooth muscle cells and the endothelium. This fibrous layer serves as a biological barrier potentially capable of minimizing the volume of neointimal hyperplasia and thrombosis in the treated artery.

**Perfusion of aortic branches.** When an aneurysm crosses the ostium of a branch artery, the disturbance of the flow and the activity of vortices are increased (see figure 4.2B). With the MFM, the recirculation zones disappear and the flow is directed into the branch artery (see Figure 4.2D). The idea is that the presence of the side branch acts as a vacuum, shrinking the aneurysm and increasing the flow into the lateral branch [Sultan and Hynes [2012]; Polydorou et al. [2010]].

### 4.1.2 Technical features of MFM

The three-dimensional structure of the MFM is formed by the braiding together of several layers of cobalt-alloy interlocked wire (Phynox). In order to guarantee the target porosity of 60% to 70% (depending on its application), the number and size of wires and the number of layers vary for different device sizes.

For aortic aneurysmal pathologies, available MFM diameters are 25 mm, 28 mm, 30 mm, 32 mm, 35 mm, 40 mm, and 45 mm. Available component lengths are 80 mm, 100 mm, 120 mm, 150 mm, 180 mm, and 200 mm. The multilayer structure makes the device adaptable in length, depending on degree of compression and oversizing. The device Instructions for Use (IFU) detail recommended MFM sizes and compression rates relative to the target vessel diameter and stented length.

The delivery system is available with an outer diameter of 18 F or 20 F depending on the diameter and length of the MFM; the delivery system is 100 cm long and is compatible with 0.035-inch guidewires.

Device deployment occurs by means of a pullback release mechanism. After a stiff guidewire is placed up into the ascending aorta, the device is inserted into the abdominal aorta and then driven to the level of the proximal aneurysm neck (Figure 4.3A). At this point, the release of the device can start with a slow and gradual movement, in order to allow the stent to reach its nominal diameter, and to get a good proximal anchor (Figure 4.3B). Once the proximal sealing zone has been properly targeted, the release of the MFM is continued gradually, down

to the distal neck (Figure 4.3C). In the intermediate anephase of the release, the distal placing of the stent should be verified. The length of the stent can be modulated within certain limits, thus allowing for optimal use of the distal sealing area. Once the release has been completed, the cap is recaptured, under fluoroscopic control (Figure 4.3D-E). The maneuver has to be performed with utmost care, especially in cases involving extreme tortuosity of the aorta, in order to avoid stent displacement during the retraction.

### 4.1.3 Initial Clinical Data

**Early reports on single cases and small cohorts**

In 2008, Henry et al. reported the first case of MFM use, involving treatment of a renal artery aneurysm [Henry et al., 2008]. Intraoperative angiography showed a sharp reduction of the flow rate into the sac and patency of collateral vessels. Six months of follow-up angiography showed the complete thrombosis of the aneurysm with perfusion of the whole renal parenchyma maintained.
In 2011, Henry et al. [Henry et al., 2011] presented 10 cases of aortic aneurysm (6 TAAA and 4 abdominal aortic aneurysms AAA) treated with the device. During follow-up, complete thrombosis of the aneurysmal sac was documented in all cases, associated with a reduction of the aneurysmal diameter in some cases.
In 2012, Euringer et al. [Euringer et al., 2012] reported the case of a 45-year-old HIV-positive male with four saccular aneurysms - in both subclavian arteries and in the suprarenal and infrarenal abdominal aorta. The authors opted for use of the MFM rather than a branched endoprosthesis due to the involvement of the origin of the vertebral artery and of all side branches of the supradiaphragmatic aorta. Four MFM were used - two for the left subclavian artery, one for the right subclavian artery, and one for the abdominal aortic segment. Angiography after deployment of the devices showed a sharp reduction of the opacification speed after infusion of contrast, associated with the maintenance of sidebranch patency. Follow-up angiography at 18 months showed the complete thrombosis of the aneurysm sac in all treated arterial segments, except for the suprarenal segment where the sac appeared to be still minimally perfused. A slight reduction in the diameter of the aneurysmal sac in all segments was also shown.
In 2012, Benjelloun et al. [Benjelloun et al., 2012] presented a successful case of MFM treatment of multiple tubercular aneurysms in the thoracic and abdominal aorta in a 16-year-old female. Computed tomography (CT) angiography performed 18 months after the intervention showed clear regression of the disease at all levels.
Also in 2012, Tolva et al. [Tolva et al., 2012] reported the case of a 57-year-old female suffering from TAAA, with multiple severe comorbidities. The patient was treated by placement of three overlapping MFM. The 20-month follow-up CT showed an almost total thrombosis of the aneurysmal sac, associated with patency of all visceral vessels.
Further in 2012, Natrella et al. [Natrella et al., 2012] published the successful case of an

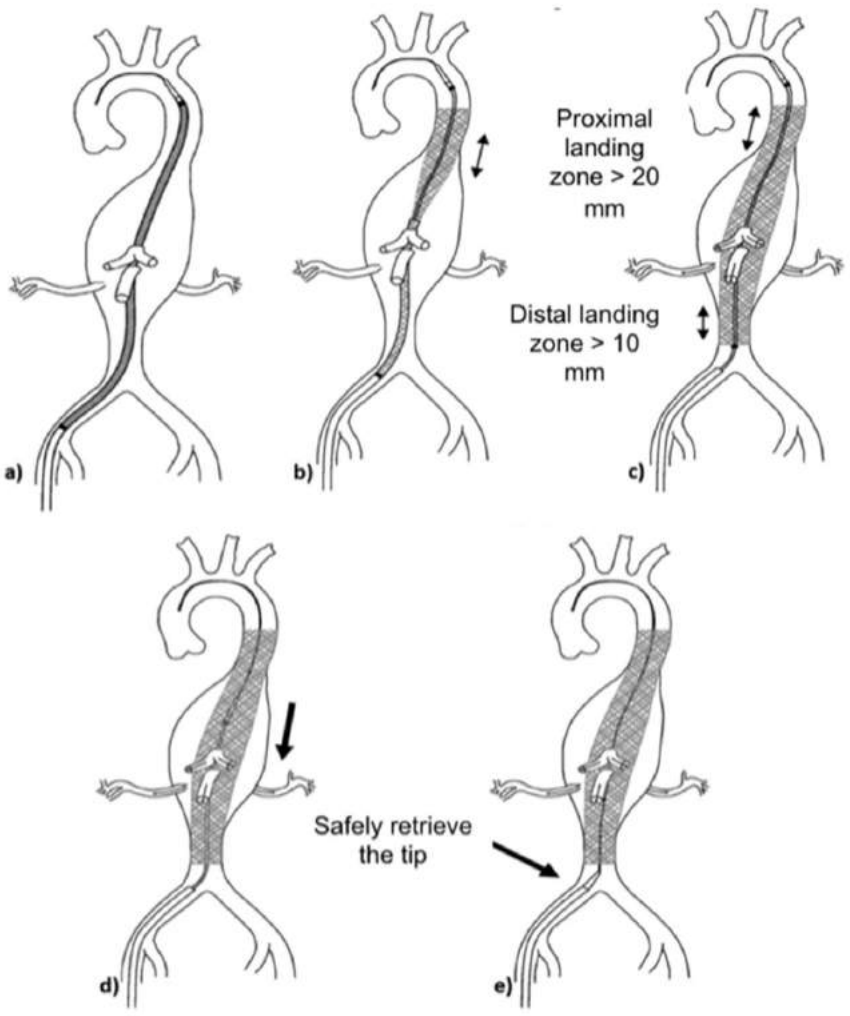


Figure 4.3: MFM deployment procedure.

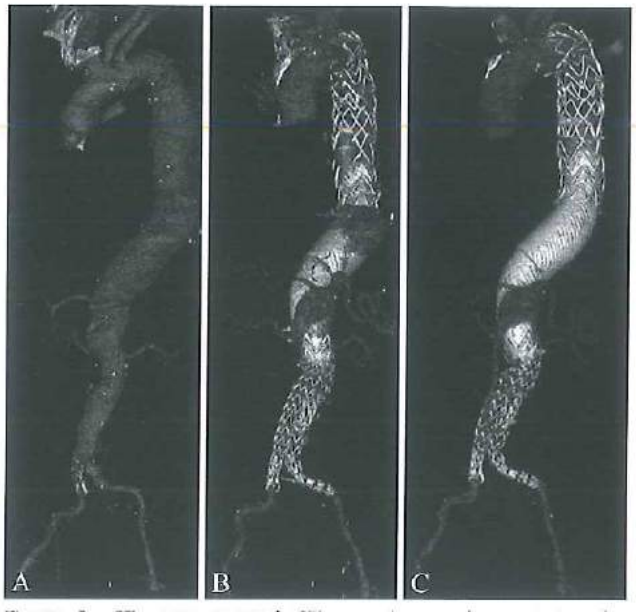


Figure 4.4: (A) pre-operative and (B) 1 month and (C) 6 months post-operative CT showing patency of branch vessels and thrombosis of the aneurysmal sac [Pane et al. 2013].

81-year-old male with multiple comorbidities and an expanding 63-mm juxtarenal AAA. The authors reported that upon implantation of a 100-mm MFM, the blood-flow velocity inside the aneurysm sac was immediately reduced. The aortic side branches that were covered by the MFM (celiac trunk, superior mesenteric artery, and renal arteries) all remained patent, and 12-month CT imaging showed progressive reduction in sac diameter and volume.
In 2013, Pane et al. [Pane et al., 2013] reported the case of a high-risk patient with type II TAAA treated, outside the IFU, with 2 thoracic endografts in combination with 2 MFM stents. As depicted in Figure 4.4, CT angiography at 1 and 6 months showed patency of visceral and renal arteries and progressive thrombosis of the aneurysm sac.
In 2014, Reijnen et al. [Reijnen and van Sterkenburg, 2014] reported on MFM treatment of a case of a Salmonella serotype enteritidis-induced rapidly expanding aortic pseudoaneurysm with a penetrating ulcer in a 78-year-old male. At 18 months, this patient was in good clinical conditions with normalized C-reactive protein levels, and imaging studies showed the aneurysm to be stable and mostly thrombosed, with adequate side-branch perfusion and no remaining sign of infection.
In 2012, Lazaris et al. [Lazaris et al., 2012] reported the case of a 78-year-old male patient who presented with a suprarenal abdominal aortic aneurysm rupture approximately 1 year after implantation of an MFM to treat a type IV TAAA. Although the stent permitted flow to all visceral arteries, the aneurysm sac was also filled by contrast. Although the patency of all

collateral vessels, blood flow was noticed inside the aneurysmal sac also at 6 months follow-up and aneurysm enlargement leaded to rupture. Unfortunately the patient died during emergency open surgical conversion. This case shows the importance of close surveillance during follow-up in order to detect and monitor the presence of persisting flow inside the aneurysm sac.
In 2014, Ferrero et al. [Ferrero et al., 2014] presented the case of 76-year-old woman with symptomatic type II TAAA. The patient was treated with the placement of 5 partially overlapping MFM and died on the fifth postoperative day, due to aortic arch rupture. The autopsy showed a 6 cm tear of the aortic arch in proximity of the descending tract. It was hypotized that the overlapping zone was too rigid to accommodate the degree of aortic arch angulation. Therefore, the trend of the stents was to lean on the outside of the physiological curvature of the aortic arch producing therefore a tear.

**Expanding study of the MFM**

The early case studies of MFM use were coincident with and have been followed by various other single-center and multicenter retrospective and prospective studies ([Hynes et al., 2016], [Vaislic et al., 2014], [Vaislic et al., 2016]). A systematic review of 15 of these studies covering 171 MFM patients (39 of them treated outside the IFU) found technical success of 77.2%, 1-year aneurysm-related survival of 78.7%, and all-cause survival of 53.7%, with no reported cases of spinal cord ischemia (SCI), renal insult, or stroke. Overall in the systematic review, in a total of 449 target branch vessels, the patency rate was 97.8%. For cases treated within the IFU, technical success was 98.5% and aneurysm-related survival was 93.3 % at 1 year and at 18 months [Hynes et al., 2016].
In 2013, Sultan and Hynes [Sultan and Hynes, 2013] reported outcomes for the first 55 patients enrolled in the global MFM registry, which was established to record both retrospective and prospective data for all aortic MFM implantations worldwide. The covered patient cohort included 31 TAAA (8 type I, 3 type II, 9 type III, and 11 type IV), 7 arch aneurysms, 3 infrarenal AAA, 8 suprarenal AAA, and 6 type B aortic dissections. Technical success was obtained in 98% of the cases, with a mean of 3.7±1.3 covered side-branch vessels. There were no adverse events in the first 30 days. During mean follow-up of 8.2±5.3 months, all covered side-branch vessels remained patent. The mean maximum aneurysm sac diameter remained stable, and the ratio of thrombus to total volume stayed almost constant, while the ratio of aneurysm flow volume to total volume fell from 21% to 12%. Sultan et al. have published subsequent reports on the global MFM registry in 2014 [Sultan et al., 2014b] and 2016 [Sultan et al., 2016]; as of the 2016 report, the registry contained data on 452 MFM patients.
In 2016, 3 years follow-up results from the STRATO trial were published [Vaislic et al., 2016]. The authors observed an overall growth of the total aneurysm volume from 232.9 ml to 363.5 ml (56 %) was detected after 3 years follow-up. Also concerning the percentage of thrombotic region, a slight increase in time was observed. Several re-interventions for endoleak were de-

tected during follow-up.
Also in 2016, the UK pilot study based on 14 patients showed on a mean follow-up of 22.8 months 4 aortic dislocations and 1 confirmed sac rupture Lowe et al. [2016].
Recently, Ibrahim et al. [Ibrahim et al., 2018] reported the outcomes of a multicenter retrospective study. 37 of 40 patients with TAAA or TAA where treated in an emergency basis. During follow-up they reported 4 cases of aneurysmal sac rupture and 10 patients underwent reintervention.
The MFM device is currently under clinical investigation for the treatment of chronic type B aortic dissection. The MFM Global Registry published a study based on Computational Fluids Dynamics (CFD) analysis for the use of MFM in the treatment of symptomatic chronic type B aortic dissection [Stefanov et al., 2017]. They concluded that the presence of the MFM modulates the pressure in the false lumen promoting the formation of thrombus and preserving at the same time patency of collateral vessels.

## 4.2 Our experience

As discussed in the previous section, several clinical studies regarding the MFM have been reported in the literature. However, to the best of our knowledge, little has been reported in the (bio)engineering about such a device; in fact, only few illustrative examples of patient specific numerical simulations with MFM stents can be found in literature. Sisto et al. [Sisto et al., 2015] performed numerical simulations to investigate blood flow differences between no stent, monolayer stent and MFM configurations in the treatment of cerebral saccular aneurysms. A computational fluid dynamic study to evaluate velocity profiles and WSS in three cases of simplified thoracic aortic aneurysm models (no stent, single monolayer stent, and two overlapped monolayer stents) has been presented also by Zhang et al. [Zhang et al., 2015]. The results of this study showed that the overlapping stenting procedure induces a reduction of blood flow velocity within the aneurysm sac, which may create a favorable hemodynamic environment.
In addition, most of the clinical research groups which published MFM follow-up results, based their follow-up measurements on the manual evaluation of the maximum diameter [Balderi et al., 2013] or evaluated complete shrinkage of the sac simply by visual inspection [Henry et al., 2008, Tolva et al., 2012]. Debing et al. [Debing et al., 2014] and Sultan and Hynes [Sultan and Hynes, 2013] measured the aneurysm volume by means of dedicated commercial softwares. Also [Vaislic et al., 2014] reported follow-up measurements based on total volume and changes in the ratios of thrombus and aneurysms sac, even though no information about the employed tools and the followed methodology are reported.
Given such considerations, in this work, following the explicit needs of the surgeons, we aim at proposing a framework of medical image analysis in order to reconstruct the aneurysm geometry and quantify its changes in time. Then, in order to test the introduced methodology,

we will present the outcomes of 4 patients suffering from TAAA with 2 years follow-up after MFM insertion. Complete evaluations about the MFM behavior and the modifications induced in time in the aneurysm sac are showed.

## 4.3 Materials and Methods

Through bioimaging techniques and geometrical analysis, starting from contrast-enhanced CTA images, we define a framework for the analysis of the geometric and morphological changes of the aneurysmatic lumen and thrombus induced by the implantation of the MFM device.

### 4.3.1 Patients' clinical history

The dataset is composed by CTA images of four patients undergoing endovascular treatment at Ospedale Policlinico San Martino, Genoa. All the patients have aneurysms in the thoraco-abdominal aorta including the portion of the vessels where the origin of the visceral and renal arteries is located. All patients were asymptomatic and were considered at too high risk for open surgery treatment and anatomically unsuitable for Fenestrated Endovascular Aortic Repair (FEVAR) or other endovascular treatments (chimney or snorkel TEVAR).
The surgical procedure was carried out under general anaesthesia. Cerebrospinal fluid drainage positioning for II and III type TAA. The total number of vessels that originated from the aneurysmal sac or from the sealing zone of the MFM was 13 for the whole study. Postoperative medical therapy protocol consisted in lifelong dual anti-platelet therapy (acetilsalicilic acid 100 mg/dye and clopidogrel 75 mg/dye).
For each patient one pre-operative CTA (called Pre in the following) and three post-operative CTAs in the firsts two years of follow-up, at established times, were collected: immediately after intervention (Post), after 1 year (1y) and after 2 years (2y). After 2 years, Patient 2 required re-intervention due to an excessive growth of the aneurysm sac resulting in the implantation of a second MFM. Therefore, for this patient, an additional CTA performed after the last intervention (Post2) is considered. No reinterventions were needed during follow-up for the other patients. Patients' characteristics, information about the stenting procedures, and available CTA scans are reported in Table 4.1.
The CTA scans have been performed using different CTA facilities and in different hospitals. Concerning image resolution, the pixel size varies from 0.7636 x 0.736 mm (worst case) to 0.63 x 0.63 mm (best case) while the slice thickness ranges from 5 mm (worst case) to 0.5 mm (best case).
The study was developed in accordance with the local institutional guidelines, and the need for patient informed consent was waived because of the retrospective nature of the analysis and the use of anonymized data.

| | Patient 1 | Patient 2 | Patient 3 | Patient 4 |
|---|---|---|---|---|
| Age | 73 | 65 | 64 | 85 |
| Sex | F | F | F | F |
| Previous aortic surgeries | no | yes | no | yes |
| Number of MFMs | 2 | 1 | 1 | 1 |
| Stent Diameter | 40 / 40 | 30 | 35 | 25 |
| Stent Lengths | 150 / 200 | 150 | 150 | 150 |
| Additional prostheses | no | no | yes | no |
| Re-intervention | no | yes | no | no |
| Available CTAs | Pre, Post, 1y, 2y | Pre, Post, 1y, 2y, Post2 | Pre, Post, 1y, 2y | Pre, Post, 1y, 2y |

Table 4.1: Characteristics of the enrolled patients.

### 4.3.2 In-vivo imaging framework

An overview of the proposed framework of image analysis is given in Figure 4.5. Our approach first segments the aneurysmatic zones and the implanted devices from the CTA images. Then, for each patient, a rigid registration between pre-operative and post-operative surfaces is computed. Afterwards, the centerlines are extracted from the 3D mesh surfaces. Finally, clinically relevant geometric parameters are estimated.

#### Segmentation procedure

Different segmentation processes are employed in order to extract the lumen, the MFM and the aneurysm region. A semi-automatic gradient-based level set method with the colliding front initialization [Antiga et al., 2008], available in the VMTK library, is used to extract the lumen (more details about the segmentation procedure are given in Section 2.7.4).
Considering the stent region, a threshold method is employed to initialize the segmentation process. A value of 1000 HU is chosen for the lower threshold and no value is given for the upper one. This choice is justified by the higher x-ray absorption of the metal stent in comparison to the surrounding tissues.
Subsequently, independently of the adopted initialization procedure, the zero level set surfaces are extracted using the Marching Cubes algorithm. This algorithm returns an initial polygonal surface that, however, is not directly suitable for geometric analysis due to an insufficient triangle quality. Hence, meshes are improved using smoothing filters [Taubin, 1995] and remeshing operations.
Due to low contrast in the thrombotic region compared to adjacent anatomical structures, a semi-manual technique is chosen to discern the aneurysm external wall. In particular, as extensively illustrated in Section 2.7.4, the manual contour of a reduced number of slices is extracted [Fetzer et al., 2014]; then a 3D surface interpolation using radial basis functions is performed.

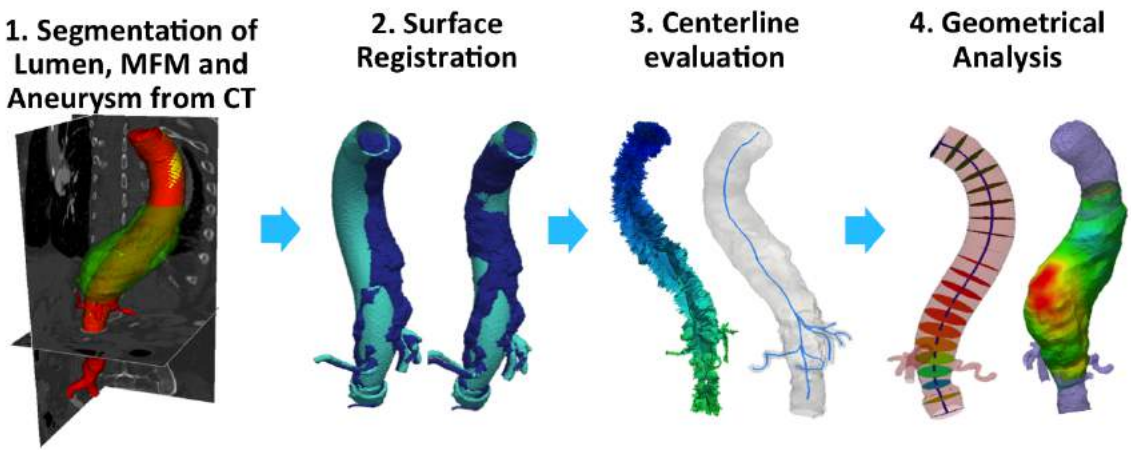


Figure 4.5: Workflow of the proposed framework: (1) segmentation procedure to extract the lumen, the MFM stent and the aneurysm wall; (2) surface registration of the post-operative surfaces to the pre-operative reference one; (3) centerline evaluation and (4) geometrical analysis on both lumen and total aneurysm surface.

### Surface registration

The main problem in comparing two surfaces deriving from different CT images is that the position of the patient and, as a consequence, the aorta location, differs from one another. Therefore, the Iterative Closest Point algorithm [Bels and McKay, 1992] is used to register each follow-up lumen surface to the pre-operative reference one. The algorithm consists in associating each vertex in one surface with the closest point on the other surface using the neighbour criteria and iteratively applying the transformation that minimizes the distance between paired points. The output is a rigid transformation matrix (roto-translation) that is then applied to both the MFM and the aneurysm surface.

### Centerline evaluation

Centerline of the lumen was computed following the method implemented in VMTK and illustrated in detail in Section 7.3.1.
Since we want to perform geometrical measurements on the aortic artery, is necessary to obtain the lumen surface without side branches. For this reason, following the method implemented in VMTK [Antiga and Steinman, 2004], the centerline is divided in groups relative to the bifurcation. At this point, the bifurcating segment is splitted into its branches and the principal lumen surface is extracted.

### Geometrical analysis

For each patient under study, we aim at verifying the perfusion of the side branches and the changes occurred in time to the patient's principal vessel centerline. In addition, the presence or absence of residual blood flow and the growth and the morphological changes of the aneurysm sac are investigated. To this end, geometric measurements on sections and volumetric indices are evaluated.
The collateral perfusion can be easily evaluated by geometrical visual inspection of the lumen surfaces. After that, for all the configurations, main vessel centerlines are extracted in order to visually investigate whether the MFM insertion causes changes to the aorta physiological curvature. In order to analyze geometrical changes in blood and aneurysm, we identify the total aneurysm region (TAR) comprising both the the lumen region (LR) and intraluminal thrombus (ILT). The lumen region is further decomposed in the residual blood flow (RF), i.e. the blood that flows outside the implanted stent and the MFM blood flow (MFMF), i.e. the blood that flows inside the stent. In Figure 4.6 the different regions are highlighted.

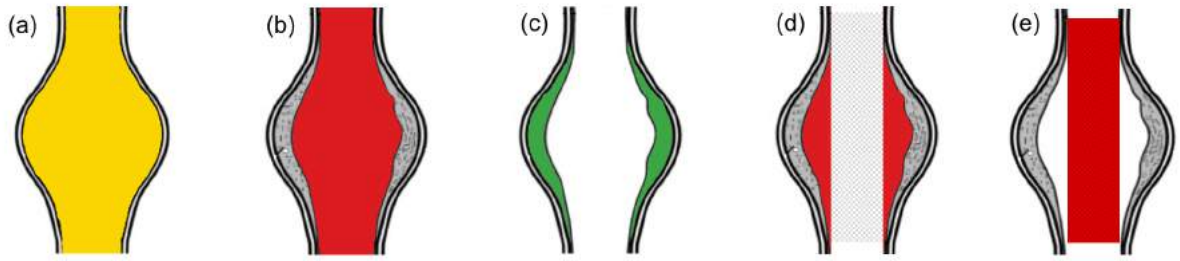


Figure 4.6: The regions in which volumetric indices are computed, are highlighted: (1) total aneurysm region (TAR); (b) the lumen region (LR); (c) the intraluminal thrombus (ILT); (d) the residual blood flow (RF); (e) the MFM blood flow (MFMF).

Firstly, we analyze the principal branch generating sections, at given distances, perpendicular to the centerline for both the vessel lumen and aneurysm. We remark that, thanks to the surface registration step, the sections are extracted at the same positions in all the pre-operative and post-operative surfaces allowing a direct comparison between different time instants. Moreover, in order have good correspondence between the sections obtained at different times, the pre-operative centerline has been adopted for all the lumen surfaces. The same centerline, suitably tailored on the aneurysm length, is used also for the aneurysm wall surface. For each section we evaluate area, maximum and minimum diameter, and a shape index $\overline{SI}$ computed as the ratio between the maximum and the minimum diameter. $\overline{SI}$ ranges from 0 to 1 where 1 signifies a completely circular shape [Piccinelli et al., 2012]. These measurements are taken both for the lumen and for the total aneurysm sac as illustrated in

Figure 4.7.

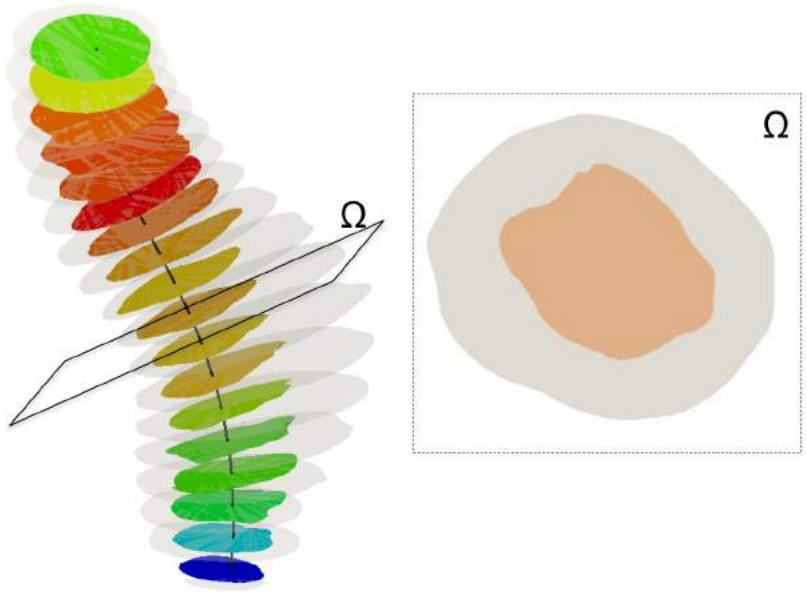


Figure 4.7: For both the aneurysm and the lumen, sections are generated perpendicular to the centerline and, for each section, maximum and minimum diameter, area and shape index are computed. In the section view (Ω), the lumen area is depicted in orange and the aneurysm area is in grey.

Secondly, we evaluate some volumetric indices. First of all, we consider the total aneurysm volume ($v_{TAR}$) and the percentage of aneurysm growth in comparison with the pre-operative configuration ($v_{TAR}\%$). Starting from the lumen volume ($v_{LR}$) computation, the residual flow volume ($v_{RF}$) and the percentage of lumen growth in comparison with the pre-operative configuration ($v_{LR}\%$) are also estimated. Percentage ratio formula are presented in Eq. 4.1.

$$v_{TAR}\%(t) = \frac{v_{TAR}(t) - v_{TAR}(0)}{v_{TAR}(0)} * 100 \qquad v_{LR}\%(t) = \frac{v_{LR}(t) - v_{LR}(0)}{v_{LR}(0)} * 100 \tag{4.1}$$

where $v_{TAR}$ is the total aneurysm volume in a given time instant, $v_LR$ is the lumen volume in a given time instant, $t = 0$ is the pre-operative phase and $t$ is the current evaluated time (Post, 1y,...). In the end, we introduce the ratio of thrombotic region (RTR%, see Eq. 4.2), which is a 3D size index related to the percentage of intraluminal thrombus in the aneurysm sac.

$$RTR\%(t) = \left(1 - \frac{v_{RF}(t)}{v_{RF}(t) + v_{ILT}(t)}\right) * 100 \tag{4.2}$$

where $v_{ILT}$ is the volume of thrombus. A value of 100% indicates a complete thrombization

of the aneurysm.

### 4.3.3 Statistical Analysis

Categorical variables are expressed as absolute frequencies or percentages whereas continuous variables as mean values.

### 4.3.4 Intra-observer and inter-observer reproducibility

Intra-observer and inter-observer reproducibility is performed only for the measurement of the total volume of the aneurysm because the process of semi-manual segmentation of the aneurysm external wall is not trivial and it may lead to differences between the measurements obtained by different operators. Therefore, to validate the obtained results, two independent skilled observers performed semi-manual segmentation of CTAs images (extraction of contours on a reduced number of slices), and one of them conducted it twice, allowing for inter-observer and intra-observer variability analysis. The total volume of the aneurysm was then automatically computed and compared. Data were analyzed with the Statistical Package for Social Sciences, Version 24.0 (SPSS; IBM Corporation, Somers, NY) using the intraclass correlation coefficient (ICC). Results were presented with the 95% confidence interval CI.
Conversely, the segmentation of lumen and MFM surfaces is performed by a semi-automatic segmentation method implemented in the VMTK software, which has been already validated [Antiga et al., 2008] and used for vascular research. Given the minimum interaction of the user in such a process, intra-observer and inter-observer reproducibility is not computed for the measurement of the luminal volume and the stent surfaces.

## 4.4 Geometric analysis results

Technical success of the intervention was achieved in all patients, without paraplegia or perioperative visceral or renal insult. In Figure 4.8 the geometric 3D reconstructions of the four patients are reported. We take the configuration Post as an example. Red color refers to the lumen, yellow to the MFM and green to the ILT. As shown from the picture, for all patients side branches remain perfused. Considering the modifications occurred to the centerlines, we can observe that only for Patient 2 and Patient 4 centerline effectively changes in the MFM apposition zone.
In Figure 4.9 the results obtained from the analysis of cross-sections are presented. Considering the lumen section area, for Patient 1 we observe that, from Pre to Post, lumen area seems to be stable whereas after 2 years it increased considerably with a final peak value in the central zone of the aneurysm that changes from 1369.7 $mm^2$ in the Pre configuration to 2073.3 $mm^2$ in the 2y configuration with a growth of the 51.36 %. As concern the lumen $\overline{SI}$, the insertion of the MFM has caused an enhancement of the sections circularity. The TAR section area and

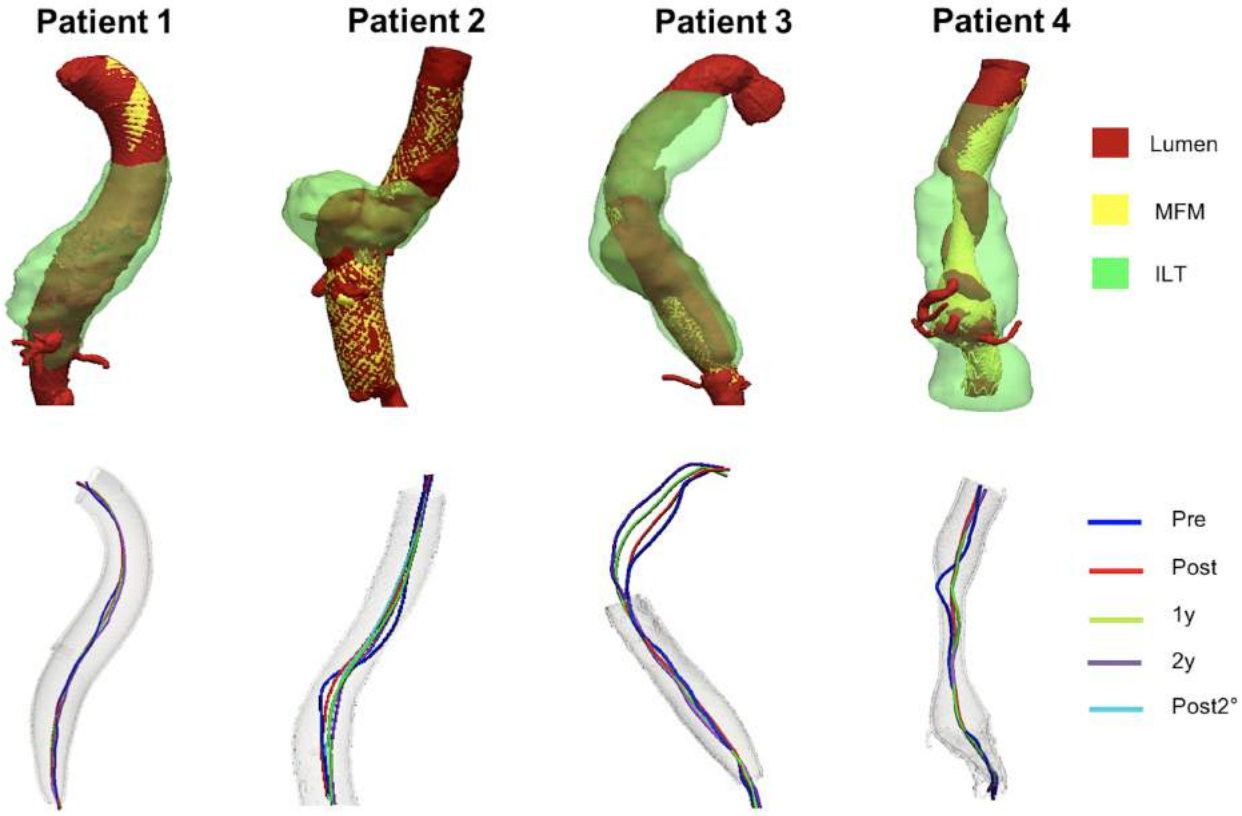


Figure 4.8: Segmentation and centerline calculation: 3D reconstructions concerning the configuration Post are depicted (top); centerline changes at different times are reported (bottom).

the TAR maximum diameter show a similar behavior: they remain stable until 2 years when a sudden growth is detected. For Patient 2 the lumen section area has gradually increased in time until 2 years and the lumen has become more irregular. Indeed, the mean value of the sections $\overline{SI}$ varies from 0.93 (Pre) to 0.85 (2y). Only with the second surgery we observed a reduction of the lumen section area. Contextually, a progressive growth of the TAR that stopped only with the re-intervention is observed. The TAR maximum diameter ranges from 59.6 $mm$ in the pre-operative phase (peak value) to 82.2 $mm$ at 2 years follow-up. For the Patient 3 after 1 year, the lumen section areas have decreased in the proximal region but increased in the distal one and the lumen sections have become more regular ($\overline{SI}$ from 0.78 to 0.88 ). Important growth of the aneurysmal sac is observed only after 2 years: the TAR maximum diameter increased from 63.2 $mm$ to 73.4 $mm$ and lumen maximum diameter has grown by 15 % from 51.2 $mm$ to 58.9 $mm$. Trend reversal is observed for Patient 4: both the lumen section areas and the TRA section areas decreased from Pre to 2 years. Considering the peak value of the lumen section areas, it decreased from 795 $mm^2$ to 730 $mm^2$ whereas a

reduction from 1918.5 $mm^2$ to 1776.1 $mm^2$ in the peak value is observed for the TAR section area. Immediately after the intervention, the lumen $\overline{SI}$ has become more regular followed by stationary phase.
For more details, results for each case are presented in Tables 4.3 and 4.4.

In Table 4.2 results of the volumetric indices are reported. Considering the aneurysm sac, for the Patient 1 the volume of the TAR significantly increased after the intervention and again after 2 years whereas remained stable between the Post and 1y configuration. In the firsts two years, for the second patient, a nearly linear growth is observed which stopped only after the second intervention. After two years, Patient 3 has a little growth of the TAR volume (26.5 %) whereas for Patient 4 a reduction from $2.09 \cdot 10^5 mm^3$ to $1.89 \cdot 10^5 mm^3$ is detected. As concerns lumen growth, for Patient 1 and Patient 2, a gradual increase in time is observed. But, after the second surgery, the residual flow decreased from $7.7 \cdot 10^4 mm^3$ to $6.6 \cdot 10^4 mm^3$ (-14.28 %). Lumen volume of Patient 3 decreased from Post to 1y, after that a moderate growth is detected. Only for Patient 4, a gradual and continuous decrease of residual flow volume from $2.0 \cdot 10^4 mm^3$ to $1.3 \cdot 10^4 mm^3$ is observed estimating a percentage decrease of 32.5 % in two years. After 1 year, RTR% index of Patient 1 has decreased from 75 % to 63 %, followed by an increase until 72% after 2 years. Therefore, for this patient no clear evidence of thrombization process is detected. For Patient 2 and Patient 4, RTR% index does not change significantly in time, but the latter is fixed at a higher value (90 %). Considering the obtained results, for Patient 2 the ratio of thrombotic zone does not change in time because the aneurysm growth is closely related to the lumen growth. On the other hand, for Patient 4, RTR% ratio remains stable because the shrinkage of the lumen region causes a total aneurysm volume reduction. In Patient 3 an important thrombization process is observed in the first year (RTR% from 48 % to 69 %) followed by a stabilization.

For a better understanding of the aneurysm zones location where the maximum volumetric changes occurred, we use a module of the VMTK library which computes the pointwise minimum signed distance between the pre-operative aneurysm surface and the 24-month configuration. In Figure 4.10 the visualization of three-dimensional geometries showing the contour plot of the relative distance is provided: colors change, from blue (volume maximum decrease) to red (volume maximum increase), according to the relative distance between the two surfaces.

### 4.4.1 Intraobserver and interobserver reproducibility

Intraobserver and interobserver reproducibility of aneurysm volume values were calculated by ICC. Intraobserver and interobserver ICC resulted 0.99 (95% CI 0.99 to 1.00) and 0.98 (95% CI 0.97 to 0.99) respectively, indicating excellent agreement for $V_{TAR}$.

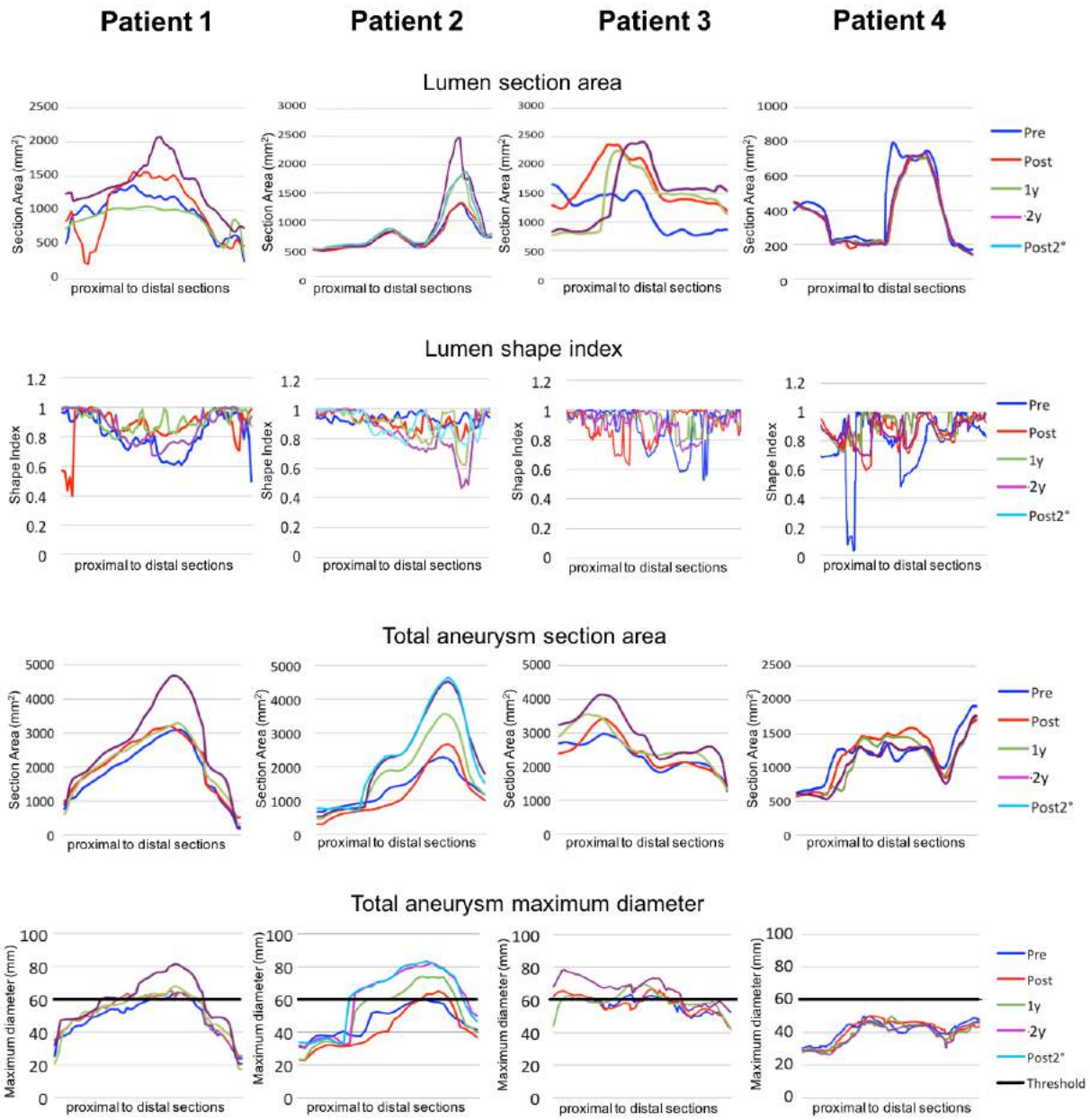


Figure 4.9: Results of geometric indices on sections are presented. Lumen section area, lumen $\overline{SI}$, total aneurysm section area and total aneurysm maximum diameter, for the four patients in all time configurations are considered. For the aneurysm maximum diameter, a constant value set at 60 mm is reported indicating the threshold diameter for elective aneurysm repair.

| | | $v_{TAR}$ $(10^5 mm^3)$ | $v_{TAR}$% | $v_{RF}$ $(10^4 mm^3)$ | $v_{LR}$% | RTR% |
|---|---|---|---|---|---|---|
| Patient 1 | *Pre* | 2.8 | | | | |
| | *Post* | 3.9 | 38 % | 5.4 | 17 % | 75 % |
| | *1y* | 3.8 | 37 % | 8.4 | 29.5 % | 63 % |
| | *2y* | 5.2 | 79 % | 9.6 | 38 % | 72 % |
| Patient 2 | *Pre* | 1.1 | | | | |
| | *Post* | 1.1 | 11 % | 3.8 | -12 % | 61 % |
| | *1y* | 1.6 | 47 % | 5.5 | 24 % | 58 % |
| | *2y* | 2.1 | 94 % | 7.7 | 53 % | 58 % |
| | *Post2°* | 2.2 | 106 % | 6.6 | 39 % | 66 % |
| Patient 3 | *Pre* | 3.8 | | | | |
| | *Post* | 3.9 | 3.2 % | 14 | 39.8 % | 48 % |
| | *1y* | 4.3 | 13.5 % | 9.5 | 17 % | 69 % |
| | *2y* | 4.8 | 26.5 % | 10 | 24 % | 70 % |
| Patient 4 | *Pre* | 2.09 | | | | |
| | *Post* | 2.1 | 0.09 % | 2.0 | -10.8 % | 87 % |
| | *1y* | 1.95 | -6.7 % | 1.85 | -11.7 % | 88 % |
| | *2y* | 1.89 | -9.5 % | 1.35 | -12.9 % | 90 % |

Table 4.2: For all patients, volumetric indices in the pre-operative and postoperative configurations are calculated.

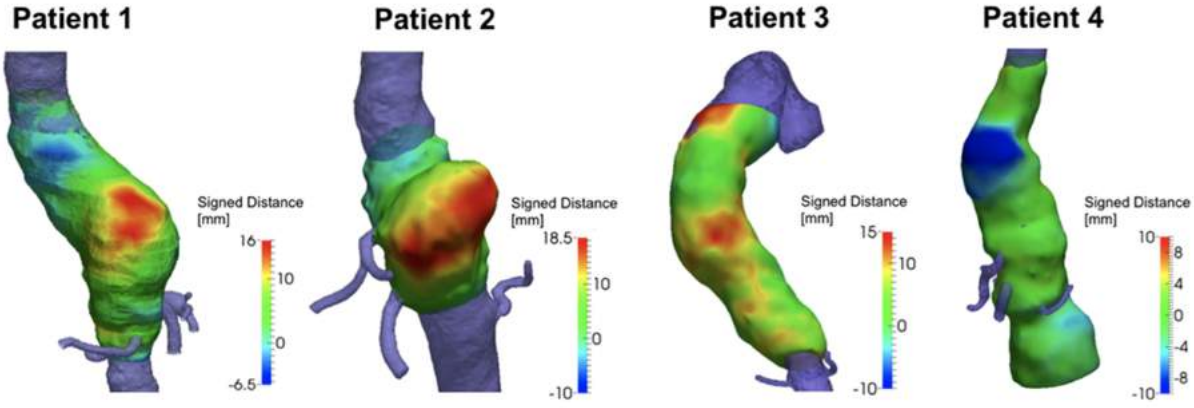


Figure 4.10: For the four patients, a contour plot of the signed pointwise minimum distance between the pre-operative aneurysm surface and the 2-year aneurysm surface is depicted. Color scale range from blue (decreasing of the sac at 2 years) to red (increasing). Lumen surfaces are purple-colored.

## 4.5 Discussion

TAAA are challenging to treat. Endovascular treatment has become established as a valuable alternative to open surgery repair for those patients with an high risk for perioperative mor-

tality and morbidity. More recently, a new concept of stent, the MFM, has been introduced as minimally invasive endovascular solution for the repair of thoracoabdominal aneurysms. The MFM device is an uncovered, self-expanding alloy stent used in the treatment of complex cases of aortic aneurysms. In particular, when the aneurysm involves collateral branches, traditional covered stent-grafts cannot be adopted leading to the occlusion of collateral arteries [Kolvenbach, 2017]. The adoption of multilayer stents may therefore overcome such anatomic limitations [Henry et al., 2008]. Due to the novelty of this device, an accurate post-operative geometrical analysis may represent a powerful tool to check the evolution of the pathology step by step and to study both the short and the long term performances of the device. Hence, aim of the present study was to conceive a complete pipeline of analysis: starting from the segmentation process, the lumen, the total aneurysm and the MFM surface have been extracted and analyzed. Measurements at different sections and morphological changes of volume are evaluated. We have considered a single center experience with 4 patients involved and follow-up results at 2 years in order to test the introduced framework.

One of the main features of the MFM concerns the patency of collateral branches: the obtained results, i.e., 0 % of collateral branches occlusion, are in agreement with other cases in literature [Debing et al., 2014, Henry et al., 2013].

One of the main cons of this treatment is that, unlike conventional covered stentgrafts, MFM device does not exclude blood flow from the aneurysm sac, which could mean that patients are not immediately protected from aneurysm rupture [Debing et al., 2014]. In particular, our results showed an overall growth of the patients' TAR at 2 years which are similar to those of the 3-years STRATO trial [Vaislic et al., 2016].

Focusing on a single case, Patient 2 underwent a second implantation to avoid a potential rupture due to an excessive growth. For this patient a positive future reduction of the aneurysm sac is predicted brought by the addition of a second MFM. After the second surgery, when a second MFM has been superimposed to the first, $v_{RF}$ has indeed decreased. We supposed that this behavior could be related to the different porosity when only one or two superimposed stents are implanted. This behavior suggests the need for in-vitro and in-silico studies to evaluate the relationship between the tuning of the porosity of the MFM and the presence and behavior of the flow inside the aneurysmal sac in order to draw guidelines for future interventions.

However, even though these patients were treated with the MFM device on a compassionate basis, the overall survival rate at 2 years is 100 %. Therefore, it can be argued that the increasing in time of the aneurysm sac do not inevitably portend rupture. These results could also be seen as an encouraging data toward the routine use of the MFM device in complicate, high-risk cases unsuitable for open repair or traditional endovascular treatment. Moreover, the recent introduction of new bifurcated MFM device could allow to treat also aneurysms involving aortic bifurcation [Costache et al., 2016].

## 4.6 Limitations

The main limitation of the study regards the use of a semi-manual method to segment the external wall of the aneurysm which could be affected by inter-operator errors. However, at the state of the art, it seems the only feasible option especially when no calcified vessels are involved. A second limitation regards the absence of a standard protocol for CTA acquisitions due to the retrospective design of the study. Another limitation is the small number of enrolled patients.

## 4.7 Conclusions

To conclude, we have defined a new pipeline for the geometric analysis of aneurysms, which has been applied to patients treated with the MFM device and related follow-up images. The dataset is composed of four patients affected by TAAA of different geometrical shape, which are also characterized by an extremely different behavior in terms of MFM implantation response. Therefore, our framework has been proved and is able to provide multiple and complete results for any aneurysm shape and for any morphological change in time. For the first time, a geometrical framework of analysis was introduced to be employed for the extraction of quantitative informations about follow-up morphological changes of the vessels. Moreover, based on our findings, an accurate quantification of aneurysm progression over time after MFM implantation resulted of great importance. An analysis with a larger and more homogeneous group is mandatory in order to give reliable results about the use and feasibility of the MFM stent in TAAA interventions.

| | | $d_{max}$ [mm] | | Area [mm$^2$] | | SI [] |
|---|---|---|---|---|---|---|
| | | Mean ± std dev | max | Mean ± std dev | max | mean |
| Patient 1 | Pre | 39.8±6.8 | 48 | 1022.9±275 | 1369.7 | 0.82 |
| | 1 month | 40±8.1 | 50.1 | 1131.9±388 | 1569.9 | 0.87 |
| | 12 months | 43.4±7.3 | 54.4 | 1297.3±331 | 1645.3 | 0.91 |
| | 24 months | 45.8±8.4 | 58.9 | 1394.2±380 | 2073.3 | 0.87 |
| Patient 2 | Pre | 31.1±5.3 | 44.6 | 709.5±235 | 1297.2 | 0.93 |
| | 1 month | 31.7±5.7 | 45.5 | 717.5±245 | 1311.8 | 0.92 |
| | 12 months | 32.4±7.6 | 55.7 | 808±365 | 1781.9 | 0.91 |
| | 24 months | 35.5±12 | 67.6 | 903±538 | 2484.4 | 0.85 |
| | 27 months[a] | 33.8±8.3 | 54.3 | 849±396 | 1879.9 | 0.89 |
| Patient 3 | Pre | 42.8±5.9 | 51.2 | 1150.7±342 | 1660 | 0.78 |
| | 1 month | 49.1±5 | 58.2 | 1647.3±396 | 2360 | 0.92 |
| | 12 months | 43.8±7.7 | 54.6 | 1398±467 | 2258 | 0.9 |
| | 24 months | 44.6±8.3 | 58.9 | 1499.3±509 | 2408.8 | 0.88 |
| Patient 4 | Pre | 24.5±7.2 | 37.5 | 413±210 | 795.4 | 0.78 |
| | 1 month | 22.7±5.8 | 33.5 | 366±185 | 712.6 | 0.9 |
| | 12 months | 22.7±5.8 | 34 | 366±182 | 712.6 | 0.9 |
| | 24 months | 22.9±6.1 | 35 | 370±189 | 730 | 0.9 |

Table 4.3: Results of the geometric indices performed on blood flow sections.
[a] CT performed after the second intervention.

| | | $d_{max}$ [mm] | | Area [mm$^2$] | | SI [] |
|---|---|---|---|---|---|---|
| | | Mean ± std dev | max | Mean ± std dev | max | mean |
| Patient 1 | Pre | 49.1±11 | 64.3 | 1937.15±817 | 3104 | 0.96 |
| | 1 month | 51.9±11.3 | 65.1 | 2141.7±823 | 3207.5 | 0.92 |
| | 12 months | 52.3±12.5 | 68 | 2170.6±821 | 3304.4 | 0.92 |
| | 24 months | 58.8±15.2 | 81.5 | 2738.1±1217 | 4689.3 | 0.95 |
| Patient 2 | Pre | 46.7±9.1 | 59.6 | 1375.6±516 | 2277.8 | 0.84 |
| | 1 month | 42.7±13.1 | 65.2 | 1243.4±740 | 2665.3 | 0.88 |
| | 12 months | 52.4±16.8 | 74 | 1806.2±996 | 3564.8 | 0.91 |
| | 24 months | 60.4±19 | 82.2 | 2291.6±1335 | 4534.3 | 0.72 |
| | 27 months[a] | 61.1±18.9 | 83.2 | 2335.7±1328.7 | 4660.3 | 0.85 |
| Patient 3 | Pre | 55.51±5.6 | 63.2 | 2333.7±419 | 2987.3 | 0.95 |
| | 1 month | 56.2±6 | 66.5 | 3422.1±532 | 3437.3 | 0.96 |
| | 12 months | 59.8±6.6 | 69.8 | 2655.6±560 | 3559 | 0.95 |
| | 24 months | 62.7±7 | 73.4 | 2997±687 | 4148.2 | 0.95 |
| Patient 4 | Pre | 41.8±5.6 | 50 | 1181±304 | 1918.5 | 0.78 |
| | 1 month | 41.3±6.8 | 50.1 | 1202±356 | 1714 | 0.9 |
| | 12 months | 39.7±6.4 | 49.8 | 1113±355 | 1767.5 | 0.9 |
| | 24 months | 38.8±6.5 | 47.4 | 1068±322 | 1776.1 | 0.9 |

Table 4.4: Changes in sections area and diameter for the aneurysm surface.
[a] CT performed after the second intervention.

# Chapter 5

# Assessment of geometrical remodeling of the aortic arch after hybrid treatment

In this chapter we will report a study regarding the geometric remodeling of the ascending aorta, aortic arch and thoracic aorta in patients who underwent hybrid repair of the aortic arch including debranching and stent graft implantation.[3]

## 5.1 Motivation and objectives

Although recent guidelines recommend the endovascular approach as the treatment of choice for patients affected by thoracic aortic diseases [Riambau et al., 2017], the anatomy of the thoracic aorta may affect the feasibility of this approach in many settings. In particular, the need to obtain an adequate proximal landing zone of the healthy aorta is crucial to avoid proximal type I endoleak or endograft migration [Nation and Wang, 2015]. Indeed, proximal landing zones with an at least 20 mm-long, healthy and relatively straight neck are needed for thoracic endograft placement [Fanelli and Dake, 2009].
On the contrary, in patients with short and highly angulated landing zones, a hybrid arch treatment performed in Ishimaru's zones 0, 1 or 2 [Mitchell et al., 2002] has been introduced as a feasible technique for revascularization of the supra aortic vessels to obtain an adequate proximal landing zone for TEVAR.
Unfortunately, the aortic arch is a critical zone for the device delivery, and its intrinsic shape

[3]This chapter is based on:

- Assessment of geometrical remodeling of the aortic arch after hybrid treatment. Spinella G, Finotello A, Conti M, Faggiano E, Gazzola V, Auricchio F, Chakfé N, Palombo D, and Pane B. Assessment of geometrical remodeling of the aortic arch after hybrid treatment. European Journal of Cardio-Thoracic Surgery; in press.

plays a crucial role in the rate of acute failure of thoracic endografts [Findeiss and Cody, 2011]. Indeed, the deployment of an endograft inside the flexible aortic tissue might lead to hard-to-predict morphological variations of the vessel shape that can be correlated with short-, mid- and long-term complications. Identifying the changes in aortic arch morphology between pre- and post-operative configuration could therefore be important in order to understand the causes of such complications and to predict procedure-related adverse events.
To date, other investigators have already focused on the role of anatomical factors in positioning outcomes [Boufi et al., 2017] or have evaluated the changes in aortic arch curvature following TEVAR [Mestres et al., 2017]. However, little is known about the geometric changes that occur at landing zones after aortic arch hybrid treatment and how these could be related to possible complications. On the basis of these considerations, the aim of our study was to measure the morphological remodeling of the thoracic aorta in patients who undergo aortic arch hybrid treatment. Aortic remodeling was measured by quantitative analysis of the aortic geometry before and after hybrid arch repair.

## 5.2 Materials and Methods

The research protocol was submitted to the local institutional medical ethics committee; the need for informed consent from the patients was waived because of the retrospective nature of the analysis and the use of anonymous data.

### 5.2.1 Patient selection

A single-center, retrospective study was conducted on all consecutive patients that underwent aortic arch hybrid treatment between January 2012 and December 2016.
Only patients treated in zones 0, 1, or 2 according to the Ishimaru classification [4] were included in the study, while patients who did not undergo supraaortic vessels revascularization or those with previous open repair of ascending aorta were excluded; type-B aortic dissections (n=3) were excluded as well due to the great remodeling of the true lumen after TEVAR.
On the basis of such criteria, a total of 22 cases were included: mean age was 70.4 years (range 31-89 years), 15 subjects were male. Nine patients presented thoracic aortic aneurysms, 9 had PAU complicated by pseudoaneurysm, and 4 had aortic IMH. Proximal landing zones 0 (Z0), 1 (Z1) and 2 (Z2) were involved in 10, 3, and 9 patients, respectively. Patients' characteristics are listed in Table 1. All procedures were performed under general anesthesia: 9 were single-stage and 13 were two-staged. In the two-stage repair, the first stage consisted of supraaortic vessels revascularization, the second stage was the endovascular endograft deployment. Median time interval between the two procedures was 21 days; median time interval between pre-operative and 1-month CTA and between pre-operative and 1-year CTA was 40 and 378 days, respectively.
Patients with landing zone 0 underwent debranching of the supraaortic vessels. This surgi-

cal procedure was carried out by means of an end-to-side anastomosis between the partially clamped ascending aorta (AsAo) and brachiocephalic trunk and the left common carotid artery using a bifurcated polyester textile graft. The left subclavian artery was revascularized during TEVAR by carotid-subclavian artery bypass. Patients with landing zone 1 underwent right common carotid artery to left subclavian artery bypass (using an 8-10 mm diameter stretch polyester textile graft) while the left common carotid artery was remplanted on bypass with an end-to-side anastomosis.
Patients with landing zone 2 underwent carotid-subclavian artery bypass. Debranching was carried out by means of an end-to-side anastomosis between left common carotid artery and left subclavian artery using an 8-10 mm diameter stretch polyester textile graft.
Technical success was defined by accurate endograft deployment without the need of additional endograft deployment and coverage of a target selected aortic vessels. More details about debranching procedures are given in Section 2.4.

| | **Total** | **Group Z0** | **Group Z1-2** |
|---|---|---|---|
| $n$ | 22 | 10 | 12 |
| Age (years), mean ± SD | 70.4±12.5 | 72.7±6.9 | 68.5±15.5 |
| Female, $n$(%) | 7 (32%) | 3 (30%) | 4 (33%) |
| Hypertension, $n$ | 17 | 8 | 9 |
| Diabetes, $n$ | 3 | 0 | 3 |
| Chronic obstructive pulmonary disease, $n$ | 8 | 6 | 2 |
| Coronary heart disease, $n$ | 5 | 3 | 2 |
| Atrial fibrillation, $n$ | 3 | 3 | 1 |
| Chronic renal failure, $n$ | 3 | 2 | 1 |

Table 5.1: Patients' data and comorbilities. SD: standard deviation.

### 5.2.2 Imaging analysis protocol

All 22 patients underwent pre- and 1-month post-operative contrast-enhanced CTA, while 19 of them were considered for 1-year follow-up analysis; indeed, three patients did not undergo 1-year post-operative CTA due to death in one case and reintervention in two cases before 1-year follow-up completion. Slice thickness and pixel spacing were in the range 0.5-1.25 mm and 0.55-0.97, respectively, for pre-operative and post-operative CTA scans. All scans were transferred to a workstation in an anonymous format for image processing as described below. The whole processing procedure was performed using the open-source VMTK library. An overview of the image processing workflow is shown in Figure 5.1.

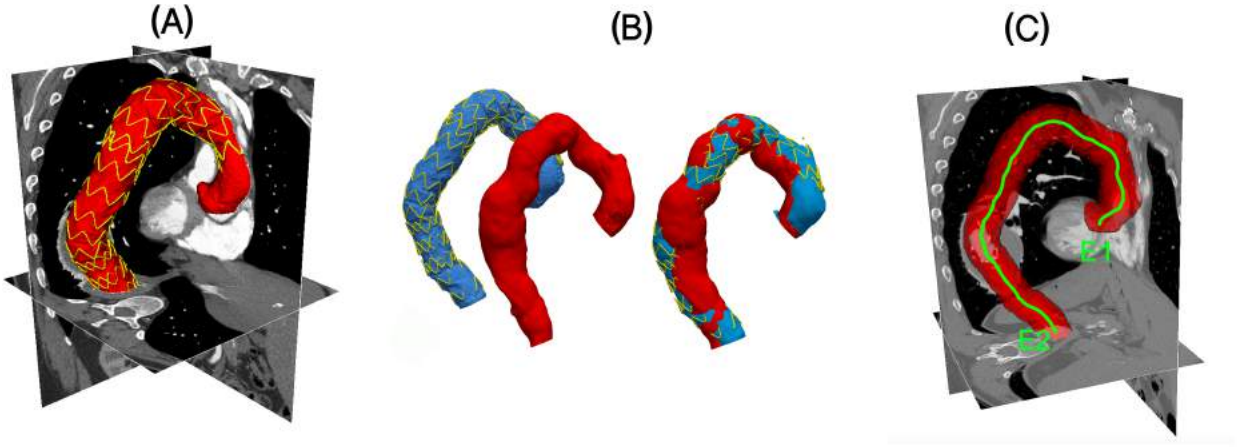


Figure 5.1: Workflow of the medical image analysis. (A) Starting from CTA images, the lumen (red) and the endograft (yellow) were automatically segmented; (B) the post-operative lumen surface (blue) and endograft surface (yellow) were superimposed to the pre-operative lumen surface (red); (C) centerlines were automatically computed from the aortic root (endpoint E1) to the coeliac trunk (endpoint E2).

Firstly, we performed a semiautomatic gradient-based level set segmentation of both pre-operative and post-operative images to extract a 3D model of the thoracic aorta lumen (see Section 2.7.4 for more details). Segmentation of post-operative images can be also used to retrieve the endografts 3D models. Afterwards, each post-operative vessel surface was automatically registered to the pre-operative one by means of the ICP algorithm [Besl and McKay, 1992], a robust method for rigid registration of 3D data, which is implemented in VMTK as well. Finally, pre- and post-operative centerlines from the aortic valvular plane (endpoint E1) to the plane crossing the celiac trunk (E2) were automatically computed [Piccinelli et al., 2009].

VMTK tool allows us to create an automated framework, consisting of a pipeline of instructions, that minimizes the users' interaction by limiting it to the segmentation phase. Therefore, we believed that the analysis of inter- and intra-observer variability can be neglected.

When the pre-operative 3D geometries involved saccular aneurysms, a virtual pre-operative surface model excluding the aneurysmal sac was created. This procedure was performed to prevent the vessel centerline from being affected by the bulbous protrusion. As previously introduced in Section 2.7.9, the original method already implemented in VMTK was partially modified to manually adjust the position of the two points delimiting the aortic aneurysmal sac.

Given the lumen centerline, we performed the following measurements: length of the whole centerline (L); length of the centerline covered by the endograft(s) (CL); distance from the

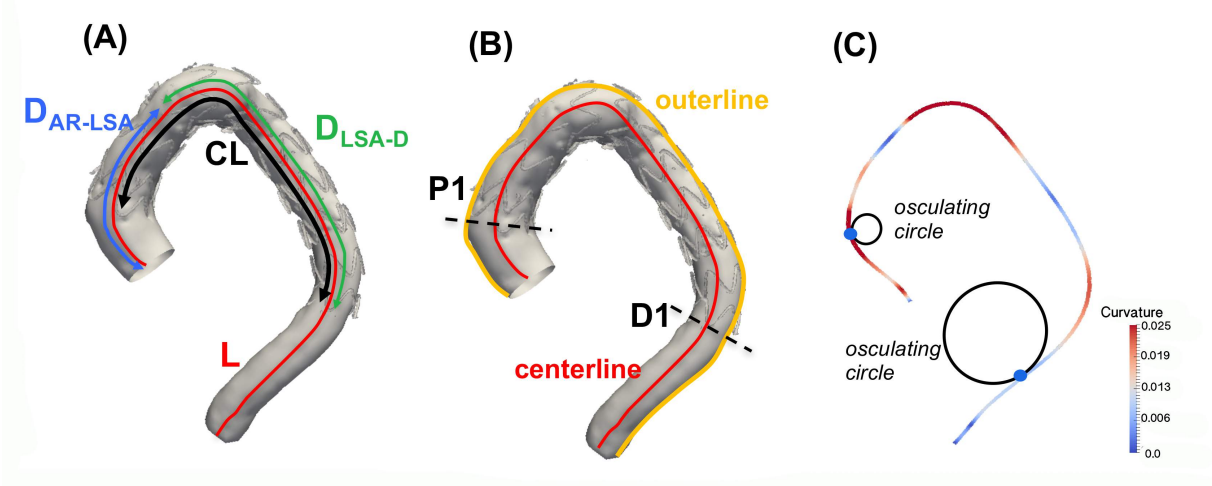


Figure 5.2: Geometric analysis of the aortic centerline. (A) Performed measurements: centerline length (L), distance from AR to LSA ($D_{AR-LSA}$), distance from LSA to distal landing zone ($D_{LSA-D}$). (B) Curvature was evaluated at proximal (P1) and distal (D1) landing points for both centerline and outerline paths. (C) local curvature computation: in each point the curvature value is extracted as the inverse of the radius of the local osculating circle.

aortic root (AR) to the proximal edge of LSA ($D_{AR-LSA}$); distance from the LSA proximal edge to the distal landing zone ($D_{LSA-D}$). CL was automatically computed by projecting the 3D model of the endograft(s) into the post-operative aortic lumen centerline. All these measurements are illustrated in Figure 5.2(A).
In addition to the centerline path, a custom script was implemented to extract the external path (outerline) of the vessel surface (see Figure 5.2(B)).
Curvature $\kappa$ was quantified along the extracted paths (centerline and outerline) for all patients. At a given point, curvature is defined as the inverse of the radius of the local osculating circle, i.e., the circle approximating the curve in a given point. On the basis of this definition, the value of curvature at a certain point quantifies its deviation from a straight line as illustrated in Figure 5.2(C).

Since pre-operative and post-operative vessel surfaces are registered, the position of the endograft was also identified onto the pre-operative path lines; thus allowing us to measure the local curvature values on both pre-operative and post-operative paths (centerline and outerline) in two specific points: proximal (P1) and distal (D1) extremities of the aortic portion involved in the endovascular implant(s). The position of these points is highlighted in Figure 2(B).
Furthermore, the values of local curvature computed along the centerline were averaged to obtain the pre- and post-operative mean curvature of the total aorta (TA) (from the AR to the

celiac trunk), of the AsAo (from AR to P1), of the endografting region (ER) (from P1 to D1), and of the descending aorta (DsAo) (from D1 to the celiac trunk). Calculations were made both for the whole group of patients (n=22) as well as for two sub-groups, i.e., Z0 (n=10) and Z1-2 (n=12). Patients with landing zones Z1 and Z2 were grouped together (Z1-2) due to the limited number of Z1 cases (n=3) and to similar aortic arch morphology between Z1 and Z2.

### 5.2.3 Statistical analysis

All statistical analyses were performed using the JMP 13.0 (SAS Institute Inc. Cary, NC, USA) software.
Data are shown as absolute frequencies, percentages, median with a range, and mean ± standard deviation, where appropriate. Shapiro-Wilk test and visual investigation of data with histograms were used to assess normal distribution of the data. All significant differences between pre- and post-operative geometric measurements were analyzed by means of the Paired-samples t-test. Comparisons between different groups of devices and the various pathologies were performed individually using one-way Anova for unequal sample sizes. Univariate correlations were examined using Pearson's correlation coefficient. P-values below 0.05 were considered statistically significant in all statistical tests. No correction for multiple testing was performed which could make significance only exploratory.
Although the pipeline we proposed allow to minimize the users' interaction, semi-automatic segmentation phase of the vessel could potentially lead to slight measurement differences. Therefore, to validate the obtained results, two independent skilled observers performed segmentation of CTAs images and subsequent centerline extraction and measurements, and one of them conducted it twice, allowing for inter-observer and intra-observer variability analysis using the intraclass correlation coefficient (ICC). Results were presented with the 95% confidence interval (CI).

## 5.3 Results

### 5.3.1 Study subjects

Altogether, 41 endografts corresponding to three different types of devices were deployed for the 22 procedures: 10 patients (45%) received the Low-Profile Zenith Alpha endograft (Cook, Bloomington, Ind), 7 (32%) received the Relay NBS endograft (Bolton, Barcelona, Spain) and 5 (23%) the Gore C-TAG endograft (W.L. Gore and Associates, Flagstaff, AZ).
Technical success was achieved in 100% of cases. No intra-operative deaths, paraplegia or other major complications occurred. The following complications were observed during follow-up: one case of type Ib endoleak at 1-month follow-up, one case of asymptomatic retrograde type-A aortic dissection (rTAAD) revealed by 1-month CTA which required reintervention, one case of aortic dissection on the distal landing zone at 3-months follow-up resolved by open

repair, one case of pseudoaneurysm with aortic rupture on the distal landing zone at 1-year of follow-up with required endovascular reintervention. Two deaths occurred within the 1-year follow up due to complications after reintervention. Of these two patients, one died from sepsis after open repair for rTAAD, the latter two months after reintervention for aortic rupture.

### 5.3.2 Analysis of geometric remodeling

#### 1-month follow-up

The values of computed geometrical quantities regarding both pre- and post-operative aortic centerline are reported in Table 5.2. The percentage of endograft coverage CL was 60.21% ± 17.73% and 1.818 ± 0.732 endografts were used per patient.
The values of computed geometrical quantities regarding both pre- and post-operative aortic centerline are reported in Table 5.2 (total group of patient), Table 5.3 (Z0 group) and Table 5.4 (Z1-2 group). The percentage of endograft coverage CL was 60 %±17 % and 1.8±0.7 endografts were used per patient. Although not statistically significant, longer segments of the aorta were stented in subjects in the Z0 group compared to those in the Z1-2 group (65±20% vs 56±15%, P=0.1).

| Measurements | Pre-operative | 1-month follow-up | 1-year follow-up |
|---|---|---|---|
| L [mm], mean ± SD | 382.7±48.7 | 388.1±50.7; P=0.010 | 395.1±47.7; P=0.001 |
| $D_{AR-LSA}$ [mm], mean ± SD | 114.1±18.7 | 117±19.3; P=0.02 | 119.7±17.9; P<0.001 |
| $D_{LSA-D}$ [mm] , mean ± SD | - | 190.5±79.9 | 192.5±74.6 |
| Centerline curvature *10 [1/mm], mean ± SD | | | |
| P1 | 0.22±0.08 | 0.27±0.16; P=0.011 | 0.4±0.2; P<0.001 |
| D1 | 0.09±0.063 | 0.15±0.12; P=0.004 | 0.23±0.13; P<0.001 |
| TA | 0.18±0.02 | 0.18±0.02; P=0.12 | 0.21±0.04; P=0.04 |
| AsAo | 0.19±0.04 | 0.21±0.04; P=0.02 | 0.24±0.08; P=0.05 |
| ER | 0.20±0.04 | 0.19±0.03; P=0.004 | 0.20±0.04; P=0.06 |
| DsAo | 0.11±0.05 | 0.12±0.07; P=0.090 | 0.18±0.07; P=0.02 |
| Outerline curvature *10 [1/mm], mean ± SD | | | |
| P1 | 0.32±0.23 | 0.49±0.37; P=0.01 | 0.4±0.18; P=0.04 |
| D1 | 0.11±0.06 | 0.18±0.09; P=0.04 | 0.41±0.04; P=0.04 |

Table 5.2: Measurements for the whole group of patients

After hybrid repair, centerline length significantly increased (P=0.010) for the whole group of patients, albeit to a rather small degree, i.e., 1.35%. Such a change in length was statistically

| Measurements | Pre-operative | 1-month follow-up | 1-year follow-up |
|---|---|---|---|
| L [mm], mean ± SD | 382.6±45.9 | 391.6±45.9; P=0.04 | 406.00±42.4; P=0.008 |
| $D_{AR-LSA}$ [mm], mean ± SD | 109.6±19.00 | 113.1±19.0; P=0.08 | 117.0±18.1; P=0.008 |
| $D_{LSA-D}$ [mm], mean ± SD | - | 196.1±91.5 | 198.1±66.5 |
| Centerline | | | |
| curvature *10 [1/mm], mean ± SD | | | |
| P1 | 0.27±0.07 | 0.35±0.19; P=0.06 | 0.47±0.29; P=0.05 |
| D1 | 0.09±0.07 | 0.14±0.09; P=0.04 | 0.23± 0.12; P=0.05 |
| TA | 0.10±0.02 | 0.19±0.03; P=0.3 | 0.21±0.006; P=0.08 |
| AsAo | 0.18±0.04 | 0.21±0.05; P=0.008 | 0.24±0.10; P=0.05 |
| ER | 0.20±0.03 | 0.19±0.03; P=0.05 | 0.20±0.04; P=0.1 |
| DsAo | 0.01±0.04 | 0.12±0.06; P=0.02 | 0.14±0.04; P=0.08 |
| Outerline | | | |
| curvature*10 [1/mm], mean ± SD | | | |
| P1 | 0.21±0.06 | 0.29±0.13; P=0.055 | 0.39±0.05; P=0.05 |
| D1 | 0.13±0.08 | 0.14±0.07; P=0.09 | 0.23±0.1; P=0.07 |

Table 5.3: Measurements for the Z0 group.

| Measurements | Pre-operative | 1-month follow-up | 1-year follow-up |
|---|---|---|---|
| L [mm], mean ± SD | 381.6±50.9 | 384.1±50.9; P=0.13 | 395.8±56.8; P=0.05 |
| $D_{AR-LSA}$ [mm], mean ± SD | 116.5±18.4 | 118.3±20.5; P=0.06 | 123.7±21.5; P=0.01 |
| $D_{LSA-D}$ [mm], mean ± SD | - | 186.2±73.3 | 188.8±83.3 |
| Centerline | | | |
| curvature *10 [1/mm], mean ± SD | | | |
| P1 | 0.18±0.07 | 0.24±0.15; P=0.03 | 0.36±0.13; P=0,02 |
| D1 | 0.09±0.06 | 0,16± 0.15; P=0.02 | 0.25±0.13; P<0.001 |
| TA | 0.18±0.02 | 0.17±0.02; P=0.2 | 0.21±0.04; P=0.006 |
| AsAo | 0.20±0.03 | 0.020±0.02; P=0.3 | 0.24±0.04; P=0.03 |
| ER | 0.19±0.04 | 0.18±0.03; P=0.04 | 0.2±0.03; P=0.1 |
| DsAo | 0.12±0.06 | 0.12±0.03; P=0.4 | 0.19±0.08; P=0.006 |
| Outerline | | | |
| curvature*10 [1/mm], mean ± SD | | | |
| P1 | 0.40±0.28 | 0.64±0.42; P=0.01 | 0.58±0.2; P=0.03 |
| D1 | 0.11±0.05 | 0.21±0.10; P=0.03 | 0.45±0.1; P=0.05 |

Table 5.4: Measurements for the Z1-2 group.

significant in the Z0 group (P=0.04) alone, showing an average increase of 2.3%; conversely, the Z1-2 group did not show centerline lengthening (P=0.1).

The degree of point-wise curvature at endograft landing points was assessed numerically (see Figure 5.3). Already 1-month after treatment, centerline local curvature was significantly greater in both P1 (P=0.011) and D1 (P=0.004). Considering the Z0 group, an increase of curvature in P1 was detected even if no statistical significance was reached (P=0.06), whereas centerline local curvature increased significantly (P=0.04) in the distal landing zone D1. With regard to the Z1-2 group, a significant increase of the curvature was found in both the P1 (P=0.03) and D1 (P=0.02) zones.
Similarly, point-wise curvature of the surface outerline (see Figure 4) significantly increased in P1 (P=0.01), and D1 (P=0.04) for the total group of patients. No statistically significance was reached for the Z0 group even if an increase of about 40% of curvature values was detected in P1 (P=0.055); whereas, considering the Z1-2 group, a significant increase was observed on both P1 (P=0.01) and D1 (P=0.03).
Following hybrid repair, the centerline mean curvature showed a significant increase (+7%) in the AsAo (P=0.02) and a significant decrease (-3.3%) in the ER (P=0.004). Regarding the mean curvature values in group Z0, a statistically significant increase (+14.5%) in mean curvature was observed in the AsAo (P=0.008) together with a decrease (-3%) in mean curvature in the ER (P=0.05). For group Z1-2, a significant reduction (P=0.04) in mean curvature values was observed in the ER (-3.4%). No device-related differences were observed among the three groups. Subsequently, considering the pathology, no significant differences were detected for any of the computed parameters, except for the change in centerline length. In particular, a greater increase in centerline length was observed in the aneurysm group.
Considering the number of deployed stents, no differences were found regarding the changes in centerline lengths. No statistically significant correlation was found between the coverage length CL and the other computed quantities. No correlation was found between centerline length increase and mean curvature increases.

#### 1-year follow-up

The analysis performed at 1-year follow-up confirmed the remodeling trend of the aorta. In particular, as concerns the centerline length a mean increase of +12.3 mm was observed if compared to pre-operative configuration. At 1-year follow-up, values of point-wise curvature at proximal and distal landing zones confirm the increase already observed at 1-month follow-up; the same comment applies with the mean curvature increase in the unstented regions of both ascending and descending aorta.

### 5.3.3 Intra-observer and inter-observer reproducibility

Intra-observer and inter-observer reproducibility analyses were computed by ICC. Intra-observer ICC index resulted 0.98 (95% CI 0.97 - 1.00) for length measurements. Inter-observer analysis showed an ICC index of 0.97 (95% CI 0.97 - 0.98) for length measurements. These results

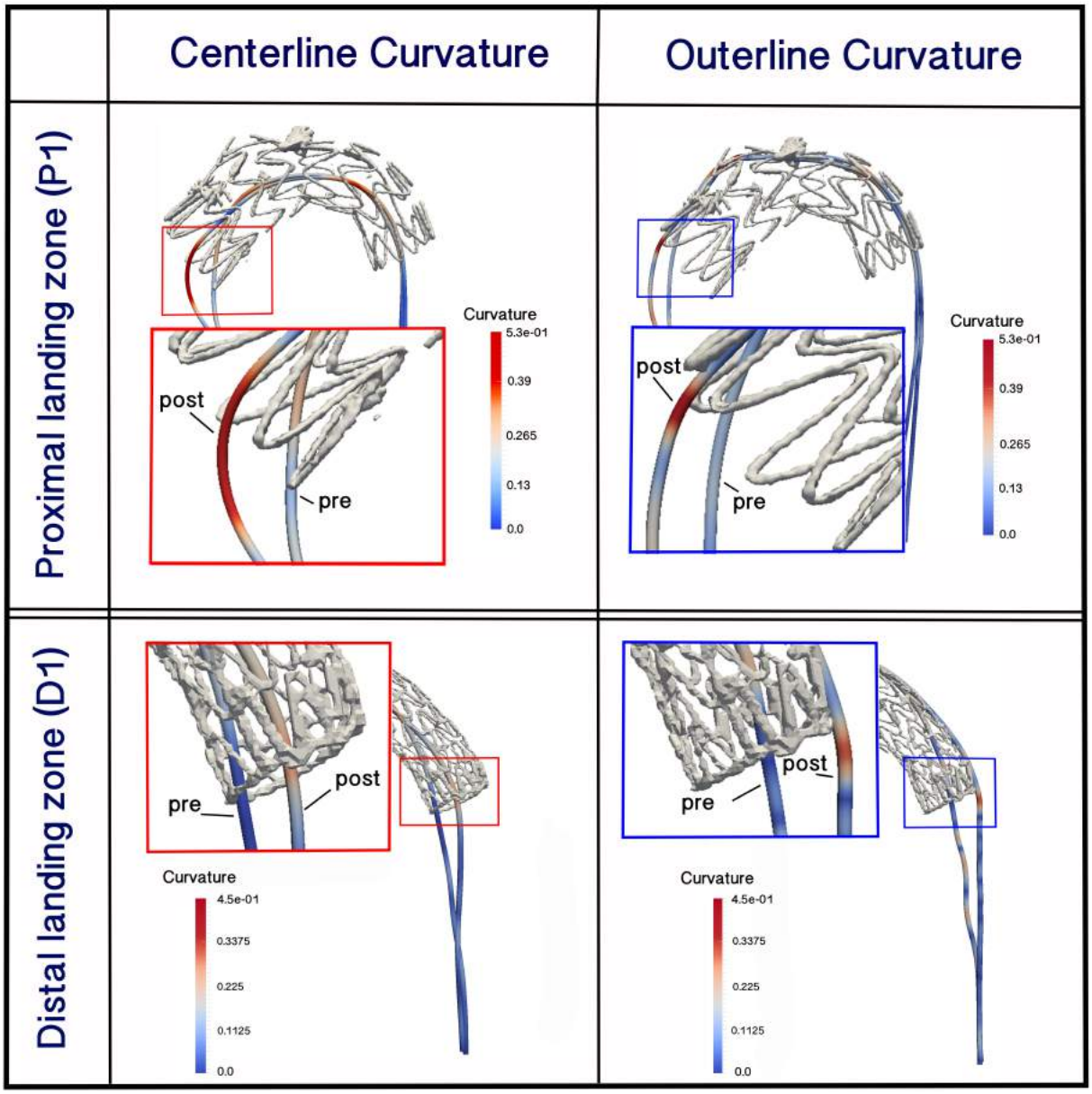


Figure 5.3: Curvature changes at proximal (P1) and distal (P2) landing zones between pre-operative and post-operative configurations are highlighted. Left column concerns centerline values whereas in the right column vessel outerline is considered. Both lines are colored with respect to point-wise curvature value: color scale legend ranges from blue (minimum value) to red (maximum value).

indicated excellent intra-observer agreement and inter-observer agreement for length measurements.

## 5.4 Discussion

The endovascular treatment of aortic diseases involving the thoracic area presents several anatomical challenges (i.e., complex 3D anatomy and supraaortic vessels presence).
In particular, the high variability of the aortic arch anatomy [Boufi et al., 2017, Girsowicz et al., 2017], which is further modified by the pathologies [Alberta et al., 2015], leads to a specific adaptation between endograft and aortic wall depending on each type of morphology. Therefore, with the currently available thoracic endoprostheses, a total endovascular repair of the aortic arch requires devices that need to be customized for each patient's anatomy and pathologic condition and often surgical left subclavian artery revascularization is required.
Thus, the hybrid procedure of the aortic arch, which includes supraaortic vessels transposition to obtain an adequate proximal landing zone for TEVAR in zones 0, 1 and 2, has proven to be an effective alternative, especially in high risk patients, in an effort to reduce peri-operative death and complications related to open surgical repair [Milewski et al., 2010]. However, the long-term outcomes of hybrid treatment still remain a source of concern, and severe complications could occur during follow-up [Geisbüsch et al., 2011]. When passively bent inside an highly curved artery as the aortic arch, the endograft exerted a spring-back force at the proximal and distal ends due to the inherent tendency to recover its original straight status [Dong et al., 2010]. As already postulated, this spring back force could causes an increasing of stress on the outer wall, especially at the endograft landing zones, ultimately leading to endograft-related vessel injuries [Guan et al., 2018].
The aim of this study was to analyze the immediate geometric changes of the aortic arch after hybrid treatment, with a particular focus on the endograft landing zones, attempting to enhance the understanding on the possible reasons for the development of device-related complications.
Our results indicated that hybrid treatment modifies the morphology of the aortic arch tract, with both a significant elongation of the vessel and an increase in point-wise and mean curvature along the vessel.
In particular, with regard to the centerline length, a mean increase of 5.3 mm (P=0.010) was observed already at 1-month after the treatment and it increased to +12.3 mm (P=0.001) at 1-year follow-up; this result is consistent with the outcomes reported by Nauta et al. [Nauta et al., 2017] and Naguib et al. [Naguib et al., 2016]. After hybrid treatment, the local curvature of the centerline was significantly greater in the endograft proximal landing zone compared to the pre-operative configuration, which supports the findings by Midulla et al [Midulla et al., 2014]. Moreover, we also observe a significant increase in the centerline local curvature at the distal fixation zone, for which no comparative results can be found in the literature.

The significant increase in centerline and outerline curvature at endograft landing points reveals the tendency of the endograft to spring back to its original straight status, as already postulated by Dong et al. [Dong et al., 2010] and Jánosi et al. [Jánosi et al., 2015] for AD treated with TEVAR. The possibility that the elastic recoil of the endograft might cause new entry tears in proximal and distal landing zones has been described as well. On the basis of our data, we could suppose that the force exerted by the endograft proximal and distal ends on the aortic wall might contribute to neck degeneration which is ultimately related to aneurysm formation or endoleak development.

After intervention, the mean curvature of the centerline in the AsAo showed a significant increase, which positively correlated with an increase in the reaction force on the wall [Poullis et al., 2008], ultimately leading to the development of rTAAD [Taguchi et al., 2014]; such an increase of mean curvature was higher in patients treated in the most proximal landing zone (i.e., zone 0). According to Chen et al. [Chen et al., 2017], the occurrence rate of rTAAD in zone 0 was demonstrated to be higher than in other landing zones. Moreover, Redheuil et al. [Redheuil et al., 2011] previously demonstrated a strong correlation between proximal aortic arch morphological changes and left ventricular remodeling, together with increases in brachial blood pressure and mean and pulse pressures in subjects with no overt cardiovascular diseases. In addition, as documented by Kadoglou et al. [Kadoglou et al., 2014], pulse wave velocity, a clinically recognized marker of arterial stiffness, significantly increased after TEVAR. Although the correlation of the morphological changes of the aorta following the hybrid procedure with the above-mentioned biomechanical aspects is beyond the scope of the present study, it warrants the attention of future multidisciplinary analyses.

The decrease in mean curvature we observed in the ER confirms the inherent tendency of the graft to turn back to straight. However, we currently know very little about the mechanical properties of the endografts and how these differences could deeply modify the behavior after implantation [Georg et al., 2017]. Differences of *in vivo* behavior with different models of endografts compared to their differences in the mechanical characteristics could help in designing next generations of endograft with better conformability and thus lowering the risk of intrinsic damages [Bussmann et al., 2017].

Our findings confirm that the aortic arch segment is a critical zone for endograft apposition. In this regard, as already mentioned, short-term complications were observed in two patients (8.7%): one case of type IB endoleak occurred and one patient underwent re-intervention due to rTAAD. The former patient exhibited an increase in centerline curvature of 110% and outerline curvature of 75 % in the distal landing point, while in the latter case, the patient showed an important increase of both outerline and centerline curvatures at the P1 level (more than 100% increase) along with a 22.5% increase in the centerline mean curvature of the AsAo.

## 5.5 Limitations

The main weakness of the present study is the small number of enrolled patients, although the sample size is consistent with recent studies regarding quantitative assessment of aortic arch geometry [Mestres et al., 2017]. Another limitation regards the absence of a standardized protocol for the acquisition of CTA images, which is due to the retrospective design of the study. In addition, CTA acquisitions were not ECG-synchronized because this technique was not available at our center for daily clinical practice. However, it is worth noting that even other studies, which are similar to the present one, did not make use of ECG-gated CTAs (Mestres et al. [2017], Naguib et al. [2016], Midulla et al. [2014]).

## 5.6 Conclusion

In conclusion, we have demonstrated that hybrid treatment is associated with a significant elongation of the vessel and a significant increase in curvature on the AsAo and on endograft landing zones which could be predictive of the development of device-related complications. This issue reveals the need for further investigation into more conformable and dedicated endografts, or even precurved endografts, for different thoracic aortic diseases.
Future studies involving the analysis of diameters changes and its correlation with aortic centerline elongation, endograft oversizing, radial force on proximal and distal landing zones should be performed.

# Chapter 6

# 12-year follow-up post-TEVAR in type B aortic dissection shown by 3D printing

In this chapter we will show a case report regarding the remodelling of the aortic vasculature during time in a patient primarly submitted to endovascular procedure for type B aortic dissection. In this work we made use of the 3D printing technology to better show the aortic changes during time. This project was performed in collaboration with the laboratory of 3D printing of the Department of Civil Engineering and Architecture of University of Pavia and in particular with Eng. Stefania Marconi. [4]

## 6.1 Introduction

Recent guidelines recommend thoracic endovascular repair (TEVAR) as the first-choice treatment for patients affected by complicated type B acute aortic dissection (TBAAD) [members et al., 2014]. Although this treatment has reduced morbidity and mortality rates considerably as compared to open-surgery, the re-intervention rate still remains high [Kret et al., 2013]. However, little is known about the long-term outcome of patients with TBAAD treated by TEVAR [Lou et al., 2018]. In addition, given the fact that aortic dissections usually present at a younger age than aneurysms or penetrating aortic ulcers [Mussa et al., 2016], establishing a life-long imaging follow-up protocol following TEVAR is mandatory. We herein present the complications and re-intervention modalities that were faced during the 12-year follow-up after TEVAR in a patient who initially presented with complicated TBAAD. Each step of

[4] This chapter is based on:

- Finotello A, Marconi S, Pane B, Conti M, Gazzola V, Mambrini S, Auricchio F, Palombo D, Spinella G. Twelve-year Follow-up Post-Thoracic Endovascular Repair in Type B Aortic Dissection Shown by Three-dimensional Printing. Annals of Vascular Surgery 2019; 55: 309-e13.

the follow-up is presented with the aid of 3D printed replica of the patient's anatomy, which help in emphasizing the need for close, lifelong follow-up. 3D printing technology is rapidly spreading in the last years as an important clinical tool for planning of complex surgeries as it is considered more informative to both 2D and 3D imaging [Marconi et al., 2017]. Previous studies have already highlighted the feasibility and accuracy of 3D printing to reproduce physical models [Ho et al., 2017] and the importance of such models to facilitate decision making and device selection in a complex abdominal aortic case [Tam et al., 2013]. Secondary aims include demonstrating the importance of 3D printing technology in pre-operative planning, helping patients fully understand their condition and the potential complications, and training future specialists using models that are tailored to specific cases.

## 6.2 Case Report

In May 2005, a 66-year old man with a past history of hypertension presented to our hospital with abdominal and lower back pain. The patient underwent a computerized tomography angiography (CTA) scan which revealed TBAAD complicated by impending aortic rupture (Step 1). As shown in Figure 6.1, the false lumen supplied blood to the left renal artery, while the true lumen fed the celiac trunk, the right renal artery, and the mesenteric arteries. Pre-operative CTA (see Figure 6.1C) shows the primary entry tear located in the proximal tract of the descending thoracic aorta and a large re-entry tear in the right common iliac artery (see Figure 6.1D-F).

To manage the TBAAD, endovascular treatment was performed by positioning a thoracic Zenith Cook (Cook Inc, Bloomington, Ind) endoprosthesis (ZTEG-2P-40-216) in correspondence of the proximal entry tear (Step 2). Post-intervention CTA examination showed that with the endograft in the correct position there was no filling of the false lumen from the entry tear, however, the distal false lumen remained patent.
After endovascular treatment, the patient carried out regular annual follow-ups which showed a dissected chronic type IV thoraco-abdominal aneurysm (see Figure 6.2) that continued to grow over time.
Six years after endovascular treatment, when the aneurysm reached its maximum diameter of 68 mm (see Figure 6.2D), the patient underwent open surgical treatment with aorta replacement, aortic re-implantation of both left and right renal arteries and bypass of the celiac and superior mesenteric arteries. Proximal anastomosis of the aorto-aortic graft was carried out distally from the thoracic aortic endoprosthesis in a non-aneurysmal tract where several pairs of intercostal arteries originate in order to reduce the risk of paraplegia.

During follow-up, aneurysmal dilatation of up to 59 mm in diameter of the ascending aortic arch and the right hemiarch was observed. Nine years after the first endovascular treatment,

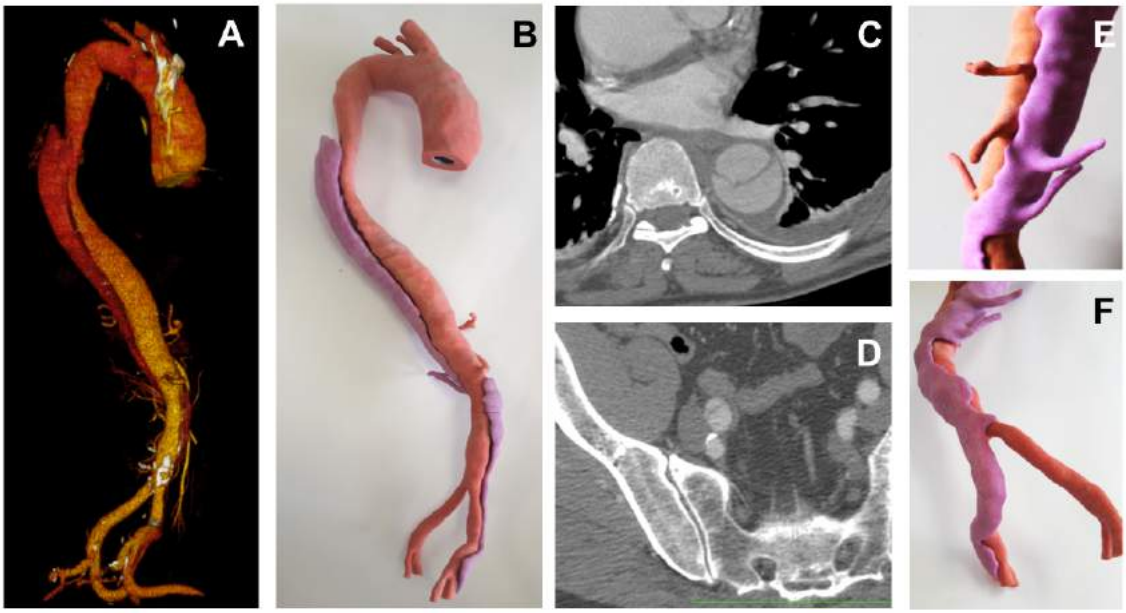


Figure 6.1: (A) Pre-operative 3D rendering of TBAAD is compared to (B) 3D printed hollow model: true lumen is colored red and false lumen is pink. (C) principal entry tear and (D-F) re-entry tear. (E) detail of the lateral branches.

the patient underwent ascending aorta replacement with transposition of the anonymous trunk and the left common carotid artery.
Eleven years after the first endovascular treatment, during follow-up CTA, gradual enlargement of the descending thoracic aorta between the thoracic endoprosthesis and the surgical graft was detected (Step 3). As depicted in Figure 6.3, type IB endoleak was diagnosed.

Taking into account the patient's age and the previous interventions, a totally endovascular treatment using fenestrated branched stent-grafts was planned. The intervention was carried out in two stages in order to reduce the risk of paraplegia. In the first stage (Step 4), a proximal side-branched custom made Zenith Cook endograft 46-30-230 was positioned to preserve intercostal branch flow with partial overlapping on the previously implanted thoracic endoprosthesis (see Figure 6.4). A distal custom-made fenestrated Zenith Cook 32-32-113 endograft was also implanted with fenestration to allow for superior mesenteric artery, celiac artery and right renal artery bypass (two fenestrations). During the same session, treatment of the renal artery was completed by positioning an Advanta (Atrium Europe, Mijdrecht, The Netherlands) 7x20 mm covered graft. The 3D printed model shown in Figure 6.4 allowed us to observe the patency of the secondary branch arising from the descending thoracic aorta. Three months later, in the second stage, an Advanta 9x36 mm covered stent was positioned with

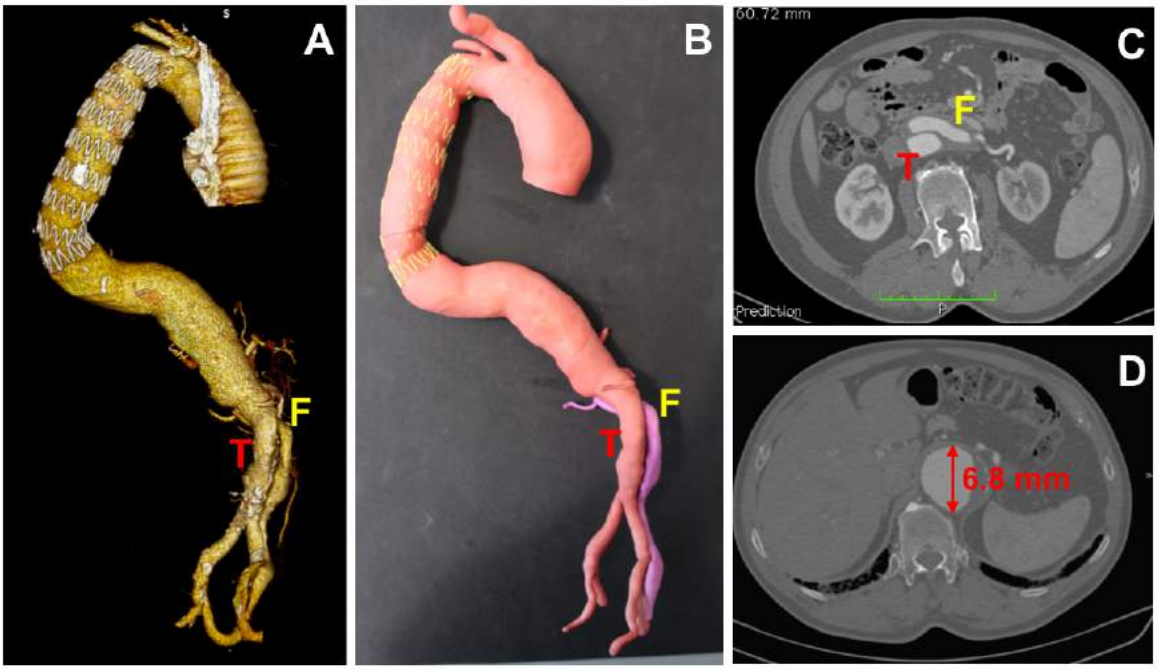


Figure 6.2: (A) 3D rendering and (B) 3D printed model show a chronic dissected TAAA. True (T) and false (F) lumen are highlighted both in the 3D models (A-B) and in the CT (C). (D) Maximum diameter reached 6 years after the first TEVAR intervention.

bypass of the superior mesenteric artery and the celiac trunk with left humeral access. Lastly, the side-branch was covered by positioning a Zenith Cook Thoracic endograft (Step 5). The patient was discharged on the sixth post-operative day with no post-procedural complications, under antiplatelet therapy. The 1-month post-operative CTA showed complete exclusion of the aneurysm with patency of all the vessels that underwent endovascular treatment. This was also confirmed by the 12-month follow-up CTA scan. Figure 6.5 shows the outcome of the endovascular procedure.

## 6.3 Methods

The entire follow-up sequence and the interventional procedures (Steps 1 to 5) were well documented by 3D printed models. An overview of the procedure workflow is given in Figure 6.6. Starting from CTA DICOM images, digital preparation of the virtual 3D models is performed using the Vascular Modeling Toolkit (VMTK) open source library (http://www.vmtk.org).


Figure 6.3: (A) 11-year follow-up CT scan is compared to (B) the 3D model showing distal neck degeneration and type IB endoleak.

First of all, image segmentation was performed by using the semi-automatic gradient-based level set technique. The *colliding fronts* initialization is adopted to extract the vascular structures; metallic stentgraft are initialized by means of the Threshold pattern. Once the segmentation is performed, the image is converted into a 3D surface using the Marching Cubes algorithm [Lorensen and Cline, 1987] implemented in VMTK as well. Surface remeshing and smoothing (Taubin method [Taubin, 1995]) are applied to improve the quality of the reconstruction. The 3D reconstruction procedure is repeated for each structure of interest (i.e., true lumen, false lumen, endograft).
Afterwards, the STL files undergo an additional post-processing phase, performed using the software Netfabb (Autodesk) fitted for additive manufacturing and design software in order to make the surfaces fit for printing.
Finally, the full-size physical models are manufactured by binder jetting technology (Project 460+, 3DSystems) which is an additive manufacturing process in which layers of materials are bonded to form an object. First, the 3DEdit (3D Systems) software is used to assign

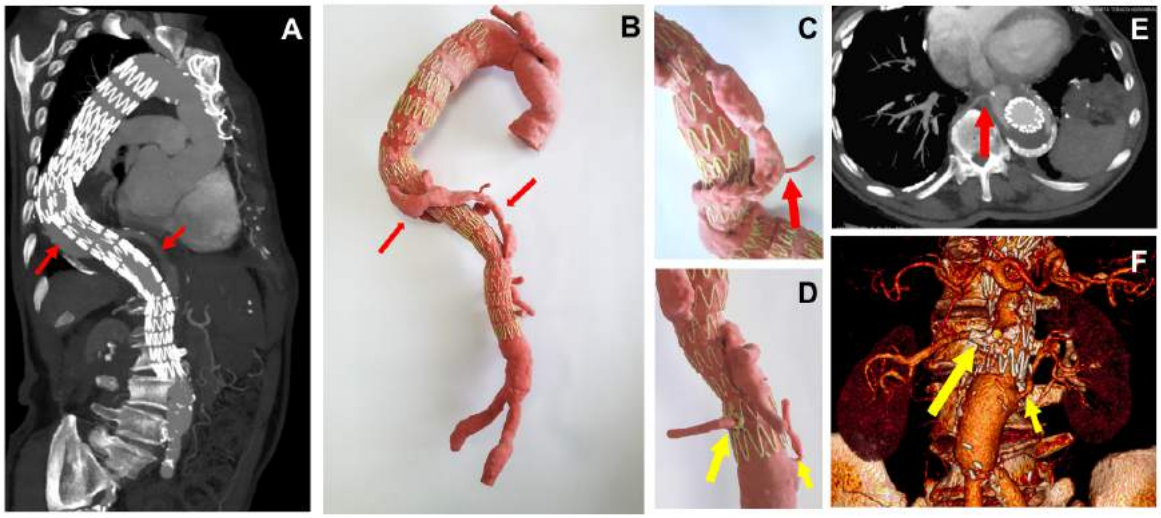


Figure 6.4: (A) CT scan and (B) the corresponding 3D model show the outcomes of the first stage of the planned two-stage totally endovascular treatment. As shown by the red arrows (A-B), intercostal branch flow was preserved to reduce the risk of paraplegia. (C) A detail of the 3D printed model showing the preserved intercostal artery, as also depicted in (E). Yellow arrows in (D) and (F) highlight patency of the descending aorta secondary branches.

different colors to each structure of interest and to obtain the hollowing of the structures which reduces the amount of material to be used. The 3D printer software selects the best slicing and slices the file creating layers of this cross sections of the object. Then, the model is prototyped using a chalk-like powder that is glued together by means of a liquid binder, along with colors deployed through an inkjet cartridge. The selected printer allow to obtain high chromatic resolution (up to 2.8 millions of colors) and to reproduce fine details (100$\mu$m of thickness resolution).
After the 3D printing, the physical model is post-processed using a cyanoacrylate infiltrating binder to strengthen the mechanical properties of the 3D printed model.

## 6.4 Discussion

We report the case of a patient treated for complicated acute type B AD. Endovascular repair successfully excluded the entry tear but during follow-up the patient experienced several complications thus making it clear the need for accurate and lifelong follow-up.
TEVAR has recently been accepted as the standard of care for complicated TBAAD [members et al., 2014]. Although promising short- and medium-term results after TEVAR have been

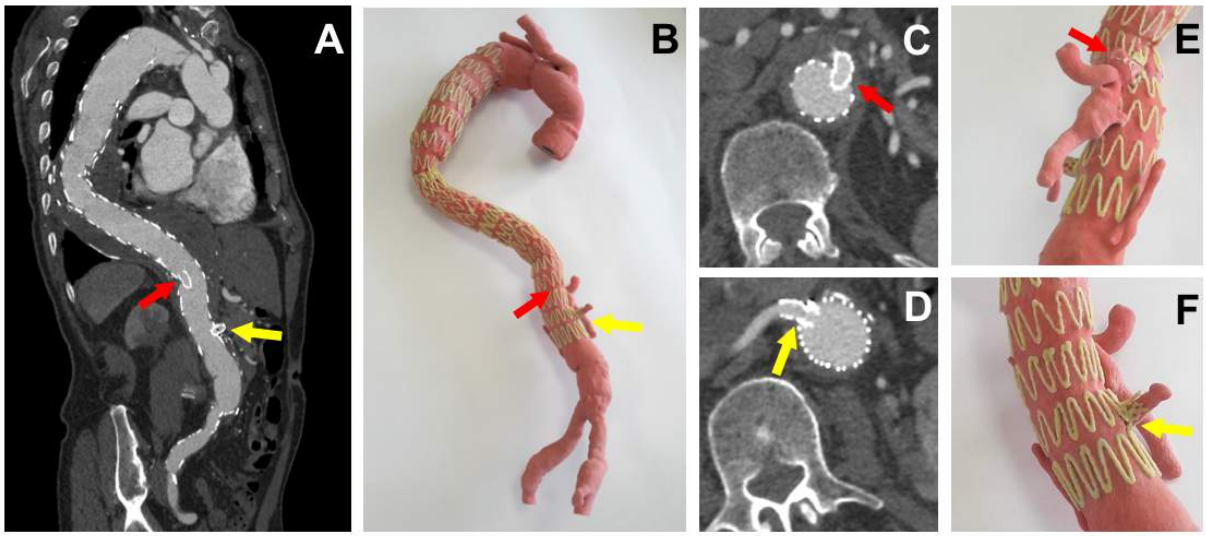


Figure 6.5: Completion of the two-stage endovascular procedure. The intercostal artery was covered. Superior mesenteric artery and celiac artery (red arrows) and right renal artery bypass (yellow arrows) were shown in detail.

well documented [Zhang et al., 2017], significant concerns remain regarding the long-term durability of the endovascular repair.

Current guidelines recommend CTA scans at 1, 6, and 12 months during the first post-operative year and annual life-long CTA/magnetic resonance imaging (MRI) thereafter [members et al., 2014]. In addition to monitoring the successful sealing of the primary entry tear and the possible false lumen thrombosis, surveillance of the changes in the non-stented aortic segment (which is susceptible to progressive aneurysmal expansion) is essential. Famularo et al. [Famularo et al., 2017] recently conducted a systematic literature review on medium- and long-term outcomes after TEVAR for the treatment of TBAAD. They reported growth of the thoracic aorta in 6.6% to 84% of the patients across 17 studies, and abdominal aorta enlargement in 10% to 54% of the patients. Similarly, Kang et al. [Kang et al., 2011] observed a re-intervention rate of 22%, which was mainly due to an excessive enlargement of the untreated aorta, in a cohort of 79 patients with complicated chronic distal aortic. Re-interventions are usually performed by open repair, by aortic hybrid procedures, and by total endovascular techniques using custom-made or standard off-the-shelf fenestrated stent grafts [Weber et al., 2016].

In our case study, we successfully treated the patient with endovascular coverage of the dissection entry tear located in the thoracic descending tract. However, after surgery, the presence of progressive aneurysmal dilatation together with the persistent false lumen patency with the left renal artery still originating from it, support the decision for re-intervention. In our case, due to the patient's relatively young age and the absence of severe comorbidities, for the first

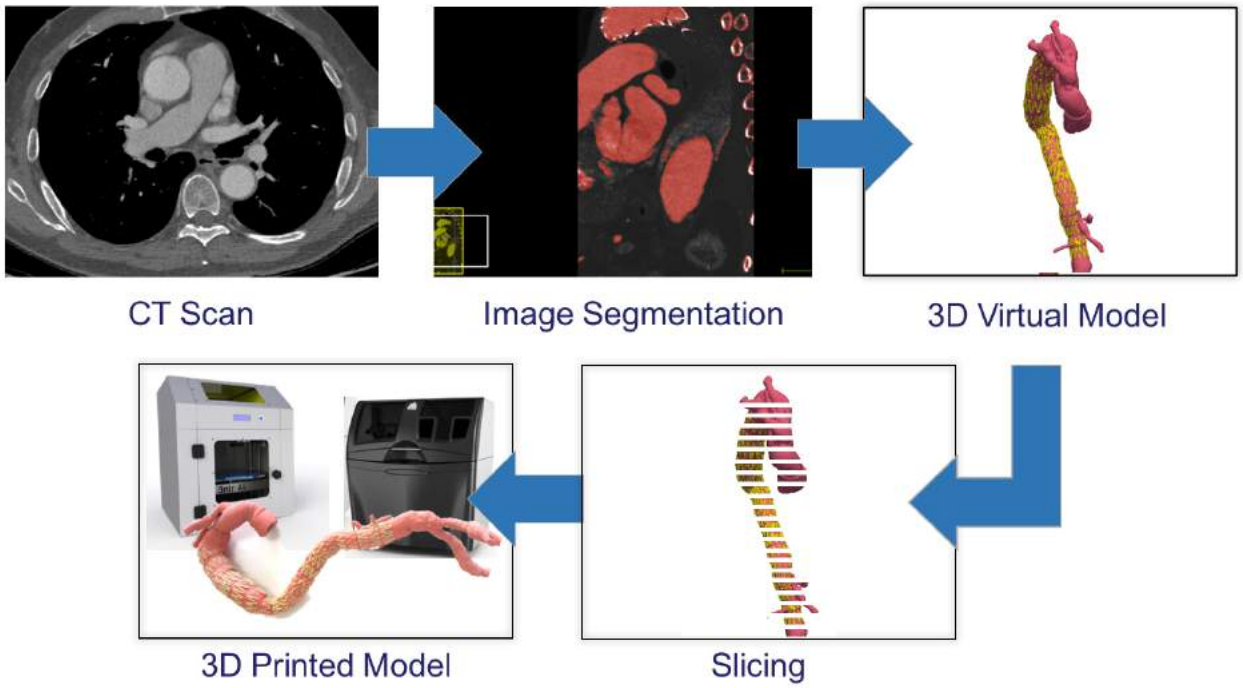


Figure 6.6: 3D printing workflow: from CT acquisition to the 3D printed model.

re-intervention we decided to proceed with open surgical repair. The surgery was performed preserving the patency of the two intercostal arteries. Over time, however, the aortic tract where the intercostal arteries originate became aneurysmatic and developed type IB endoleak in the aortic tract distal to the endograft. Re-intervention was therefore required and, taking into account the previous surgeries, a two-staged fenestrated endovascular aortic repair was planned.

The present study took advantage of 3D printing technology as a valuable tool to support the follow-up of the patient. Since the first 3D printing technology was patented in 1986 [Hull, 1986], there has been an exceptional spread around the world, especially in recent few years, with many new technologies and materials brought to the market. 3D printing technology was born as a prototyping technology, to be used in the industrial field for the production of preliminary copies of a final product to be produced using standard manufacturing technologies. Nowadays, thanks to development of a wide range of materials, 3D printing is broadening its applications in many other fields. State-of-the-art 3D printers are able to reproduce objects of even extremely complex geometries: relying on a layer-by-layer approach, 3D printers are able to face even shapes impossible to realize with other manufacturing technologies. Moreover, this technology is particularly suitable for the production of single copies or small batches of

an object, since the price per copy does not reduce increasing the number of products, as it happens for example in injection molding. Thanks to these characteristics, 3D printers appear to be particularly suitable for the production of personalized products: accordingly, they started to be investigated in the medical field for the production of patient-specific devices.
In recent years the number of applications of 3D printing in the field of medicine has exponentially increased. Existing and potential medical uses range from orthopedic reconstruction and implants [Auricchio and Marconi, 2016] to living tissue fabrication [Murphy and Atala, 2014]. Although it was initially only used as a tool for pre-operative planning [Itagaki, 2015], 3D printing technology is now emerging as a powerful tool for patient education, device optimization, and clinical training [Marro et al., 2016].
As concerns vascular and cardiovascular surgery, 3D printing has been used to better understand the unique pathological anatomy, to plan the best treatment and to assist in the device selection [Tam et al., 2013]. However, at the same time, the use of 3D full size objects to help medical students and residents understand the course of vascular pathologies is currently not still very widespread in the field of vascular surgery [Marconi et al., 2017].
3D printed life-sized models have been successfully employed during follow-up by our group to better evaluate both the evolution of the pathology related to the onset of complications and the outcomes of re-interventions. As already demonstrated by Marconi et al. [Marconi et al., 2017] for laparoscopic surgery, the tactile inspection of the printed models allows a better understanding of the patient's 3D real anatomy, increasing the understanding of the sense of depth and anatomical relationship between the different anatomical structures. In particular, the aorta has a complex anatomy with a great number of secondary branches originating from it, making the mutual relationship between pathological section and the arterial branches the not trivial to understand with standard visualization of CTA images by means of flat screens. Our experience allows confirming the literature data about the superiority of 3D printed models with respect to standard imaging also for follow-up monitoring, an application not yet investigated. For example, the 3D printed models depicted in Figures 6.1 and 6.2 were beneficial to show the remodeling of true and false lumen after endovascular treatment, and, in particular, to better understand the real 3D relationship between true and false lumen and arterial secondary branches which originate from the two channels, and its changes before (Figure 6.1) and after (Figure 6.2) endovascular repair. Similarly, the 3D printed model of Step 3 (see Figure 6.3) allowed to observe the dislocation of the endograft leading to endoleak development and the metallic rings distortion which were hardly visible on CTA images.
Importance of visual inspection of 3D printed models is also confirmed by the 3D printed replica of the last two surgical steps. In particular, the 3D printed models allow to clearly observe the patency of the intercostal artery after Step 4 and completion of the endovascular procedure with coverage of intercostal artery and flow exclusion from the aneurysmal sac (see Figure 6.5). Moreover, both 3D printed models offer a clear view about the spatial relationship between the endograft distal landing zone and the just-below re-implanted celiac trunk. 3D printed models enable an immediate and effective comparison of the clinical situations at different times, without the need of going through the analysis of different image datasets. This

aspect is particularly valuable for complex anatomies to be investigated in detail. Another interesting perspective confirmed by this work concerns the use of 3D printed models as a valuable teaching tool for both skilled surgeons and for residents, medical students and other professional figures in the medical field. Moreover, they could help the patient understand his/her clinical situation, the therapeutic strategies proposed and the related risks. All these applications can be translated into a clinical outcome improvement as well as into a money saving for the hospital, especially as concerns the prevention of possible legal issues for malpractice.

In this case report we make use of 3D printing technology to accurately reproduce 3D printed color models of patient-specific life-size vasculature. Among the current available options, we opted for a binder jetting 3D printer which offers, with respect to the specific application, the best compromise between level of accuracy (100$\mu$m of layer thickness), construction speed (23 mm/h, resulting in a total of 10 hours for the printing plus 2 hours for the post-processing) and lower fabrication costs (about 200 euros for printing and post-processing) if compared to other techniques. Moreover, its intrinsic functioning enables to reproduce very complex structures without the need of supports' placement and their mechanical removal, since the model is continuously self-supported by the uncured powder during the printing. Production time and cost are the key points to evaluate the effective introduction of 3D printing into the daily clinical practice.

At the present state 3D printing is mostly applied in isolated cases or few number of cases, often demanding the production to producers external to the hospital, thus increasing costs and delivery time. The time required to process the images and produce the model limits the application of 3D printing for the production of patient-specific models only to elective surgery. In the present study, each model took about 24 hours to move from CTA images to the final 3D printed model. Image elaboration time is reduced for bones models, thanks to the easier segmentation process, while is extended to up 1 day for abdominal parenchymal organs. The application to emergency surgery, is accordingly prevented.

Considering the benefit brought by the technology at different levels, as proved by the present study, the introduction of 3D printing technology as an additional support for surgeons and clinicians should be promoted. Even if the choice of the most suitable technology should consider the specific fields of application, all the medical specialties could take advantage from the 3D printing.

The high innovation rate of 3D printing technologies and materials will probably lead to a cost reduction of both machines and supplies, hopefully boosting the use of 3D printing technologies for the daily clinical practice.

## 6.5 Conclusion

Our experience demonstrates the effectiveness of TEVAR in the short- and medium-term follow-up as a treatment option for complicated TBAAD. However, the long-term complications that were observed in this patient during long-term follow-up support the importance of lifelong CTA surveillance.
Furthermore, the study highlighted the effectiveness of 3D printed supports. Besides being especially useful in both pre-operative planning and device selection, the use of 3D printed patient-specific models could also be beneficial in follow-up monitoring, in teaching residents and medical students how to deal with complicated cases.

# Chapter 7

# Patient-specific structural simulations of endovascular repair to predict complications

The field of aortic endovascular treatment is currently in continuous expansion and recent International Guidelines [Schermerhorn and Jones, 2017] suggest it as treatment of choice in substitution to traditional open surgery for treatment of the main pathologies of abdominal and thoracic aorta. However, the high follow-up reintervention rate remains the Achilles' heel of thoracic endovascular repair. Early TEVAR failures involve delivery, deployment, and conformation to the local aortic anatomy. Also mid- and long-term complications after TEVAR could be related to the sub-optimal apposition of the device to the aortic wall [Grabenwoger et al., 2012]. In order to prevent such problems, the angulation of the aorta and the predictable position of the stent graft after deployment have to be well estimated. Moreover, when multiple overlapped endografts are deployed, the implantation sequence should be accurately planned.
Computer-based simulations are gradually emerging as a useful tool both for the virtual testing of endovascular prostheses and for the virtual simulation of the interventions and the relative exploration of possible operating scenarios [Conti et al., 2018].
One of the pioneer investigations in this area was presented in 2008 by Kleinstreuer et al. [Kleinstreuer et al., 2008], who discussed a finite element analysis (FEA) of tubular, diamond-shaped stent grafts under representative cyclic loading for abdominal aortic aneurysm (AAA) repair. In 2012 De Bock et al. [De Bock et al., 2012] experimentally validated the use of structural FEA with virtual deployment of a bifurcated stent graft into a patient-specific abdominal aortic model.
Perrin et al. in 2016 simulated numerically endograft deployment inside two different patient-specific tortuous arterial models of abdominal aneurysm [Perrin et al., 2016]. The results of the study group proved the efficacy of FEA to predict endovascular repair even in very tortuous arteries which are usually more prone to complications.

Finite element investigations regarding the feasibility of TEVAR to treat complex cases are few in literature.
Recently, Romarowski et al. [Romarowski et al., 2018] simulated numerically the deployment of custom made endoprostheses into the ascending aorta evaluating the feasibility of endovascular procedure with different types of stentgrafts.
In 2019, Meng and colleagues [Meng et al., 2019] investigated the mechanical behavior of two types of stentgrafts and its relationship with complication development after TEVAR for type B aortic dissection.

Aim of our work is to investigate in a patient-specific case the deployment sequence of two partially overlapped endografts and to evaluate wall apposition and conformation in a challenging tortuous descending thoracic aorta. Primary outcome of the study is the comparison between predicted endografts expansion and real endograft apposition to the wall detected by post-operative CTA images. Then, following a specific request from the surgeons who wonder to know if is possible to avoid complications with a better planning we decided to perform an additional simulation by changing the deployment sequence between proximal and distal endograft. Secondary outcome of the study is therefore the comparison of predicted endografts apposition to the aortic wall between the two different simulations.[5]

## 7.1 Finite element analysis

Finite element analysis coupled with engineering and design began in the 1960s with its first major applications in the field of aerospace engineering [Clough, 1990].
Finite elements methods (FEM) are numerical methods adopted to approximate solutions of mathematical problems when the related analytical solutions cannot be obtained.
Many engineering phenomena and mechanical systems can be expressed by governing equations and boundary conditions. FEM relies on a discrete representation of a physical continuum. In particular, a discretization strategy consists in the subdivision of the whole domain into a generally large number of non-overlapping subdomains (elements). Such elements are interconnected at nodes common to two or more elements and all together they should cover the entire domain as accurately as possible. The set of nodes and elements constitute the mesh. Each of these elements is represented by a set of nodal equations. The response of each element is expressed in terms of a finite number of degrees of freedom, characterized as the value of an unknown function at a set of nodal points. The overall response of the mathematical model results therefore in an approximation of the response of the discrete model obtained by assembling all elements of the mesh.
In mechanical problems, the nodal displacements are the fundamental variables that the solver

[5]This chapter is based on:
Finotello A, Spinella G, Conti M, Pane B, Auricchio F, Palombo D. Toward the use of patient-specific structural simulations of endovascular repair in the clinical practice. $67^{th}$ Proceeding of the International congress of the European Society of Cardiovascular and Endovascular Surgery (April 2018, Strasbourg).

has to calculate. Subsequently, after solution of the global equation system, strain and stress values of each element can be extracted.
Implicit and Explicit are two different approaches that can be used to solve the finite element problem. Implicit formulation requires to solve simultaneously the equilibrium equations and the equations system needs to be solved at the end of each time increment. In contrast to implicit formulation, the explicit approach does not require to solve simultaneously an equation system but nodal displacement is approximated to the next increment using acceleration of the current time-step. Selection of the solution method depends on the specifics of the problem. On one hand, the implicit method is ideal when the response of the dynamic system depends mainly upon lower frequencies. On the other hand, explicit formulation is advantageous to treat high frequency parts and traveling waves. There are, however, certain static or quasi-static problems that can be simulated well with both methods. Several reasons can guide the choice between explicit and implicit approach. Implicit formulation could provide results of high accuracy even if an high number of iterations and an excessive computation cost could be detected. From an opposing point of view, when the number of degrees of freedom is high the explicit method could be the only alternative to obtain results in a relatively short time.
In our specific case, the FEA of aortic endografting essentially transforms the unknowns from the continuum (e.g. the model of the aorta and of the endograft) into equations of discrete nodal quantities. Under the assumption that certain numerical requirements and standards of practice are satisfied, the solution obtained from finite element analysis could estimate the physical solution of the problem under investigation (e.g. the real endovascular procedure). Quantitative characterization of the anatomy, structure and material properties forms the foundation for FEA and the reliability of the results obtained depends on the accuracy of the characterization and translation of such parameters into the FE model. Important parameters include:

- aorta and device geometry;
- tissue and device mechanical properties;
- boundary conditions created by the interaction of the anatomy and the implanted devices.

In the following sections all these prerequisites, needed to set up a proper finite element model are discussed in more detail.
The commercial finite element solver Abaqus CAE 6.14 ®by Dassault Systemes (Providence, RI, USA) is used to perform all the simulations.

## 7.2 Patient clinical history

In this work we considered a 78 year old patient with aneurysm in the descending thoracic aorta. TEVAR was performed using two Zenith Cook stentgrafts (Cook Inc, Bloomington,

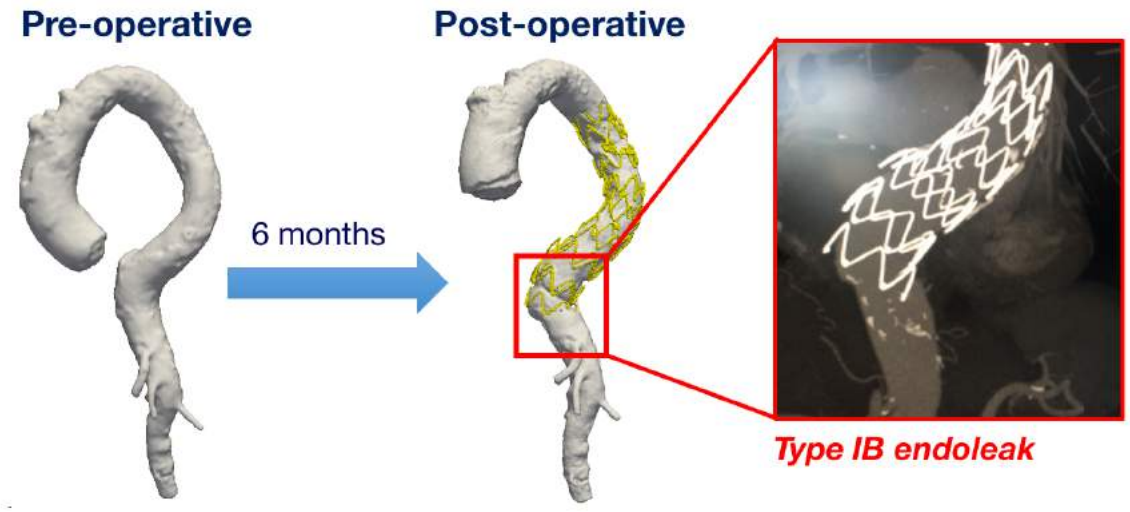


Figure 7.1: Pre-operative and post-operative aortic surfaces reconstructed from CTA images. Six-months after endovascular procedure routine CTA showed type IB endoleak (red box).

Ind) sized 36-161 (proximal endograft) and 36-113 (distal endograft). The intervention was successfully performed without intra-operative complications. The patient was discharged on the sixth post-operative day under antiplatelet therapy. Six months after intervention, routine CTA examination showed type IB endoleak (see Figure 7.1).

## 7.3 Methods

The analysis method consists of three main steps: pre-processing, simulation of endograft deployment, and post-processing, following [Auricchio et al., 2013].

### 7.3.1 Pre-processing

The first step of the simulation setup involves the segmentation of pre-operative medical images acquired by CTA scans with the VMTK software (level set gradient based with colliding fronts initialization) as described in Chapter 2 to retrieve a 3D vascular model. In order to reduce analysis computation time, the surface is clipped and then further elaborated with surface smoothing and remeshing operations (see Figure 7.2). A triangular mesh (R3D3 elements) is assigned to the aortic surface and rigid material properties are adopted. Vessel centerline is then computed by means of VMTK script (see Chapter ).
As mentioned before, for this patient, two Zenith Alpha Low Profile endovascular prostheses

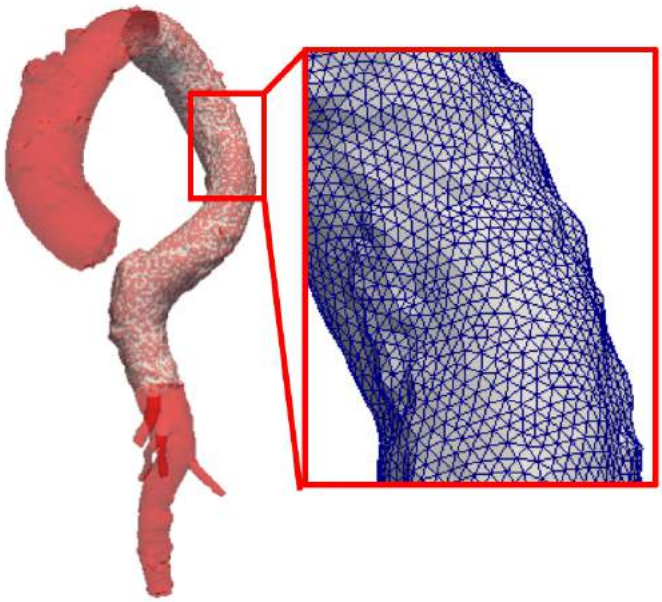

Figure 7.2: Reconstruction of the patient aorta (red), clip of the surface (white) and zoom on the adopted triangular mesh.

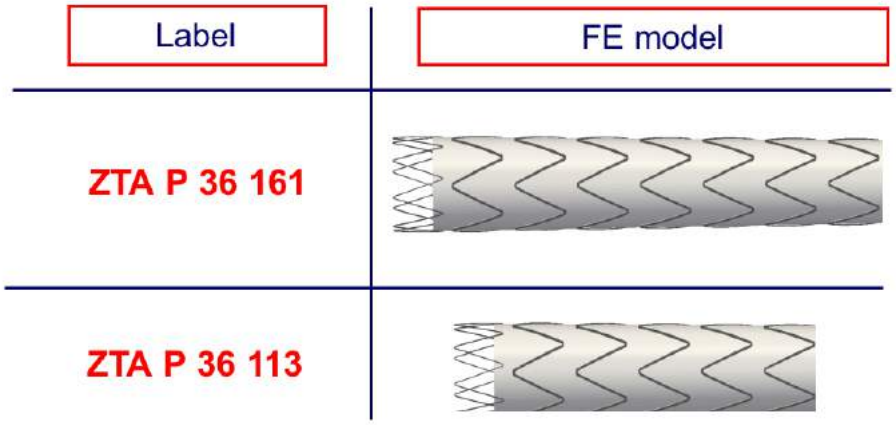


Figure 7.3: Two different endograft models were created following real samples measurements.

have been implanted by the surgeons. Accurate models of the prostheses based on the real prosthesis samples are reconstructed by means of Abaqus CAE software and a suitable mesh for structural FEA is defined. Reconstructed endograft models are depicted in Figure 7.3. The metallic grafts are then meshed with 8-noded solid hexahedral elements (C3D8R) using the software Abaqus CAE and assigned NiTiNOL properties with constitutive law parameters as described in Table 7.1. Triangular membrane elements (M3D3) are adopted to model the fabric coverage. PTFE material properties are defined as described in Kleinstreuer et al. [Kleinstreuer et al., 2008]: Young's modulus 55.2 $MPa$, Poisson ratio 0.46, plasticity Yield stress 6.6 $MPa$. A detail of endograft mesh is given in Figure 7.4.

### 7.3.2 Simulation methodology of endograft deployment

The input file for structural FEA has been written by means of in-house developed Matlab scripts (contribution by M. Conti, University of Pavia). Briefly, while running the code, user is asked to select on the vessel centerline the endograft proximal landing point. Then, the endograft model is imported and a rigid cylindrical surface resembling catheter is built around the endograft allowing for endograft crimping. Endograft virtual deployment is simulated in two steps. First, the endograft is crimped by the catheter and curved from a straight position to the vessel's centerline. Then, once the endograft is positioned, a uniform enlargement of the catheter surface along its length is performed to allow endograft self-expansion inside the vessel model. Figure 7.5 illustrates the different steps of endograft virtual crimping and deployment.

| NiTiNOL material parameters | |
|---|---|
| Austenite Young's modulus | 51700 $MPa$ |
| Austenite Poisson's Ratio | 0.3 |
| Martensite Young's modulus | 47800 $MPa$ |
| Martensite Poisson's Ratio | 0.3 |
| Transformation strain | 0.063 |
| Loading | 6.527 |
| Loading start of transformation stress | 600 $MPa$ |
| Loading end of transformation stress | 670 $MPa$ |
| Temperature | 37 °C |
| Unloading | 6.527 |
| Unloading start of transformation stress | 288 $MPa$ |
| Unloading end of transformation stress | 254 $MPa$ |
| Start of transformation stress (loading in compression) | 900 $MPa$ |
| Volumetric transformation strain | 0.063 |

Table 7.1: Fourteen parameters are used to accurately reproduce the NiTiNOL behavior.

Contact is defined between the endograft surface and the inner surface of the catheter and between the endograft surface and the inner surface of the aorta; a self-contact formulation is used for the endograft itself. The entire procedure was performed in seven analysis steps: six steps have a duration of 0.005 s each and account for gradual stent crimping and bending; the last step has a duration of 0.035 s to allow endograft self-deployment.

In the clinical case we examined, two partially overlapped endografts were deployed. A proximal endograft has been deployed, followed by a distal one partially overlapped to the first one. Therefore, the Matlab procedure is repeated to implant a second endograft inside the first one; thus creating a region of partial overlapping. During the re-expansion step, contact between the stent and the vessel and the stent with the previously deployed stent is activated. A semi-automatic mass-scaling strategy is used to speed up the analysis. During the entire simulation, kinetic energy is monitored to ensure that the ratio of kinetic energy to internal energy remains less than 10%. In the following of the present Chapter we will refer to this analysis as **Test A**.

As discussed before, to investigate if the change of deployment sequence between proximal and distal endograft could influence the procedural outcome, we performed an additional analysis by changing the order of deployment of the proximal and distal endograft (**Test B**). The simulation outcomes of the two different tests are then compared.

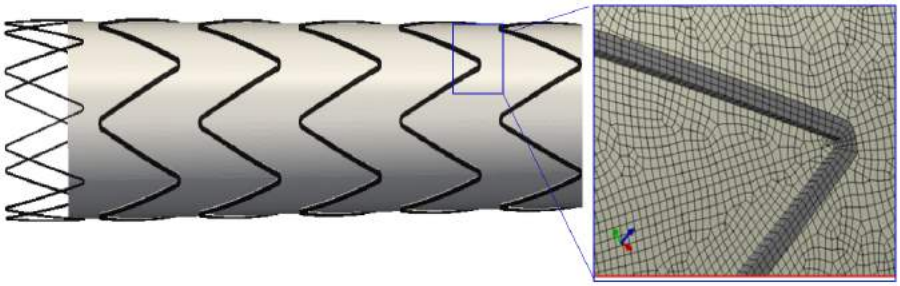

Figure 7.4: Detail of endograft mesh. C3D8R elements representing the struts are merged with M3D3 membrane elements representing the fabric.

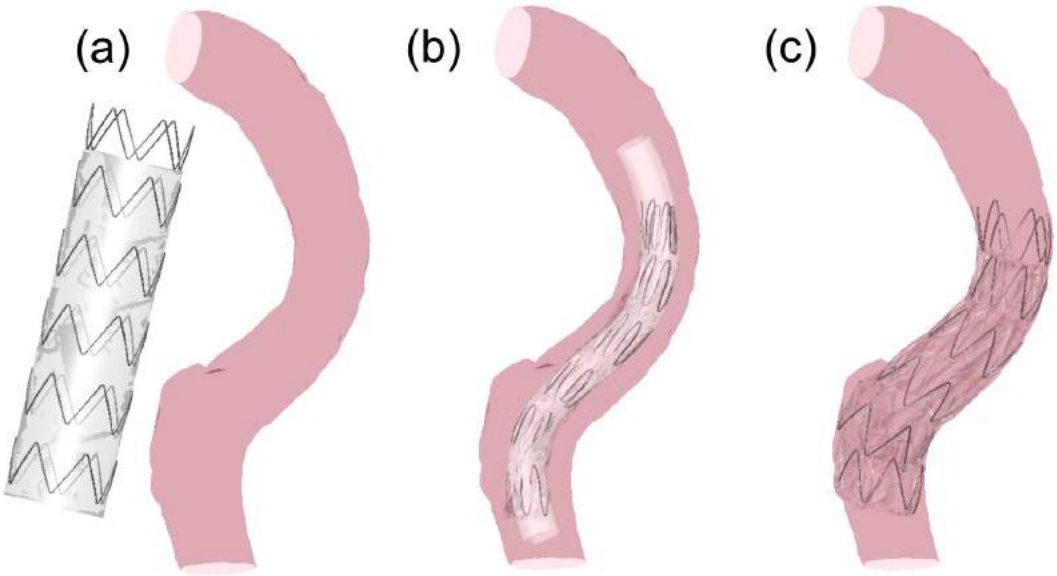


Figure 7.5: Simulation steps of endograft implantation: (a) starting configuration; (b) endograft crimping and bending inside the catheter; (c) stent self-expansion against the aortic wall.

### 7.3.3 Post-processing

After deployment simulation, the prediction of Test A (i.e. endografts deployment order as in the reality) is compared to the stentgrafts position assumed on post-operative CTA scan.

VMTK software is used to extract 3D representations of the post-operative vessel surface and of the stentgrafts surface. A qualitative assessment of the results is achieved by registering the post-operative deformed stent surface coming from the simulation to the real reconstructed one.
In addition, we compared the outcomes of two different deployment sequences (Test A *vs* Test B) to verify if a better apposition to the aortic wall could be obtained. The contours of the endograft and of the aortic wall surfaces taken on sections perpendicular to the vessel centerline to assess the proximity of endograft to the vessel wall. Cross-sections were taken for both the models at 2 mm, and 1 mm, and 0.5 mm along the centerline before the end of the simulated distal endograft. ImageJ open source software was adopted to quantify the area of mismatch between the simulated stentgrafts and the vessel surface.

## 7.4 Results

Two different simulations are performed. Abaqus/Explicit has been adopted as finite element solver. All the simulations run across 8 CPUs, in double precision, on a dedicated server (Intel Xeon E5-4620 2.20 GHz) and takes about 8 hours to complete.
Simulation A has been performed by taking into account the same deployment sequence as in the reality. First step involved the deployment of the proximal device and second step the deployment of the distal one. The predicted positions of the endografts are compared with the real post-operative outcome extracted from post-operative CTA. Simulation outcomes show a correct apposition along all the stent surface, with exception to the distal landing zone, where a mismatch between the surface of the distal deployed stent and the aorta has been recorded (see Figure 7.6). Such malapposition could be considered predictive of type IB endoleak development.

For test B, the first step involved the deployment of the distal device and second step the deployment of the proximal one partially overlapped to the first. As depicted in Figure 7.7, the two different simulation outcomes are then compared to evaluate device apposition to the wall in correspondence of the distal landing zone. For each model, three slices perpendicular to the centerline are taken to quantify the mismatch area between the simulated stentgraft and the aortic wall in the distal landing zone. Mean value is then extracted. A mean mismatch area of 73.2 $mm^2$ is obtained for test A compared to 40.88 $mm^2$ computed for test B. Therefore, we suppose that, in this latter case, the patient would be less prone to endoleak.

## 7.5 Discussion

Nowadays, the finite element analysis method is a widely accepted method which can provide ambitious predictive information during the surgeon's decision-making process, and previous

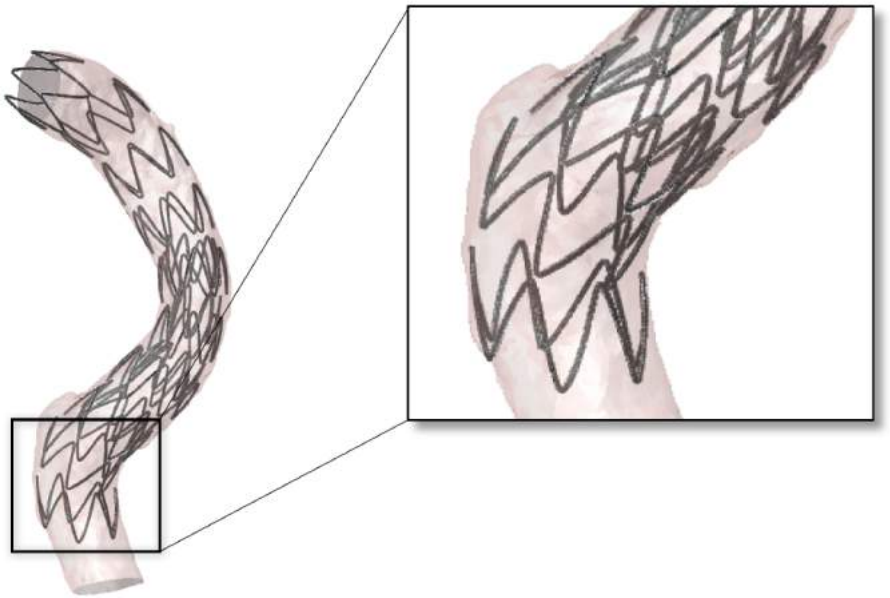

Figure 7.6: Result of deployment simulation. The zoom shows a bad apposition of the endograft in correspondence of the distal landing zone which could be predictive of type IB endoleak development as observed in the reality.

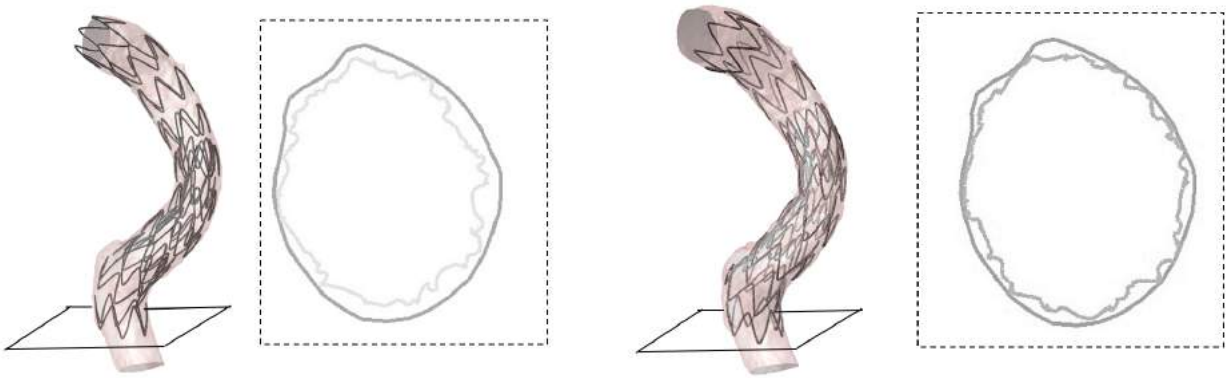

Figure 7.7: Test A (left) *vs* Test B (right). As depicted a better apposition to the wall is obtained for case B.

studies have already correlated the usefulness of this method in various scenarios requiring virtual stent evaluation [Arokiaraj et al., 2014].

In this work we investigated the deployment of two partially overlapped endovascular devices inside a patient-specific model of descending thoracic aorta. The clinical case was chosen for the tortuous geometry and for the development of complication during follow-up.

Simulation outcomes were compared to post-operative CTA images showing a good adherence to the reality. In particular, bad apposition to the aortic wall in correspondence of the distal landing zone could be predictive of complication development.
Moreover, as shown in Figure 7.7, we demonstrated that, by changing the deployment sequence (distal device deployed first), a better apposition of the simulated stent-graft in the distal landing zone could be obtained.
In conclusion, this study demonstrated that patient-specific computational simulations could provide additional predictive information about the behavior of the devices, both during deployment and after expansion, driving the surgeons during the decision-making process. In the future, additional simulations on a larger dataset of clinical cases should be performed.

# Chapter 8

# *In-vivo* morphological changes of the femoropopliteal artery due to limb flexion after endovascular treatment of popliteal aneurysms

If compared with aortic aneurysms, popliteal aneurysms are relatively uncommon. However, recent studies demonstrated an association between the presence of aortic aneurysm and the development of popliteal aneurysms. Although endovascular treatment could be recommended specially in high-risk patients, its outcomes are still debated and there is an increased interest in understanding the causes inducing to the mechanical failure of the implanted devices. The hostile biomechanical conditions of the popliteal segment due to the hip/joint kinematics surely plays an important role in the occurrence of these drawbacks.
On this basis, in this chapter we will present a study regarding the evaluation of popliteal artery device performance. In particular, we will assess the capability of the device to avoid localized kinks and to keep the lumen patency during knee flexion by means of quantitative medical image analysis.[6]

## 8.1 Introduction

Popliteal artery aneurysms (PAA) are the most frequently encountered peripheral aneurysms [Ouriel, 1995]. In elective cases, open repair or endovascular treatment are often used when the aneurysm reaches 2 cm in diameter [Pulli et al., 2013].

[6]Spinella G, Finotello A, Pane B, Salsano G, Mambrini S, Kamenskiy A, Gazzola V, Cittadini G, Auricchio F, Palombo D, and Conti M. *In-vivo* morphological changes of the femoropopliteal artery due to limb flexion after endovascular treatment of popliteal aneurysms. Journal of Endovascular Therapy; accepted for publication.
The authors would acknowledge Ana Jounea (University of Pavia) for her support in the analysis procedure.

Results of the endovascular treatment were initially disappointing, likely due to the materials used in the first generation of devices [Gerasimidis et al., 2003], and while it continues to demonstrate lower patency rates compared with open repair using prosthetic materials or the autologous vein [Wrede et al., 2018], endovascular PAA repair is now indicated in selected cases [Lovegrove et al., 2008]. In particular, it is often used in the absence of arterial tortuosity and off-target area dilations, and when treating patients with at least two run-off vessels, and proximal and distal stent-graft landing zones of at least 15 mm [Leake et al., 2017].
However, clinical outcomes even in these selected patients are far from perfect, and treatment failures are often attributed to the severe repetitive deformations experienced by the femoropopliteal artery during limb flexion. These deformations can lead to kinking and compression of the endovascular device, contributing to thrombosis, stent fracture [Tielliu et al., 2010], and ultimately resulting in treatment failure [Tielliu et al., 2005]. These considerations call for a quantification of the *in-vivo* behavior of the femoral-popliteal artery (FPA) during limb flexion after endovascular aneurysm repair.
Until recently, only a few studies investigated FPA kinematics in healthy patients [Choi and Cheng 2016; Diehm et al. 2011] or studied occlusive peripheral artery disease (PAD) treatment *ex-vivo* in human cadavers [MacTaggart et al. 2018; MacTaggart et al. 2018; Smouse et al. 2005] or *in-vivo* using 2D angiographic images [Ganguly et al. 2011; Gökgöl et al. 2017]. Recently, Conti et al. [Conti et al., 2017] used 3D CTA to measure *in-vivo* femoro-popliteal artery deformations during limb flexion, and have used these data in a patient-specific stenting simulation. Consequently, to the best of our knowledge, the in-vivo assessment of post-stenting PAA deformations due to limb flexion has not yet been performed.
Given this motivation, the present study aims at evaluating the morphological changes of the femoro-popliteal axis due to limb flexion in patients with endovascularly treated PAA using a standardized protocol for CTA acquisition with both straight and bent limb positions.

## 8.2 Methods

Seven patients who underwent endovascular treatment for PAA at our center between January 2013 and December 2017 were selected for the study. Signed informed consent was obtained from all patients and all procedures were performed in accordance with the Declaration of Helsinki and submitted to local institutional medical ethics committee.
Patient selection was based on the following criteria: patients of both genders, with age between 50 and 85 years, and no contraindications to CTA examinations. Exclusion criteria were previous peripheral surgical or endovascular procedures, and inability to give signed informed consent. Patients who developed stent-graft occlusions during the follow-up were excluded as well.

### 8.2.1 Endovascular treatment

PAA endovascular treatment with covered self-expandable stent-graft (Viabahn, Gore, Flagstaff, AZ) was planned on the basis of pre-operative CTA. Patients were deemed eligible for the endovascular treatment if their proximal and distal landing zones were least 15 mm, and the artery was relatively straight and free from stenosis or off-target dilations. In all cases, at least two run-off vessels were present. Stent-graft was oversized 10% with respect to the proximal landing zone diameter. No oversizing was used for the distal landing zone. Due to tapering of the artery distally, we have often placed two or three stent-grafts to avoid excessive oversizing, and the length of these stent-grafts was chosen in accordance with the length necessary to exclude the aneurysm. All patients were treated under spinal anesthesia. Surgical exposure of the proximal superficial femoral artery was performed, and a 10-11 Fr introducer was placed under systemic heparinization. Angiographic images were acquired, and a stiff guide-wire (Supracore; Guidant, Santa Clara, CA, USA) was placed in the tibial or below-knee arteries. The endografts were then deployed, and the angiography was repeated to ensure correct stent placement. Patients were discharged on dual antiplatelet therapy (Clopidogrel 75 and Cardioaspirin 100 mg/die).

### 8.2.2 Imaging acquisition protocol

During the follow-up, one contrast-enhanced CTA of the lower limbs was acquired for each patient in addition to the routine eco color-doppler imaging. During this CTA examination, two scans were performed few minutes apart. During the first scan, the treated lower limb was placed in the standardized 90°position (bent-leg configuration) using a dedicated foam-coated leg support (see 8.1A), while the contralateral limb remained straight. Following bent-limb imaging, the treated limb was placed in the 180°position (straight-leg configuration) to acquire the second scan (see Figure 8.1B). All CTA images were acquired with the same 64 multidetector-row CTA (General Electric Optima 660). The adopted scan parameters were: thickness, 0.625 mm; increment, 0.625 mm; collimation, 64x0.625; pitch, 0.915; rotation time, 0.7 s; field of view, 35 cm; matrix, 512x512 pixel.
In each patient, an 18-gauge intravenous catheter was placed in an antecubital vein in the upper limb, and contrast material was injected using a double-syringe injector. The start trigger of scanning was individually obtained for each patient by using "smart prep" technique, with a trigger level of 100 Hounsfield Units and a delay time of 5 s in order to obtain an optimal intraluminal contrast enhancement. The triggering area was manually placed at aortic hiatus. The first scan was obtained in a single breath-hold from the aortic hiatus to pedidial artery with the affected lower limb at 90°position. The second scan was obtained from the common femoral artery to pedidial artery with the affected lower limb at 18°position.
The study group was examined using a low-dose-radiation protocol, with 100 keV and automated tube current modulation. In all patients, low contrast material volume (50-70 ml, Iomeron 400 or Iopamiro 370) was administered, with a flow rate of 4ml/s followed by saline

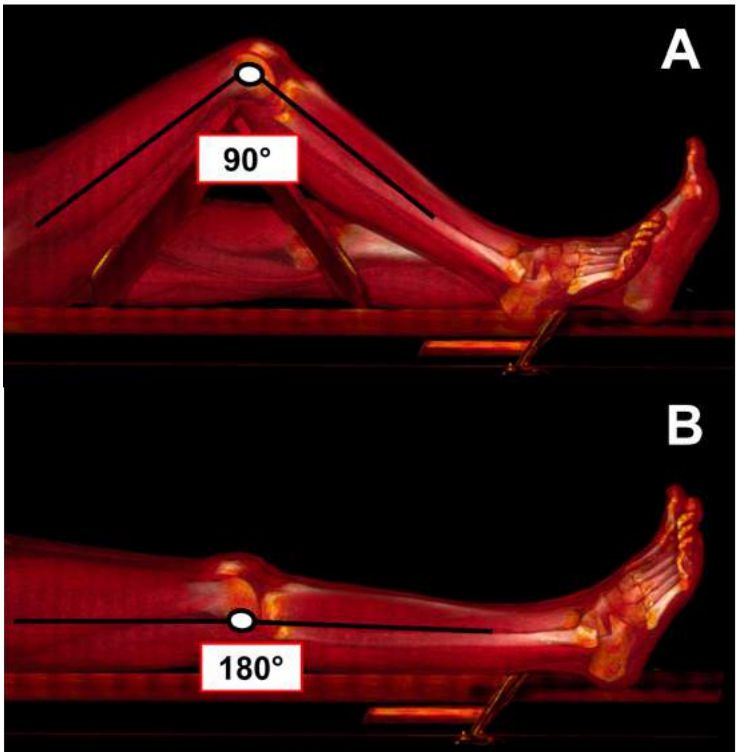


Figure 8.1: CTA acquisition in standardized (A) bent-leg and (B) straight-leg positions.

flushing (30 ml; flow rate, 4ml/s).

### 8.2.3 Image processing

Post-operative CTA images were anonymized and transferred to a workstation for image processing. Segmentation of the FPA from the femoral artery bifurcation to the popliteal artery bifurcation, leg bones, calcifications of the arterial wall (if present), and the implanted stent-graft, was performed using the open source library VMTK following the procedures illustrated in Section 2.7.4. As previously outlined, this tool allows to create an automated framework, consisting of a pipeline of instructions, that minimizes users' interaction by limiting it to the segmentation phase alone. For each patient, rigid-registration of bent leg structures on their corresponding straight counterparts was automatically performed by means of the Iterative Closest Point algorithm [Besl and McKay, 1992] implemented in VMTK.
Reconstruction of the vessel centerline was performed automatically [Antiga et al., 2003] followed by resampling and smoothing operations using the moving average filter. The femoral-popliteal axis was then divided into three zones (see Figure 8.2) spanning the distance between

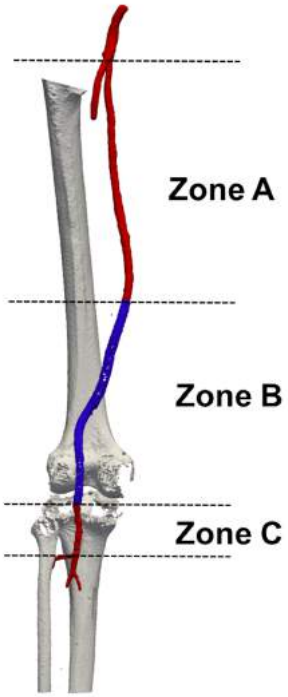


Figure 8.2: Subdivision of the FPA into three zones: (A) between the origin of the superficial femoral artery and the proximal end of the covered stent; (B) from the proximal to the distal end of the stent-graft; and (C) from the distal end of the covered stent to the origin of the anterior tibial artery. Stent-graft is highlighted in blue while arterial lumen in red.

the origin of the superficial femoral artery and the proximal end of the covered stent (zone A), from the proximal to the distal end of the stent-grafted segment (zone B), and from the distal end of the covered stent to the origin of the anterior tibial artery (zone C). Since all stent-grafts were placed in the popliteal artery, in many subjects zone C was the shortest of all three zones and constituted on average only 4.5 cm in length.

For each segment, the following parameters were automatically computed by means of VMTK scripts: centerline length, centerline point-wise curvature, centerline global tortuosity, diameter, and eccentricity of each section along the vessel. For each computed parameter, comparisons were performed between straight-leg and bent-leg configurations.
A foreshortening Index (FI) was defined based on centerline length as:

$$FI = \frac{length_{FL} - length_{SL}}{length_{SL}} * 100 \tag{8.1}$$

to quantify the difference in length between the two limb flexion configurations. When two or more stent-grafts overlapped, the length of the overlapping zone was measured as well.

Starting from the vessel centerline, equally-spaced planes perpendicular to the centerline were computed, and diameter and eccentricity measurements were taken on each transverse section. Maximum cross-sectional diameter was measured to detect zones of partial stenosis/thrombosis. Then, for each of the three zones (A, B, and C) mean and minimum values were extracted. Sections eccentricity was calculated to assess flexion-induced cross-sectional pinching defined for each cross-section as: $E = d/D$ where $d$ and $D$ are the minimum and maximum diameter of the artery, respectively. Absolute mean and minimum values for each zone (A, B, and C) were then extracted.
Tortuosity index was measured as a global parameter, describing the overall shape of the vessel. Curvature was computed for each point of the centerline representing the local behavior of the centerline. For both straight and bent limb configurations, tortuosity index was defined as: $T = L/ED - 1$, where $L$ represents the centerline length, and $ED$ is the shortest distance between the two centerline endpoints. This parameter quantifies the fractional increase in length of a tortuous vessel when compared to a perfectly straight path. Curvature of the vessel centerline was defined for each point of the centerline as the inverse of the radius of the osculating circle, i.e., the circle that approximates the curve at a given point. An automatic script implemented in VMTK was adopted to compute pointwise curvature values along the centerline [Piccinelli et al., 2009], and the maximum value of curvature was then calculated.

### 8.2.4 Statistical analysis

Categorical variables were expressed as absolute frequencies and percentages whereas continuous variables were assessed as means and standard deviations. All statistical analysis was performed using the JMP 13.0 (SAS Institute Inc. Cary, NC, USA) software. Significance of differences between the bent and straight limb configurations was analyzed using Paired-samples t-tests. P values less than 0.05 were considered statistically significant.
Two independent skilled observers performed segmentation of CTA images, followed by centerline computation and extraction of diameter and curvature measurements. One observer performed segmentation twice allowing for inter-observer and intra-observer variability analyses using the intraclass correlation coefficient (ICC). Results were presented with the 95% confidence interval (CI). After computing the centerlines, automatic extraction of diameters, eccentricity, tortuosity and mean curvature was performed by means of a script implemented in the VMTK software.

## 8.3 Results

Patients' demographics and comorbidities are listed in Table 8.1. Mean age was 67.83 years (range: 52-88 years).
Proximal landing zone of the stent-graft was either in the superficial femoral or proximal popliteal artery, while distal landing zone was in the popliteal artery below the knee at an average 45.2 ± 35.6 mm distance from the origin of the anterior tibial artery. Mean CTA follow-up was 17.8 months (range: 1-57 months), and all scans were successfully segmented both in the straight and in the bent limb configurations. Since arteries were not heavily calcified, analysis of calcification was not performed.
Figure 8.3 illustrates the 3D reconstructions of all the patients.

| | |
|---|---|
| Numerosity | 7 |
| Age (mean ± std dev) | 67.83 ± 9.54 years |
| Male/ Female | 7/0 |
| Smoking | 3/7 |
| Hypertension | 7/7 |
| Diabetes | 3/7 |
| Chronic obstructive pulmonary disease | 4/7 |
| Ischemic cardiomyopathy | 5/7 |
| Chronic renal failure | 2/7 |
| American Society of Anesthesiologists Classification 1-2 | 2/7 |
| American Society of Anesthesiologists Classification 3-4 | 5/7 |

Table 8.1: Patients' characteristics.

Arterial diameters, eccentricity, length, tortuosity, and curvature for each of the three FPA segments A, B, and C in straight (SL) and bent (BL) limb configurations are reported in Tables 8.2, 8.3 and 8.4, respectively.

Segment A on average foreshortened 6% from 238.5±56.77 mm to 225.21±56.87 mm during limb flexion ($p=0.001$), and the curvature ($p=0.05$) and tortuosity ($p<0.05$) increased 15% and 67%, respectively. No significant changes in minimum or mean diameters or eccentricity between the straight and bent limb configurations were observed.

Stent-grafted segment B on average foreshortened 4%, from 236.36 mm to 226.08 mm with limb flexion ($p=0.001$), and when devices overlapped, the length of the overlapped segment decreased 9% due to limb flexion. Similar to segment A, limb flexion produced a significant increase in mean curvature (from 0.026 to 0.033 on average; $p=0.005$) and tortuosity (0.06 to 0.15 on average; $p<0.05$). The difference in mean and minimum diameter between the straight-leg and bent-leg positions was not statistically significant but in two patients we have observed localized zones of diameter reduction in the stent-grafted region in the bent-leg po-

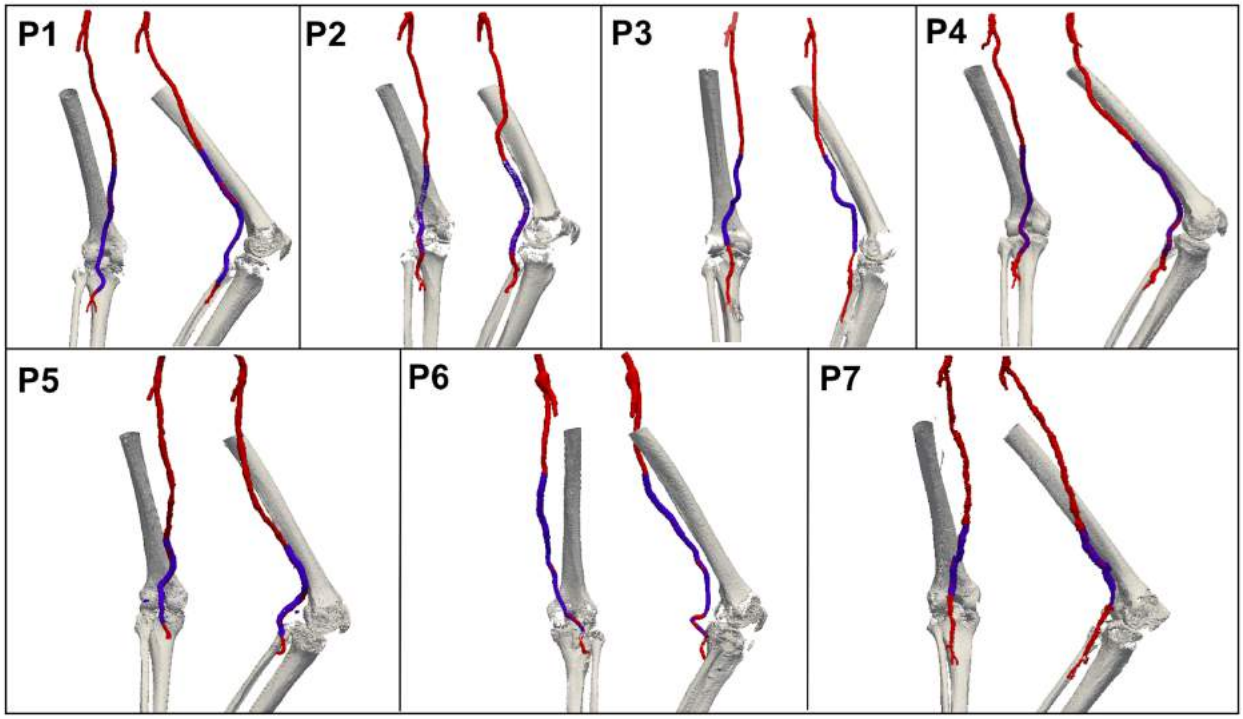


Figure 8.3: 3D reconstruction of femoro-popliteal artery (red), stent-graft (blue) and bones (grey) in seven patients recruited in our study. Two different views are presented for each patient.

| | Straight-leg | Flexed-leg |
|---|---|---|
| Mean diameter [mm] | 8.25 ± 1.10 | 8.15 ± 0.90 |
| Min diameter [mm] | 7.41 ± 1.35 | 7.30 ± 0.98 |
| Eccentricity [-] | 0.89 ± 0.01 | 0.9 ± 0.01 |
| Min eccentricity [-] | 0.75 ±0.06 | 0.73±0.05 |
| Length [mm] | 238.50 ± 56.77 | 225.21 ± 56.87 |
| Tortuosity [-] | 0.03 ± 0.006 | 0.05 ± 0.02 |
| Mean curvature [1/mm] | 0.027 ± 0.007 | 0.031 ± 0.005 |

Table 8.2: Measurements in straight-leg and flexed-leg positions in zone A.

| | Straight-leg | Flexed-leg |
|---|---|---|
| Mean diameter [mm] | 7.42 ± 1.08 | 7.12 ± 0.94 |
| Min diameter [mm] | 6.08 ± 1.81 | 5.89 ± 1.70 |
| Eccentricity [-] | 0.9 ± 0.02 | 0.89 ± 0.02 |
| Min eccentricity [-] | 0.75 ± 0.08 | 0.70 ± 0.08 |
| Length [mm] | 235.36 ± 74.24 | 226.08 ± 72.77 |
| Tortuosity [-] | 0.06 ± 0.03 | 0.15 ± 0.09 |
| Mean curvature [1/mm] | 0.026 ± 0.005 | 0.033 ± 0.006 |

Table 8.3: Measurements in straight-leg and flexed-leg positions in zone B (stented zone).

sition as illustrated in Figure 8.4.

Average eccentricity was not affected by leg flexion, and minimum eccentricity decreased from 0.74±0.08 to 0.70±0.08 but the statistical significance was not reached (p=0.9). Most severe changes in minimum eccentricity were observed in two patients (from 0.72 to 0.59 in one patient and from 0.84 to 0.67 in the second patient) and these results are illustrated in Figure 8.5. Segment C was 5-fold shorter than both segments A and B. No significant differences in length, diameter or eccentricity with limb flexion were detected in segment C.
Conversely, in zone C no significant differences for the parameters under investigation between SL and FL were found.

| | Straight-leg | Flexed-leg |
|---|---|---|
| Mean diameter [mm] | 6.65 ± 0.87 | 6.60 ± 1.01 |
| Min diameter [mm] | 6.64 ±1.66 | 6.50 ±1.78 |
| Eccentricity [-] | 0.88 ± 0.04 | 0.89 ± 0.05 |
| Min eccentricity [-] | 0.76 ± 0.07 | 0.70 ± 0.13 |
| Length [mm] | 45.20 ± 35.61 | 43.35 ± 30.99 |
| Tortuosity [-] | 0.027 ± 0.017 | 0.031 ± 0.01 |
| Mean curvature [1/mm] | 0.032 ± 0.013 | 0.063 ± 0.034 |

Table 8.4: Measurements in straight-leg and flexed-leg positions in zone C.

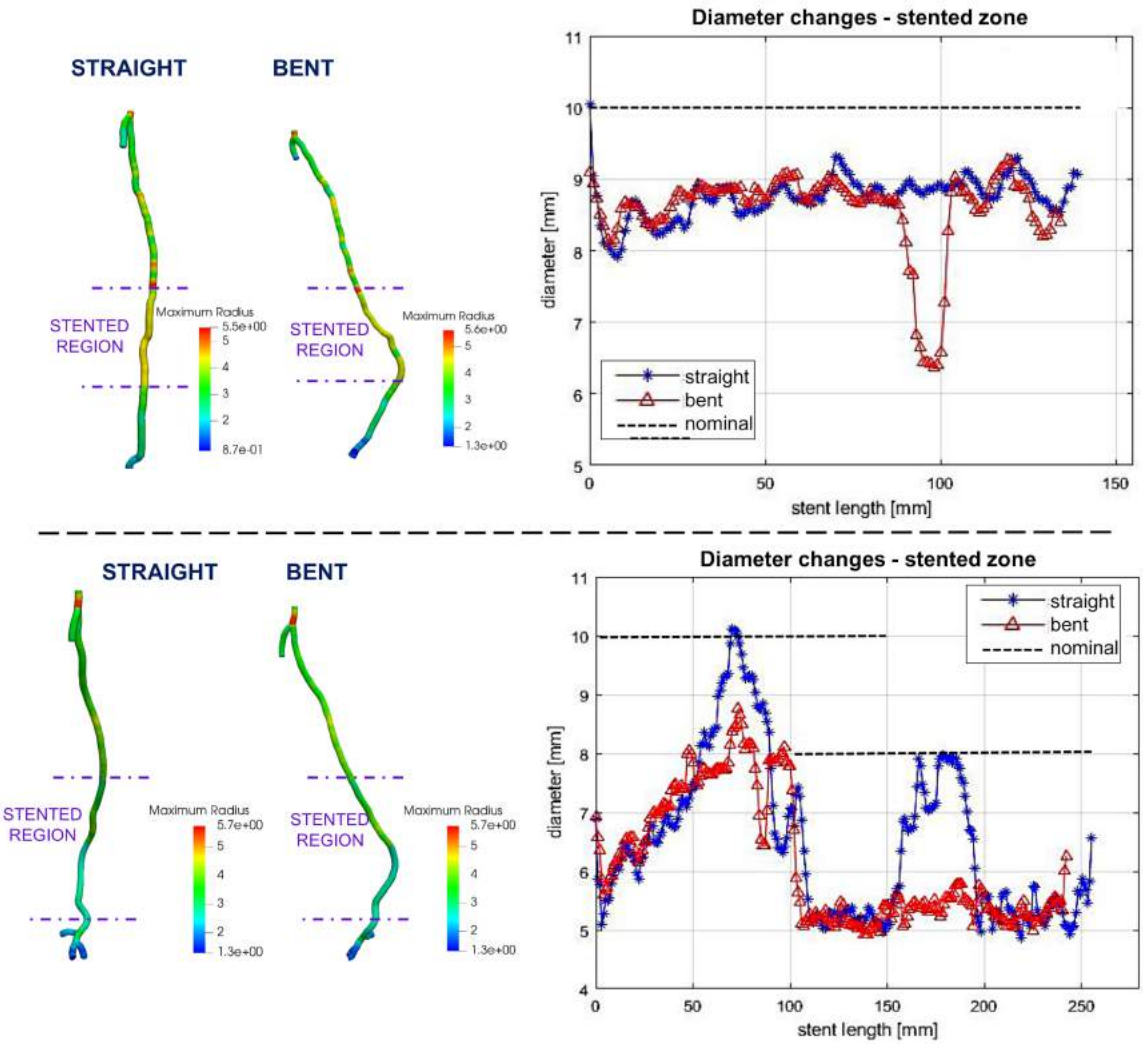


Figure 8.4: Diameter reduction in the stent-grafted segment due to limb flexion in two patients. Left: Contour plot depicting changes in arterial diameter along the length of the segmented FPA. Right: Change in FPA diameter along the length of the stent-grafted zone in straight (blue) and bent (red) positions. Nominal stent-graft diameters are depicted with black dashed lines; two partially overlapping endografts are shown for the second patient.

### 8.3.1 Intraobserver and interobserver reproducibility

Intraobserver and interobserver reproducibility were computed by ICC. Intraobserver ICC resulted in 0.98 (95% CI 0.97 to 1.00), 0.98 (95% CI 0.97 to 0.99) and 0.97 (95% CI 0.96 to 0.98) for the difference in centerline length corresponding to zones A, B, and C, respectively.

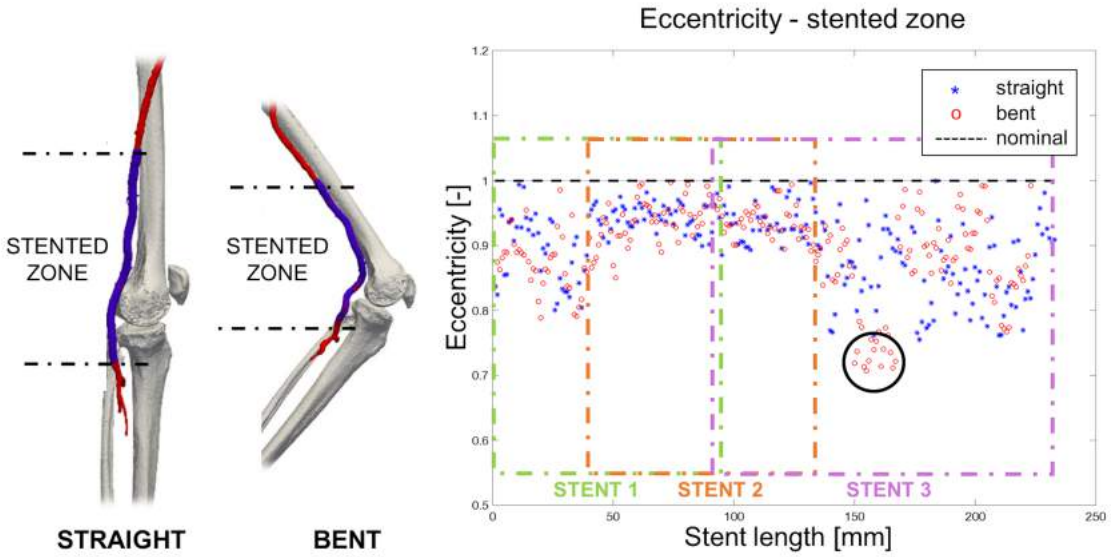


Figure 8.5: On the left, 3D reconstruction of bones and FPA in both straight and bent limb configurations pertaining to one representative patient. On the right, the graph demonstrates change in eccentricity along the length of the stent-grafted segment in straight and bent positions. Black dashed line denotes eccentricity of an ideal circular section. Black circle highlights the zone where eccentricity reduction was observed during limb flexion. Colored boxes refer to different stents.

Interobserver analysis showed an ICC index of 0.98 (95% CI 0.98 to 0.99), 0.95 (95% CI 0.94 to 0.97) and 0.94 (95% CI 0.94 to 0.95). These results demonstrated excellent intraobserver agreement and good interobserver agreement in detecting differences in centerline length between straight and bent limb configurations.

## 8.4 Discussion

Current study focused on the evaluation of the morphological changes in the femoro-popliteal axis due to limb flexion in patients undergoing PAA repair with a Viabahn stent-graft. Prior *in-vivo* studies investigating deformations on the FPA segments during limb flexion mainly utilized young healthy volunteers, which did not allow the assessment of age and arterial pathology on vessel kinematics [Choi and Cheng 2016; Diehm et al. 2011]. *Ex-vivo* studies in older cadavers [Smouse et al., 2005] have been reported as well, but the absence of active muscle contraction may potentially affect limb flexion-induced deformations [MacTaggart et al.,

2018]. Present study investigated *in-vivo* PAA repair which to the best of our knowledge has not yet been evaluated in the context of limb flexion.

In this study we have defined a novel protocol for CTA acquisition with both bent- and straight-leg positions, which optimizes the amount of injected contrast bolus. The latter is a critical factor because it allows to achieve an adequate concentration of contrast medium in the lumen of the vessel from the aorta to dorsal pedis artery [Fleischmann et al., 2000]. In general, 100-130 ml of contrast medium is recommended to obtain a good quality CTA, but several reports suggest lower contrast concentrations [Baxa et al., 2014]. In our study we used a double scan low-dose-radiation and low contrast material volume protocol to analyze peripheral arteries of the lower limbs in a standardized 90°and 180°positions, and were able to achieve excellent image quality. The protocol of obtaining a bent-limb CTA also allowed the assessment of arterial curvature and tortuosity which were previously reported as risk factors for arterial pathology in patients undergoing stenting [Tillich et al., 2001].

Our results demonstrate that proximal to the covered stents, arterial diameter, eccentricity, and mean centerline curvature of the FPA does not change significantly with limb flexion, but vessel foreshortens on average by 6%. These values are in line with previously reported findings by Choi and Cheng (8.8±4.4 %) [Choi and Cheng, 2016], Ansari et al. (4-6%) [Ansari et al., 2013], and Ní Ghriallais et al. (9.9±1.8%) [Ní Ghriallais et al., 2016] that have also analyzed long arterial segments, but are lower than segmental values reported by Poulson et al. et al. [Poulson et al., 2018] likely due to non-uniform distribution of FPA deformations along the artery length.

In the repaired segment, we found a reduction of 3.3% of the stent-graft mean diameter during limb flexion, but mean and minimum eccentricity did not change significantly suggesting that the Viabahn stent-graft generally remains circular during flexion of the limb. In some patients however we have detected localized zones of section eccentricity reduction which shows the tendency of the stent-graft to pinch in the flexed limb posture as also reported previously 13,27 [MacTaggart et al. 2018; Desyatova et al. 2018].

The stent-grafted segment foreshortened on average 4.3% during limb flexion, which is in line with previously reported data for the non-stented arteries reported by Ansari et al. [Ansari et al., 2013]. Using a heterogeneous group of patients with and without peripheral arterial disease, as well as human cadavers, Ansari et al. reported an axial shortening of 4-13.9% in the FPA depending on the axial position along the vessel. Comparison of our data to these results suggest that the implanted stent-grafts were able to maintain these baseline values of physiological foreshortening. The capability of Viabahn of avoiding foreshortening has been also confirmed by MacTaggart et al. [MacTaggart et al., 2018] in cadaver models. Similar findings were found with regards to curvature and tortuosity, whose variations between straight and bent configurations reflect the outcomes of unstented zone A. Unfortunately, no other direct comparison with other published articles is available in case of popliteal aneurysms.

Though no statistical significance was reached, the largest change in vessel foreshortening was observed distal to the stent-graft, in zone C. In this segment the FPA foreshortened on average 7.9% which is in line with the results of MacTaggart et al. [MacTaggart et al., 2018] mea-

sured in perfused cadavers. Moreover, we detected an average reduction of diameter of 1.25% distally to the stent. A possible explanation is that in this area the sub-articular popliteal artery is less affected by the presence of muscle mass, so it is more physiologically subject to variations during flexion. It is also important to note that the average length of segment C was only 45±36 mm, which is 5-fold shorter than lengths of segments A and B. This smaller length and large variation may have contributed to the lack of statistical significance.

While our study describes morphologic changes to the endovascularly-repaired PAAs during limb flexion, its findings need to be considered in the context of study limitations. First and foremost, we were only able to recruit a small number of patients. Though PAAs are the most frequently encountered peripheral aneurysms, the overall prevalence is low (<1%). Furthermore, not all patients are treated endovascularly, and from those that are, some are unable to undergo post-operative CTA. All these factors significantly reduced our sample size, and larger studies are required to validate our conclusions.
The second limitation is related to the heterogeneity in patient conditions and repair configurations. As demonstrated in Figure 8.3, there was a significant difference in the location, length, and number of stent-grafts between all seven patients, producing an appreciable variation in the lengths of zones A, B, and C. This limitation is particularly important as the FPAs are known to deform non-uniformly along their lengths [MacTaggart et al., 2014]. Another limitation is related to comparisons of our results with literature data that is composed of a very inhomogeneous data including different disease pathologies, age, and vessel type.
To address this, future assessments should also include pre-operative bilateral bent-limb scans which can act as a proper baseline for post-operative comparisons. Such studies will also allow to assess the effects of surgical exposure of the proximal SFA on arterial deformations - an aspect that has not been evaluated here.
Finally, future work will include the analysis of arterial hemodynamics in the bent limb configuration as previously done for the non-stented artery [Desyatova et al., 2017a], and utilize arterial landmarks to assess arterial twist during flexion of the limbs [Desyatova et al., 2017b]. While these limitations are being addressed, our work provides the initial assessment of FPA biomechanics in patients with endovascularly-repaired popliteal aneurysms, and describes a CTA protocol to perform this assessment in 3D.

## 8.5 Conclusions

In this study, the complex behavior of PFA segment during knee bending in patients treated for PAA has been investigated. Our data demonstrates that the popliteal artery is a hostile environment for endovascular procedure due to changes in length, curvature and torsion during leg movements. The present analysis confirms that the stent-graft seems to be compliant with the physiological arterial changes during knee flexion and could be considered a valuable

treatment option to bypass surgery in selected cases.
Future research should focus on arterial hemodynamic behavior trying to identify the potential causes leading to stent failure.

# Chapter 9

# Conclusions and future perspectives

In the last years the advancement in imaging technologies and the introduction of new generations of endovascular devices have enable the endovascular procedure to be routinely performed in the clinical practice. However, it is not already well known how the introduction of a metallic graft could impact on a much more elastic native vessel. The present thesis aimed at expanding the knowledge in the field of vessel remodeling after endovascular procedure. In this study we integrated techniques of medical imaging and computational facilities to obtain a better understanding of the vascular pathologies and to provide outcomes with high impact in the clinical research.
In the following we have drawn conclusions for each chapter.
After having introduced the aim of the present doctoral research and the organization of the dissertation in **Chapter 1**, in **Chapter 2** an overview of the anatomy, the pathology and the treatments of the aorta is given. Moreover the Chapter illustrated the current medical imaging modalities and described the segmentation techniques and geometric feature extraction exploited in this work.
In **Chapter 3** a comprehensive literature review about remodeling of the aorta after endovascular treatment for dissections or aneurysmal pathologies is given. Two types of aortic remodeling are considered: positive remodeling is seen as the shrinkage of the aneurysmal sac or dissection false lumen thrombosis; on the other side endovascular procedure could influence the physiological shape of the aorta which could ultimately lead to device related complications.
In **Chapter 4** we have introduced a new pipeline for the geometric analysis of aneurysms, which has been applied to patients treated with the MFM device and related follow-up images. The dataset is composed of four patients affected by TAAA of different geometrical shape, which are also characterized by an extremely different behavior in terms of MFM implantation response. Therefore, our framework has been proved and is able to provide multiple and complete results for any aneurysm shape and for any morphological change in time. For the first time, a geometrical framework of analysis was introduced to be employed for the extraction of quantitative informations about follow-up morphological changes of the vessels.

Moreover, based on our findings, an accurate quantification of aneurysm progression over time after MFM implantation resulted of great importance.
An analysis with a larger and more homogeneous group could be assessed in order to give reliable results about the use and feasibility of the MFM stent in TAAA interventions.
In **Chapter 5** we assessed the influence of hybrid arch treatment on the remodeling of the aortic arch with a particular focus on endograft landing zones, attempting to enhance the understanding on the possible reasons for the development of device-related complications. Our results indicate that hybrid arch treatment modifies the morphology of the aortic arch tract, with both a significant elongation of the vessel and an increase in curvature. The significant increase in outerline curvature at endograft landing points reveals the tendency of the endograft to spring back to its original straight status. We therefore speculate that the force exerted by the endograft at proximal and distal ends causes an increasing of stress on the outer wall, ultimately leading to graft-related vessel injuries.
Future studies should focuses on the comparison between different aortic pathologies (e.g. aneurysms *vs* dissections).
In **Chapter 6** we described the case of a patient originally treated with TEVAR for TBAAD. Various full-size 3D models of the patient-specific vasculature were printed to better explain the different interventional interventions over the 12 years of follow-up and as a hands-on tool for medical education. The present case report, involving long-term follow-up, provides an example of the effectiveness and the safety of TEVAR for the treatment of complicated TBAAD shown at short and medium-term follow-up. However, the long-term complications that were observed in this patient during follow-up support the importance of lifelong CTA surveillance. Furthermore, the present study confirms the capability of 3D printing technology as powerful tool to support communication with patients and residents' education through the physical analysis of the real cases.
In **Chapter 7** we performed structural simulations to investigate in a patient-specific case the endografts deployment and evaluate wall apposition and conformation in a challenging tortuous descending thoracic aorta. This study demonstrated that patient-specific computational simulations could provide additional predictive information about the behavior of the devices, both during deployment and after expansion, driving the surgeons during the decision-making process.
In the future, additional simulations on a larger dataset should be performed.
Finally, **Chapter 8** was devoted to the study of endovascular treatment of the femoro-popliteal district to treat popliteal aneurysms. In particular, we have introduced a standardized protocol for CTA acquisitions with both flexed-leg and straight-leg positions in order to visualize the changes of arterial shape due to the knee flexion. Our results confirmed that the FPA segment is a hostile environment for endovascular procedure due to changes in length, curvature and torsion during leg movements. Endovascular treatment of popliteal aneurysms can be accomplished in selected cases using the GORE Viabahn stentgraft which seems to be compliant with the physiological arterial changes during knee flexion.
Future developments could involve structural and fluid dynamics simulations to provide a bet-

ter better understanding of the *in-vivo* changes of FPA kinematics due to leg flexion before and after stenting, and the correlations of such severe loading conditions on the mechanical behavior of the implanted devices.

## 9.1 Future directions

In this thesis work we tried to expand the knowledge on aortic and peripheral vessel remodeling after endovascular procedures. All the findings we presented form a foundation for further research developments in the field of cardiovascular research. In this final section, we discuss about new and improved technologies we are currently working on and about some possible future directions.

- **Systolic Left Ventricular Function.** Recent literature data imply that the increased vascular stiffness after endovascular stent graft deployment could cause increased arterial wave reflections, and this could lead to cardiac failure. This idea, if proven true, could become a predictor of cardiovascular events, even severe. Therefore, future studies that investigate the systolic left ventricular function before and after treatment in patients undergoing endovascular treatment for abdominal or thoracic aortic diseases are expecting to be of particular importance.

- **Structural finite element analysis.** In Chapter 7 we have shown the capability of finite element computational modeling to provide useful predictive information for pre-operative endovascular planning. Moreover, in Chapter 5 we hypothesized that the aortic remodeling we observed after TEVAR, and in particular the increase of curvature at endograft landing zones, are the results of the "spring" behavior of the endograft which tends to return to its original straight status. With a view to the future, finite element analysis could be employed in this scenario to simulate endograft deployment into the aortic arch and to investigate the distribution of forces and stress acting on the arterial wall.

- **Computational Fluid Dynamics.** In the recent years, the study of computational fluid dynamics is experimenting an increased interest in the field of vascular surgery. We will aim in the future to propose an integrate framework which combines image-based geometrical quantification of vascular anatomy with patient-specific computational techniques in order to improve the clinical diagnosis with a more personalized treatment planning.

# Bibliography

HB Alberta, JL Secor, TC Smits, MA Farber, WD Jordan, A Azizzadeh, JD Rovin, and JS Matsumura. Comparison of thoracic aortic diameter changes after endograft placement in patients with traumatic and aneurysmal disease. *Journal of vascular surgery*, 59(5): 1241–1246, 2014.

HB Alberta, T Takayama, TC Smits, BB Wendorff, RP Cambria, MA Farber, WD Jordan, V Patel, A Azizzadeh, JD Rovin, et al. Aortic arch morphology and aortic length in patients with dissection, traumatic, and aneurysmal disease. *European Journal of Vascular and Endovascular Surgery*, 50(6):754–760, 2015.

F Ansari, LK Pack, SS Brooks, and TM Morrison. Design considerations for studies of the biomechanical environment of the femoropopliteal arteries. *Journal of vascular surgery*, 58 (3):804–813, 2013.

L Antiga and DA Steinman. Robust and objective decomposition and mapping of bifurcating vessels. *IEEE Trans Med Imaging*, 2004.

L Antiga, B Ene-Iordache, and A Remuzzi. Centerline computation and geometric analysis of branching tubular surfaces with application to blood vessel modeling, 2003.

L Antiga, M Piccinelli, L Botti, B Ene-Iordache, A Remuzzi, and DA Steinman. An image-based modeling framework for patient-specific computational hemodynamics. *Medical & biological engineering & computing*, 46(11):1097, 2008.

MC Arokiaraj, G De Santis, M De Beule, and IF Palacios. Finite element modeling of a novel self-expanding endovascular stent method in treatment of aortic aneurysms . *Scientific Reports*, 2014.

F Auricchio and S Marconi. 3d printing: clinical applications in orthopaedics and traumatology. *EFORT open reviews*, 1(5):121–127, 2016.

F Auricchio, M Conti, S Marconi, A Reali, JL Tolenaar, and S Trimarchi. Patient-specific aortic endografting simulation: From diagnosis to prediction. *Computers in biology and medicine*, 43(4):386–394, 2013.

A Balderi, A Antonietti, F Pedrazzini, D Sortino, C Vinay, and M Grosso. Treatment of visceral aneurysm using multilayer stent: two-year follow-up results in five consecutive patients. *Cardiovasc Intervent Radiol.*, 2013.

J Baxa, T Vendiš, J Moláček, L Štěpánková, T Flohr, B Schmidt, JG Korporaal, and J Ferda. Low contrast volume run-off ct angiography with optimized scan time based on double-level test bolus technique–feasibility study. *European journal of radiology*, 83(3):e147–e155, 2014.

JD Beard, PA Gaines, and I Loftus. *Vascular and Endovascular Surgery E-Book: Companion to Specialist Surgical Practice*. Elsevier Health Sciences, 2013.

PJ Bels and ND McKay. A method for registration of 3-d shapes. *Proceedings of Spie- The international Society for Optical Engineering*, 1992.

A Benjelloun, M Henry, A Ghannam, C Vaislic, A Azzouzi, W Maazouzi, A Khlifi, and J Benamor. Endovascular treatment of a tuberculous thoracoabdominal aneurysm with the multilayer stent. *Journal of Endovascular Therapy*, 19(1):115–120, 2012.

M Berezowski, J Morlock, F Beyersdorf, M Jasinski, T Plonek, M Siepe, M Czerny, and B Rylski. Inaccurate aortic stent graft deployment in the distal landing zone: incidence, reasons and consequences. *European Journal of Cardio-Thoracic Surgery*, 53(6):1158–1164, 2017.

PJ Besl and ND McKay. A method for registration of 3-d shapes. *IEEE Transactions on Pattern Analysis and Machine Intelligence*, 14.2:239–256, 1992.

M Boufi, C Guivier-Curien, AD Loundou, V Deplano, O Boiron, K Chaumoitre, et al. Morphological analysis of healthy aortic arch. *Eur J Vasc Endovasc Surg*, 53:663–670, 2017.

A Bussmann, F Heim, C Delay, E Girsowicz, B Del Tatto, D Dion, J Papillon, A Lejay, J Chakfé, F Thaveau, et al. Textile aging characterization on new generations of explanted commercial endoprostheses: a preliminary study. *European Journal of Vascular and Endovascular Surgery*, 54(3):378–386, 2017.

Y Chen, S Zhang, L Liu, Q Lu, T Zhang, and Z Jing. Retrograde type a aortic dissection after thoracic endovascular aortic repair: A systematic review and meta-analysis. *Journal of the American Heart Association*, 6(9):e004649, 2017.

G Choi and CP Cheng. Quantification of in vivo kinematics of superficial femoral artery due to hip and knee flexion using magnetic resonance imaging. *Journal of Medical and Biological Engineering*, 36(1):80–86, 2016.

Ray W Clough. Original formulation of the finite element method. *Finite Elements in Analysis and Design*, 7(2):89–101, 1990.

MF Conrad, RS Crawford, CJ Kwolek, DC Brewster, TJ Brady, and RP Cambria. Aortic remodeling after endovascular repair of acute complicated type b aortic dissection. *Journal of vascular surgery*, 50(3):510–517, 2009.

M Conti, S Marconi, G Campanile, A Reali, D Adami, R Berchiolli, and F Auricchio. Patient-specific finite element analysis of popliteal stenting. *Meccanica*, 52(3):633–644, 2017.

M Conti, S Morganti, A Finotello, RM Romarowski, A Reali, and F Auricchio. Aortic endovascular surgery. In *Mathematical and Numerical Modeling of the Cardiovascular System and Applications*, pages 167–184. Springer, 2018.

V Costache, R Hulpus, A Costache, A Voican, and C Matei. The use of multilayer flow modulators in the endovascular treatment of complex aortic aneurysms and aortic dissections. *Journal of Indian College of Cardiology*, 6:44–51, 2016.

JL Cronenwett and KW Johnston. *Rutherford's Vascular Surgery E-Book*. Elsevier Health Sciences, 2014.

S De Bock, E Iannaccone, G De Santis, M De Beule, D Van Loo, D Devos, F Vermassen, P Segers, and B Verhegghe. Virtual evaluation of stent graft deployment: a validated modeling and simulation study. *Journal of the mechanical behavior of biomedical materials*, 13:129–139, 2012.

E Debing, D Aerden, S Gallala, F Vandenbroucke, and P Van den Brande. Stenting complex aorta aneurysms with the cardiatis multilayer flow modulator: first impressions. *Eur J Vasc Endovasc Surg.*, 2014.

A Desyatova, J MacTaggart, R Romarowski, Wi Poulson, M Conti, and A Kamenskiy. Effect of aging on mechanical stresses, deformations, and hemodynamics in human femoropopliteal artery due to limb flexion. *Biomechanics and modeling in mechanobiology*, 2017a.

A Desyatova, W Poulson, P Deegan, C Lomneth, A Seas, K Maleckis, J MacTaggart, and A Kamenskiy. Limb flexion-induced twist and associated intramural stresses in the human femoropopliteal artery. *Journal of The Royal Society Interface*, 14(128), 2017b.

A Desyatova, W Poulson, J MacTaggart, K Maleckis, and A Kamenskiy. Cross-sectional pinching in human femoropopliteal arteries due to limb flexion, and stent design optimization for maximum cross-sectional opening and minimum intramural stresses. *Journal of The Royal Society Interface*, 15(145), 2018.

N Diehm, S Sin, H Hoppe, and P Büchler. Computational biomechanics to simulate the femoropopliteal intersection during knee flexion: a preliminary study. *Journal of endovascular therapy*, 18(3):388–396, 2011.

Z Dong, W Fu, Y Wang, C Wang, Z Yan, D Guo, X Xu, and B Chen. Stent graft-induced new entry after endovascular repair for stanford type b aortic dissection. *Journal of vascular surgery*, 52(6):1450–1457, 2010.

W Euringer, M Südkamp, B Rylski, and P Blanke. Endovascular treatment of multiple hiv-related aneurysms using multilayer stents. *Cardiovascular and interventional radiology*, 35 (4):945–949, 2012.

M Famularo, K Meyermann, and JV Lombardi. Aneurysmal degeneration of type b aortic dissections after thoracic endovascular aortic repair: A systematic review. *Journal of vascular surgery*, 66(3):924–930, 2017.

F Fanelli and MD Dake. Standard of practice for the endovascular treatment of thoracic aortic aneurysms and type b dissections. *Cardiovasc Intervent Radiol*, 32.5:849–860, 2009.

R Fattori, TT Tsai, T Myrmel, A Evangelista, JV Cooper, S Trimarchi, J Li, L Lovato, S Kische, KA Eagle, et al. Complicated acute type b dissection: is surgery still the best option?: a report from the international registry of acute aortic dissection. *JACC: Cardiovascular Interventions*, 1(4):395–402, 2008.

E Ferrero, L Gibello, M Ferri, A Viazzo, and F Nessi. Aortic arch rupture after multiple multilayer stent treatment of a thoracoabdominal aneurysm. *Journal of Vascular Surgery*, 2014.

A Fetzer, S Zelzer, T Schroeder, HP Meinzer, and M Nolden. An interactive 3d segmentation for the medical imaging interaction toolkit (mitk). *Conference: MICCAI, At Harward Medical School, Boston, MA, United States, Volume: Proc MICCAI IMIC*, 2014.

LK Findeiss and ME Cody. Endovascular repair of thoracic aortic aneurysms. *Semin Intervent Radiol*, 28:107–117, 2011.

D Fleischmann, GD Rubin, AA Bankier, and K Hittmair. Improved uniformity of aortic enhancement with customized contrast medium injection protocols at ct angiography. *Radiology*, 214(2):363–371, 2000.

MD Ford, Y Hoi, M Piccinelli, L Antiga, and DA Steinman. An objective approach to digital removal of saccular aneurysms: technique and applications. *The British journal of radiology.*, 2014.

A Ganguly, J Simons, A Schneider, B Keck, NR Bennett, RJ Herfkens, SM Coogan, and R Fahrig. In-vivo imaging of femoral artery nitinol stents for deformation analysis. *Journal of Vascular and Interventional Radiology*, 22(2):244–249, 2011.

BC Gardner and SS Sabri. Endoleak. In *IR Playbook*, pages 219–227. Springer, 2018.

P Geisbüsch, S Hoffmann, D Kotelis, T Able, A Hyhlik-Dürr, and D Böckler. Reinterventions during midterm follow-up after endovascular treatment of thoracic aortic disease. *Journal of vascular surgery*, 53(6):1528–1533, 2011.

Y Georg, A Bussmann, D Mathieu, F Heim, and N Durand, Band Chakfe. Clinical applications of the study of the radial force of thoracic stentgrafts. *Annals of vascular surgery*, 38:e16, 2017.

E Georgakarakos, CV Ioannou, S Volanis, Y Papaharilaou, I Ekaterinaris, and AN Katsamouris. The influence of intraluminal thrombus on abdominal aortic aneurysm wall stress. *Int Angiol*, 28, 2009.

T Gerasimidis, G Sfyroeras, K Papazoglou, G Trellopoulos, A Ntinas, and D Karamanos. Endovascular treatment of popliteal artery aneurysms. *European journal of vascular and endovascular surgery*, 26(5):506–511, 2003.

E Girsowicz, Y Georg, F Lefebvre, A Lejay, F Thaveau, C Roy, M Ohana, and N Chakfe. Anatomical study of healthy aortic arches. *Annals of vascular surgery*, 44:179–189, 2017.

C Gökgöl, S Schumann, N Diehm, G Zheng, and P Büchler. In vivo quantification of the deformations of the femoropopliteal segment: Percutaneous transluminal angioplasty vs nitinol stent placement. *Journal of Endovascular Therapy*, 24(1):27–34, 2017.

M Grabenwoger, F Alfonso, J Bachet, R Bonser, M Czerny, H Eggebrecht, and CA Nienaber. Thoracic endovascular aortic repair (tevar) for the treatment of aortic diseases: a position statement from the european association for cardio-thoracic surgery (eacts) and the european society of cardiology (esc), in collaboration with the european association of percutaneous cardiovascular interventions (eapci). *European journal of cardio-thoracic surgery*, 42(1):17–24, 2012.

Y Guan, J Lin, Z Dong, and L Wang. Comparative study of the effect of structural parameters on the flexibility of endovascular stent grafts. *Advances in Materials Science and Engineering*, 2018, 2018.

HT Hassoun, RS Mitchell, MS Makaroun, AJ Whiting, KR Cardeira, and JS Matsumura. Aortic neck morphology after endovascular repair of descending thoracic aortic aneurysms. *Journal of vascular surgery*, 43(1):26–31, 2006.

GM Heisler and DR Dewalle. Effects of windbreak structure on wind flow. In *Windbreak technology*, pages 41–69. Elsevier, 1988.

M Henry, A Polydorou, N Frid, P Gruffaz, I Cavet, and I Henry. Treatment of renal artery aneurysm with the multilayer stent. *J. Endovasc. Ther*, 2008.

M Henry, A Benjelloun, and I Henry. Tct-591: a new concept of stent: the multilayer stent. first human study in taaa & aaa. *J Am Coll Cardiol*, 58:B159, 2011.

M Henry, A Benjelloun, I Henry, and G Wheatley. The multilayer flow modulator stent for the treatment of arterial aneurysms. *J. Cardiovasc. Surg.*, 2013.

D Ho, A Squelch, and Z Sun. Modelling of aortic aneurysm and aortic dissection through 3d printing. *Journal of medical radiation sciences*, 64(1):10–17, 2017.

CW Hull. Apparatus for production of three-dimensional objects by stereolithography, March 11 1986. US Patent 4,575,330.

N Hynes, S Sultan, A Elhelali, EB Diethrich, EP Kavanagh, M Sultan, F Stefanov, P Delassus, and L Morris. Systematic review and patient-level meta-analysis of the streamliner multilayer flow modulator in the management of complex thoracoabdominal aortic pathology. *Journal of Endovascular Therapy*, 23(3):501–512, 2016.

W Ibrahim, K Spanos, A Gussmann, CA Nienaber, J Tessarek, H Walter, J Thalwitzer, SE Debus, N Tsilimparis, and T Kölbel. Early and midterm outcome of multilayer flow modulator stent for complex aortic aneurysm treatment in germany. *Journal of vascular surgery*, 2018.

MW Itagaki. Using 3d printed models for planning and guidance during endovascular intervention: a technical advance. *Diagnostic and Interventional Radiology*, 21(4):338, 2015.

RA Jánosi, K Tsagakis, M Bettin, P Kahlert, M Horacek, F Al-Rashid, T Schlosser, H Jakob, H Eggebrecht, and R Erbel. Thoracic aortic aneurysm expansion due to late distal stent graft-induced new entry. *Catheterization and Cardiovascular Interventions*, 85(2):E43–E53, 2015.

CG Júnior, ESL Botelho, and LA dos Santos Diego. Intraoperative monitoring with transesophageal echocardiography in cardiac surgery. *Revista brasileira de anestesiologia*, 61(4): 503–512, 2011.

NPE Kadoglou, KG Moulakakis, I Papadakis, I Ikonomidis, M Alepaki, A Spathis, P Karakitsos, J Lekakis, and CD Liapis. Differential effects of stent-graft fabrics on arterial stiffness in patients undergoing endovascular aneurysm repair. *Journal of Endovascular Therapy*, 21 (6):850–858, 2014.

A Kaladji, R Spear, A Hertault, J Sobocinski, B Maurel, and S Haulon. Centerline is not as accurate as outer curvature length to estimate thoracic endograft length. *European Journal of Vascular and Endovascular Surgery*, 46(1):82–86, 2013.

WC Kang, RK Greenberg, TM Mastracci, MJ Eagleton, AV Hernandez, AC Pujara, and EE Roselli. Endovascular repair of complicated chronic distal aortic dissections: intermediate outcomes and complications. *The Journal of thoracic and cardiovascular surgery*, 142 (5):1074–1083, 2011.

C Kleinstreuer, Z Li, CA Basciano, S Seelecke, and MA Farber. Computational mechanics of nitinol stent grafts. *Journal of biomechanics*, 41(11):2370–2378, 2008.

Ralf Robert Kolvenbach. Contemporary strategies for repair of complex thoracoabdominal aortic aneurysms: real-world experiences and multilayer stents as an alternative. *Jornal vascular brasileiro*, 16(4):293–303, 2017.

MR Kret, AF Azarbal, EL Mitchell, Timothy K Liem, GJ Landry, and GL Moneta. Compliance with long-term surveillance recommendations following endovascular aneurysm repair or type b aortic dissection. *Journal of vascular surgery*, 58(1):25–32, 2013.

JC Lasheras. The biomechanics of arterial aneurysms. *Annu. Rev. Fluid Mech.*, 39:293–319, 2007.

Kedar S Lavingia, Sadaf S Ahanchi, Richard E Redlinger, Navalkishor R Udgiri, and Jean M Panneton. Aortic remodeling after thoracic endovascular aortic repair for intramural hematoma. *Journal of vascular surgery*, 60(4):929–936, 2014.

AM Lazaris, AN Maheras, and SN Vasdekis. A multilayer stent in the aorta may not seal the aneurysm, thereby leading to rupture. *Journal of Vascular Surgery*, 2012.

AE Leake, MA Segal, RA Chaer, MH Eslami, G Al-Khoury, MS Makaroun, and ED Avgerinos. Meta-analysis of open and endovascular repair of popliteal artery aneurysms. *Journal of vascular surgery*, 65(1):246–256, 2017.

D Levy and JK Le. Aortic, dissection. `https://www.ncbi.nlm.nih.gov/books/NBK441963`, 2018.

WE Lorensen and HE Cline. Marching cubes: A high resolution 3d surface construction algorithm. In *ACM siggraph computer graphics*, volume 21, pages 163–169. ACM, 1987.

X Lou, EP Chen, YM Duwayri, RK Veeraswamy, WD Jordan Jr, CA Zehner, and BG Leshnower. The impact of thoracic endovascular aortic repair on long-term survival in type b aortic dissection. *The Annals of thoracic surgery*, 105(1):31–38, 2018.

RE Lovegrove, M Javid, TR Magee, and RB Galland. Endovascular and open approaches to non-thrombosed popliteal aneurysm repair: a meta-analysis. *European Journal of Vascular and Endovascular Surgery*, 36(1):96–100, 2008.

C Lowe, A Worthington, F Serracino-Inglott, R Ashleigh, and C McCollum. Multi-layer flow-modulating stents for thoraco-abdominal and peri-renal aneurysms: the uk pilot study. *European Journal of Vascular and Endovascular Surgery*, 51(2):225–231, 2016.

J MacTaggart, W Poulson, A Seas, P Deegan, C Lomneth, A Desyatova, K Maleckis, and A Kamenskiy. Stent design affects femoropopliteal artery deformation. *Annals of surgery*, 2018.

JN MacTaggart, NY Phillips, CS Lomneth, II Pipinos, R Bowen, BT Baxter, J Johanning, GM Longo, AS Desyatova, MJ Moulton, et al. Three-dimensional bending, torsion and axial compression of the femoropopliteal artery during limb flexion. *Journal of biomechanics*, 47 (10):2249–2256, 2014.

S Marconi, L Pugliese, M Botti, A Peri, E Cavazzi, S Latteri, F Auricchio, and A Pietrabissa. Value of 3d printing for the comprehension of surgical anatomy. *Surgical endoscopy*, 31(10): 4102–4110, 2017.

A Marro, T Bandukwala, and W Mak. Three-dimensional printing and medical imaging: a review of the methods and applications. *Current problems in diagnostic radiology*, 45(1): 2–9, 2016.

G Matalanis, NK Perera, and SD Galvin. Total aortic repair: the new paradigm in the treatment of acute type a aortic dissection. *Annals of cardiothoracic surgery*, 5(3):216, 2016.

G Melissano, L Bertoglio, E Rinaldi, D Mascia, A Kahlberg, D Loschi, M De Luca, F Monaco, and R Chiesa. Satisfactory short-term outcomes of the stabilise technique for type b aortic dissection. *Journal of vascular surgery*, 2018.

Task Force members, R Erbel, V Aboyans, C Boileau, E Bossone, RD Bartolomeo, H Eggebrecht, A Evangelista, V Falk, H Frank, et al. 2014 esc guidelines on the diagnosis and treatment of aortic diseases: Document covering acute and chronic aortic diseases of the thoracic and abdominal aorta of the adult the task force for the diagnosis and treatment of aortic diseases of the european society of cardiology (esc). *European heart journal*, 35(41): 2873–2926, 2014.

Z Meng, T Ma, S Wang, Z Dong, and W Fu. Finite element analysis for type b aortic dissection treated with two types of stent grafts. *Molecular & Cellular Biomechanics*, 16(S1), 2019.

G Mestres, ME Garcia, X Yugueros, R Urrea, P Trunki, F Gomez, et al. Aortic arch and thoracic aorta curvature remodeling after thoracic endovascular aortic repair. *Ann Vasc Surg*, 38:233–241, 2017.

M Midulla, R Moreno, A Negre-Salvayre, F Nicoud, JP Pruvo, S Haulon, and H Rousseau. Impact of endografting on the thoracic aortic anatomy: comparative analysis of the aortic geometry before and after the endograft implantation. *Cardiovascular and interventional radiology*, 37(1):69–76, 2014.

RK Milewski, WY Szeto, A Pochettino, GW Moser, P Moeller, and JE Bavaria. Have hybrid procedures replaced open aortic arch reconstruction in high-risk patients? a comparative study of elective open arch debranching with endovascular stent graft placement and conventional elective open total and distal aortic arch reconstruction. *The Journal of thoracic and cardiovascular surgery*, 140(3):590–597, 2010.

RS Mitchell, S Ishimaru, MP Ehrlich, T Iwase, L Lauterjung, T Shimono, et al. First international summit on thoracic aortic endografting: roundtable on thoracic aortic dissection as an indication for endografting. *J Endovasc Ther*, pages 98–105, 2002.

KG Moulakakis, SN Mylonas, J Kakisis, NPE Kadoglou, I Papadakis, GS Sfyroeras, CCN Antonopoulos, G Mantas, I Ikonomidis, and CD Liapis. Arterial stiffness alterations and inflammatory response following endovascular aortic repair. *AORTA Journal*, 3(2):75, 2015.

SV Murphy and A Atala. 3d bioprinting of tissues and organs. *Nature biotechnology*, 32(8): 773, 2014.

FF Mussa, JD Horton, R Moridzadeh, J Nicholson, S Trimarchi, and KA Eagle. Acute aortic dissection and intramural hematoma: a systematic review. *Jama*, 316(7):754–763, 2016.

NNN Naguib, B Zima, A Nour-Eldin, T Gruber-Rouh, S Fischer, B Schulz, K Eichler, T Schmitz-Rixen, A Moritz, JO Balzer, et al. Long-term changes in aortic length after thoracic endovascular aortic repair. *Journal of Vascular and Interventional Radiology*, 27 (2):181–187, 2016.

DA Nation and GJ Wang. Tevar: Endovascular repair of the thoracic aorta. *Semin Intervent Radiol*, 32:265–271, 2015.

M Natrella, M Castagnola, F Navarretta, M Cristoferi, G Fanelli, T Meloni, and F Peinetti. Treatment of juxtarenal aortic aneurysm with the multilayer stent. *Journal of Endovascular Therapy*, 19(1):121–124, 2012.

FJH Nauta, GHW Van Bogerijen, C Trentin, M Conti, F Auricchio, FL Moll, JA Van Herwaarden, and S Trimarchi. Impact of thoracic endovascular aortic repair on pulsatile circumferential and longitudinal strain in patients with aneurysm. *Journal of Endovascular Therapy*, 24(2):281–289, 2017.

R Ní Ghriallais, K Heraty, B Smouse, M Burke, P Gilson, and M Bruzzi. Deformation of the femoropopliteal segment: effect of stent length, location, flexibility, and curvature. *Journal of Endovascular Therapy*, 23(6):907–918, 2016.

Y Nomura, K Sugimoto, Y Gotake, K Yamanaka, T Sakamoto, A Muradi, T Okada, M Yamaguchi, and Y Okita. Comparison of volumetric and diametric analysis in endovascular repair of descending thoracic aortic aneurysm. *European Journal of Vascular and Endovascular Surgery*, 50(1):53–59, 2015.

GS Oderich and D Factor. *Endovascular Aortic Repair: Current Techniques with Fenestrated, Branched and Parallel Stent-Grafts*. Springer, 2017.

PT O'gara. Aortic aneurysm. *Circulation*, 107(6):e43–e45, 2003.

Kenneth Ouriel. Popliteal and femoral aneurysms. *Vascular Surgery 5^*, pages 1103–1112, 1995.

B Pane, G Spinella, M Salcuni, and D Palombo. Stent-graft and multilayer stent for treatment of type ii thoracoabdominal aortic aneurysm in a high-risk patient. *The Journal of cardiovascular surgery*, 54(4):505–509, 2013.

KH Park, C Lim, JH Choi, E Chung, S Il Choi, EJ Chun, and K Sung. Midterm change of descending aortic false lumen after repair of acute type i dissection. *The Annals of thoracic surgery*, 87(1):103–108, 2009.

BO Patterson, RJ Cobb, A Karthikesalingam, PJ Holt, RJ Hinchliffe, IM Loftus, and MM Thompson. A systematic review of aortic remodeling after endovascular repair of type b aortic dissection: methods and outcomes. *The Annals of thoracic surgery*, 97(2): 588–595, 2014.

D Perrin, P Badel, L Orgeas, C Geindreau, S Rolland du Roscoat, JN Albertini, and S Avril. Patient-specific simulation of endovascular repair surgery with tortuous aneurysms requiring flexible stent-grafts. *Journal of the mechanical behavior of biomedical materials*, 63:86–99, 2016.

M Piccinelli, A Veneziani, DA Steinman, A Remuzzi, and L Antiga. A framework for geometric analysis of vascular structures: application to cerebral aneurysms. *IEEE transactions on medical imaging*, 28(8):1141–1155, 2009.

M Piccinelli, DA Steinman, Y Hoi, F Tong, A Veneziani, and L Antiga. Automatic neck plane detection and 3d geometric characterization of aneurysmal sacs. *Annals of Biomedical Engineering*, 2012.

A Polydorou, M Henry, I Bellenis, D Kiskinis, K Bolos, K Athanasiadou, A Portinos, P Dedeilias, I Kokotsakis, P Anthopoulos, et al. Endovascular treatment of arterial aneurysms with side-branches–a simple method. myth or reality? *Hospital Chronicles*, 5(2):88–94, 2010.

MP Poullis, R Warwick, A Oo, and RJ Poole. Ascending aortic curvature as an independent risk factor for type a dissection, and ascending aortic aneurysm formation: a mathematical model. *European Journal of Cardio-Thoracic Surgery*, 33(6):995–1001, 2008.

W Poulson, A Kamenskiy, A Seas, P Deegan, C Lomneth, and J MacTaggart. Limb flexion-induced axial compression and bending in human femoropopliteal artery segments. *Journal of vascular surgery*, 67(2):607–613, 2018.

C Pratesi and R Pulli. *Menagement of complications after EVAR and TEVAR*. Edizioni Minerva Medica, 2018.

R Pulli, W Dorigo, P Castelli, V Dorrucci, F Ferilli, G De Blasis, V Monaca, E Vecchiati, A Benincasa, and C Pratesi. A multicentric experience with open surgical repair and endovascular exclusion of popliteal artery aneurysms. *European Journal of Vascular and Endovascular Surgery*, 45(4):357–363, 2013.

RE Pyeritz and C Gasner. *The Marfan syndrome*. National Marfan Foundation, 1999.

A Redheuil, WC Yu, E Mousseaux, AA Harouni, N Kachenoura, CO Wu, D Bluemke, and JAC Lima. Age-related changes in aortic arch geometry: relationship with proximal aortic function and left ventricular mass and remodeling. *Journal of the American College of Cardiology*, 58(12):1262–1270, 2011.

MMPJ Reijnen and SMM van Sterkenburg. Treatment of a salmonella-induced rapidly expanding aortic pseudoaneurysm involving the visceral arteries using the cardiatis multilayer stent. *Journal of vascular surgery*, 60(4):1056–1058, 2014.

V Riambau, D Böckler, J Brunkwall, P Cao, R Chiesa, G Coppi, et al. Editor's choice–management of descending thoracic aorta diseases: clinical practice guidelines of the european society for vascular surgery (esvs). *European Journal of Vascular and Endovascular Surgery*, 53.4:4–52, 2017.

RM Romarowski, M Conti, S Morganti, V Grassi, MM Marrocco-Trischitta, S Trimarchi, and F Auricchio. Computational simulation of tevar in the ascending aorta for optimal endograft selection: A patient-specific case study. *Computers in biology and medicine*, 103:140–147, 2018.

A Sandoo, JJCSV van Zanten, GS Metsios, D Carroll, and GD Kitas. The endothelium and its role in regulating vascular tone. *The open cardiovascular medicine journal*, 4:302, 2010.

ML Schermerhorn and DW Jones. Management of descending thoracic aorta disease: Evolving treatment paradigms in the tevar era. *European Journal of Vascular and Endovascular Surgery*, 1(53):1–3, 2017.

AG Sherrah, SM Grieve, RW Jeremy, PG Bannon, MP Vallely, and R Puranik. Mri in chronic aortic dissection: A systematic review and future directions. *Frontiers in Cardiovascular Medicine*, 2:5, 2015.

A Sisto, AL Restante, B Ait Brik, and L Preziosi. Numerical simulation comparison between monolayer and multilayer flow modulator in a cerebral saccular aneurysm. *The 5th IEEE International Conference on E-Health and Bioengineering - EHB 2015*, 2015.

HB Smouse, A Nikanorov, and D LaFlash. Biomechanical forces in the femoropopliteal arterial segment. *Endovascular Today*, 4(6):60–66, 2005.

F Stefanov, S Sultan, L Morris, A Elhelali, EP Kavanagh, V Lundon, M Sultan, and N Hynes. Computational fluid analysis of symptomatic chronic type b aortic dissections managed with the streamliner multilayer flow modulator. *Journal of vascular surgery*, 65(4):951–963, 2017.

E Sueyoshi, H Nagayama, K Hashizume, K Eishi, I Sakamoto, and M Uetani. Computed tomography evaluation of aortic remodeling after endovascular treatment for complicated

ulcer-like projection in patients with type b aortic intramural hematoma. *Journal of vascular surgery*, 59(3):693–699, 2014.

M Sultan and N Hynes. Disruptive endovascular technology with multilayer flow modulator stents as a therapeutic option in the management of thoracoabdominal aortic aneurysms. early results from the global independent mfm registry. *It J Vasc Endovasc Surg*, 19:215–228, 2012.

S Sultan and N Hynes. One-year results of the multilayer flow modulator stent in the management of thoracoabdominal aortic aneurysms and type b dissections. *Journal of Endovascular Therapy*, 2013.

S Sultan, N Hynes, EP Kavanagh, and EB Diethrich. How does the multilayer flow modulator work? the science behind the technical innovation, 2014a.

S Sultan, M Sultan, and N Hynes. Early mid-term results of the first 103 cases of multilayer flow modulator stent done under indication for use in the management of thoracoabdominal aortic pathology from the independent global mfm registry. *J Cardiovasc Surg (Torino)*, 55 (1):21–32, 2014b.

S Sultan, E Kavanagh, F Stefanov, M Sultan, V Costache, A Elhelali, V London, E Diethrich, and N Hynes. Streamliner multilayer flow modulator stents as a therapeutic option in the management of complex thoraco-abdominal aortic pathology report from global smfm registry. *Journal of Indian College of Cardiology*, 6:77–84, 2016.

E Taguchi, K Nishigami, S Miyamoto, T Sakamoto, and K Nakao. Impact of shear stress and atherosclerosis on entrance-tear formation in patients with acute aortic syndromes. *Heart and vessels*, 29(1):78–82, 2014.

MDBS Tam, SD Laycock, JRI Brown, and M Jakeways. 3d printing of an aortic aneurysm to facilitate decision making and device selection for endovascular aneurysm repair in complex neck anatomy. *Journal of Endovascular Therapy*, 20(6):863–867, 2013.

G Taubin. Curve and surface smoothing without shrinkage. In *Computer Vision, 1995. Proceedings., Fifth International Conference on*, pages 852–857. IEEE, 1995.

MJ Thubrikar, F Robicsek, M Labrosse, V Chervenkoff, and BL Fowler. Effects of thrombus on abdominal aortic aneurysm wall dilatation and stress. *The Journal of cardiovascular surgery*, 44:67–77, 2003.

IFJ Tielliu, ELG Verhoeven, CJ Zeebregts, TR Prins, MM Span, and JAM Van Den Dungen. Endovascular treatment of popliteal artery aneurysms: results of a prospective cohort study. *Journal of vascular surgery*, 41(4):561–566, 2005.

IFJ Tielliu, CJ Zeebregts, G Vourliotakis, F Bekkema, JAM Van Den Dungen, TR Prins, and ELG Verhoeven. Stent fractures in the hemobahn/viabahn stent graft after endovascular popliteal aneurysm repair. *Journal of vascular surgery*, 51(6):1413–1418, 2010.

M Tillich, RE Bell, DS Paik, D Fleischmann, MC Sofilos, LJ Logan, and GD Rubin. Iliac arterial injuries after endovascular repair of abdominal aortic aneurysms: correlation with iliac curvature and diameter. *Radiology*, 219(1):129–136, 2001.

IC Tintoiu, JA Elefteriades, A Ursulescu, M Underwood, and I Droc. *New Approaches to Aortic Diseases from Valve to Abdominal Bifurcation*. Academic Press, 2017.

VS Tolva, PG Bianchi, LV Cireni, A Lombardo, GC Keller, G Parati, and RM Casana. Multiple multilayer stents for thoracoabdominal aortic aneurysm: a possible new tool for aortic endovascular surgery. *International Journal of General Medicine*, 2012.

R Uflacker. Thoracic aorta and arteries of the trunk. *Atlas of Vascular Anatomy: An Angiographic Approach*, page 133, 2006a.

R Uflacker. Abdominal aorta and branches. *Atlas of vascular anatomy: an angiographic approach*, page 481, 2006b.

CD Vaislic, J Noël Fabiani, S Chocron, J Robin, VS Costache, JP Villemot, J Marc Alsac, PN Leprince, T Unterseeh, E Portocarrero, et al. One-year outcomes following repair of thoracoabdominal aneurysms with the multilayer flow modulator: report from the strato trial. *Journal of Endovascular Therapy*, 21(1):85–95, 2014.

CD Vaislic, JN Fabiani, S Chocron, J Robin, VS Costache, JP Villemot, JM Alsac, PN Leprince, T Unterseeh, E Portocarrero, Y Glock, H Rousseau, and STRATO Investigators Group. Three-year outcomes with the multilayer flow modulator for repair of thoracoabdominal aneurysms: A follow-up report from the strato trial. *Journal of Endovascular Therapy*, 2016.

DA Vorp, PC Lee, DHJ Wang, MS Makaroun, EM Nemoto, S Ogawa, and MW Webster. Association of intraluminal thrombus in abdominal aortic aneurysm with local hypoxia and wall weakening. *Journal of Vascular Surgery*, 34(2):291–299, 2001.

DHJ Wang, MS Makaroun, MW Webster, and DA Vorp. Effect of intraluminal thrombus on wall stress in patient-specific models of abdominal aortic aneurysm. *Journal of Vascular Surgery*, 36(3):598–604, 2002.

TF Weber, D Böckler, M Müller-Eschner, M Bischoff, M Kronlage, H von Tengg-Kobligk, H-U Kauczor, and A Hyhlik-Dürr. Frequency of abdominal aortic expansion after thoracic endovascular repair of type b aortic dissection. *Vascular*, 24(6):567–579, 2016.

A Wrede, F Wiberg, and S Acosta. Increasing the elective endovascular to open repair ratio of popliteal artery aneurysm. *Vascular and endovascular surgery*, 52(2):115–123, 2018.

M Xenos, Ns Labropoulos, S Rambhia, Y Alemu, S Einav, A Tassiopoulos, N Sakalihasan, and D Bluestein. Progression of abdominal aortic aneurysm towards rupture: refining clinical risk assessment using a fully coupled fluid–structure interaction method. *Annals of biomedical engineering*, 43(1):139–153, 2015.

MH Zhang, X Du, W Guo, XP Liu, X Jia, and YY Ge. Early and midterm outcomes of thoracic endovascular aortic repair (tevar) for acute and chronic complicated type b aortic dissection. *Medicine*, 96(28), 2017.

P Zhang, X Liu, A Sun, Y Fan, and X Deng. Hemodynamic insight into overlapping bare-metal stents strategy in the treatment of aortic aneurysm. *Journal of Biomechanics*, 2015.

# List of Publications*

## Other published manuscripts

- **Finotello A,** Morganti S, and Auricchio F (2017). Finite element analysis of TAVI: Impact of native aortic root computational modeling strategies on simulation outcomes. Medical engineering & physics, 47, 2-12.

## Book Chapter

- Spinella G, Pane B, **Finotello A,** Conti M, Gazzola V, Mambrini S, Ferrero C, Auricchio F, Palombo D. "Precision and control of thoracic stent graft deployment" in Endovascular treatment of aortic aneurysms: durable solution, Medea

- Conti M, Morganti S, **Finotello A,** Romarowski RM, Reali A, Auricchio F. "Aortic Endovascular Surgery" in Mathematical and Numerical Modeling of the Cardiovascular System and Applications, Springer

## Conference Proceedings

- **A. Finotello,** S. Morganti, S. Marconi, R. Romarowski, P. Totaro, F. Auricchio. Double aortic arch: engineering support to decision making process. ESB-ITA (Rome, Italy, 28-29 September 2017)

- **A. Finotello,** G. Spinella, M. Conti, E. Faggiano, B. Pane, F. Auricchio, D. Palombo. Aortic remodeling after hybrid treatment: a quantitative geometrical analysis. European Society of Vascular Surgery 31st Annual Meeting (Lyon, 19-22 September 2017)

- **A. Finotello,** G. Spinella, E. Faggiano, B. Pane, M. Conti, F. Auricchio, D. Palombo. Geometrical analysis of aortic arch morphological changes after hybrid treatment. 7th International Congress Aortic and Peripheral Surgery “HOW TO DO IT” (Milan, Italy, 15-17 December 2016)

*not included in the present thesis work

- E. Faggiano, **A. Finotello,** M. Fedele, G. Alaimo, M. Conti, S. Morganti, F. Auricchio. A study of the Cardiatis Multilayer Flow Modulator: from in-vivo geometrical analysis to patient-specific simulations. XIII Biannual Congress of the Italian Society of Industrial and Applied Mathematics (Milano, Italy, 13-16 September, 2016)

- S. Morganti, **A. Finotello,** N. Brambilla, F. Bedogni, F. Auricchio. Finite element analysis of TAVI: impact of native valve modeling strategies on simulation outcomes. ESB-ITA Thematic Conference: Frontier Biomechanical Challenges in Cardiovascular Physiopathology (Palermo, Italy, 8-9 September, 2016)